Graphite lubrication mechanism under high mechanical load

Zur Erlangung des akademischen Grades einer

DOKTORIN DER INGENIEURWISSENSCHAFTEN (Dr.-Ing.)

von der KIT-Fakultät für Maschinenbau des
Karlsruher Instituts für Technologie (KIT)

angenommene

DISSERTATION

von

M. Sc. Carina Elisabeth Morstein

Abstract

Many extreme applications such as in a vacuum, acidic environments, high-temperature applications, or under high load are challenging and lead to failure of conventional liquid lubricants such as oils and greases. For these cases, solid lubricants like graphite are an excellent alternative. Despite its early discovery, the understanding of graphite's lubrication mechanism remains incomplete. Two models are frequently cited up till today: the so-called card-deck model postulated by Bragg and Savage's adsorption model. The former does not provide a clear explanation for the moisture dependence of graphite lubrication and has been experimentally refuted. Savage's adsorption model offers a more profound explanation and also incorporates the effect of water molecules. However, it has been tested mainly on atomically flat surfaces or for small normal forces.

The subject of this work is the investigation of lubrication mechanism of graphite as a solid lubricant and the fundamental research of influencing parameters. For this purpose, microtribometer sliding experiments were carried out in a sphere-on-flat setup to investigate graphite lubrication especially under high loads. Iron plates coated with graphite by airbrush spray coating were used as samples. The first parameter studies were dedicated to the influence of normal force and coating thickness. A strong correlation between these parameters and the tribological performance were revealed, with the lowest friction being measured at the highest normal force and thinnest coating thickness. The substrate-coating adhesion hereby limits the coating lifetime, hence a step-wise investigation of the substrate roughness was conducted. Large friction reduction and a long lifetime rely on a thin carbon film formation, which is observed for industrial surface roughness values. Subsequently, an important aspect of this thesis is the in-depth analysis of the humidity dependence on graphite lubrication. Using transmission electron microscopy, a shear-induced transformation of graphite to turbostratic carbon is reported; hence, a new, extended graphite lubrication mechanism is proposed which is valid for both high and low contact pressures.

As a final aspect, the graphite lubricant was tested under rolling friction. These experiments ensured a comparability between the desired application, an axial rolling bearing, and revealed new insights. The formation of a thin tribofilm on the counter-body was observed and confirmed by Raman spectroscopy, which seems to significantly influence the tribological performance of the graphite coating.

Zusammenfassung

Viele tribologische Extremanwendungen wie im Vakuum, in sauren Umgebungen, bei Hochtemperaturanwendungen oder unter hoher Last sind anspruchsvoll und führen oft zum Versagen herkömmlicher flüssiger Schmierstoffe wie Öle und Fette. Für diese Fälle stellen Festschmierstoffe wie Graphit eine exzellente Alternative dar. Trotz seiner frühen Entdeckung ist das Verständnis des Graphitschmiermechanismus weiterhin unvollständig. Zwei Modelle werden hierbei bis heute viel zitiert: das von Bragg postulierte, so genannte Deck-of-Card-Modell und das Adsorptionsmodell von Savage. Ersteres liefert keine eindeutige Erklärung zur Feuchtigkeitsabhängigkeit der Graphitschmierung und wurde experimentell widerlegt. Das Adsorptionsmodell von Savage bezieht die Wirkung der Wassermoleküle mit ein, wurde jedoch hauptsächlich auf atomar flachen Oberflächen oder für kleine Normalkräfte getestet.

Die vorliegende Arbeit beschäftigt sich mit der Untersuchung des Schmierungsmechanismus von Graphit als Festschmierstoff und die tiefgreifende Erforschung der möglichen Einflussgrößen. In dieser Arbeit wurden deshalb Mikrotribometer-Gleitexperimente im Kugel-Platte-Kontakt durchgeführt, um die Graphitschmierung vor allem unter hohen Flächenpressungen zu untersuchen. Als Proben dienen hierfür mittels eines Airbrush-Sprühverfahren graphitbeschichteten Eisenplatten. Erste Parameterstudien widmeten sich dem Einfluss von Normalkraft und Schichtdicke und zeigten eine starke Korrelation sowie niedrigste Reibung bei höchster Normalkraft und dünnster Schichtdicke. Die Substrat-Beschichtungs-Adhäsion hat hierbei einen limitierenden Einfluss auf die Schichtlebensdauer, weshalb die Substratrauigkeit graduell variiert und untersucht wurde. Eine gute Reibminderung sowie lange Lebensdauer konnten auf die Bildung einer dünnen Kohlenstoffschicht zurückgeführt werden, welche bei industrienahen Oberflächenrauheiten gebildet wurde. Ein weiterer wichtiger Aspekt dieser Arbeit war im Anschluss die eingehende Analyse der Feuchtigkeitsabhängigkeit auf die Graphitschmierung. Mittels Transmissionselektronenmikroskopie konnte die Umformung von Graphit in turbostratischen Kohlenstoff nachgewiesen werden und somit ein neuer, erweiterter Schmiermechanismus vorgeschlagen werden. Diese in-situ-Bildung des turbostratischen Kohlenstoffs an der Gleitfläche wurde sowohl bei hohen als auch bei niedrigen Lasten beobachtet.

Als letzter Aspekt wurde der Graphitschmierstoff unter Rollreibung getestet. Hierdurch konnte Korrelationen zur gewünschten Anwendung, einem Axialwälzlager, gezogen und wichtige Erkenntnisse gewonnen werden. Es wurde die Bildung eines dünnen Tribofilms auf dem Gegenkörper beobachtet und durch Raman-Spektroskopie bestätigt, welcher die tribologische Leistung der Graphitbeschichtung maßgeblich zu beeinflussen scheint.

Acknowledgments

I could not have done this without the support of my family, who supported me no matter what. We shared excitement and nervousness during paper publishing processes, conference visits, and scientific talks. Thanks for your unconditional love and support.

Last but not least I want to thank my fiancé Leon. It has not always been easy and at times stressful, but you have never failed to offer me comfort, support, helpful advice, and warmth. You helped make hard decisions easier and see things more rationally. I can't wait to spend the rest of my life with you.

Filderstadt, in March 2023

Carina Morstein

Publications

This dissertation is based in part on previously published work, which are marked by citation in the respective sections, see below:

- C.E. Morstein and M. Dienwiebel, "Graphite Lubrication Mechanisms under high mechanical load", *Wear* 477, 203794, 2020

- A. Joerger, C. E. Morstein, M. Dienwiebel, and A. Albers, "A numerical approach for the determination of graphite deformation behaviour by using microtribological pressure tests", *Wear* 476, 203652, 2021

- C. E. Morstein, A. Klemenz, M. Dienwiebel, and M. Moseler, "Humidity-dependent lubrication of highly loaded contacts by graphite and a structural transition to turbostratic carbon", *Nature Communications* 13, 5958, 2022

Additional Publications:

- N. T. Garabedian, P. J.Schreiber, N. Brandt, P. Zschumme, I. L. Blatter, A. Dollmann, C. Haug, D. Kümmel, Y. Li, F. Meyer, et al., "Generating FAIR research data in experimental tribology", *Scientific Data* 9, 315 (2022)

Supervised Theses:

- H. Candan, "Grafit und Graphen: Einfluss der Luftfeuchtigkeit auf Reibung und Verschleiß", Bachelor's thesis, Karlsruhe Institute of Technology (KIT), Institute of Applied Materials - Reliability and Microstructure (IAM-ZM), Karlsruhe, Germany, 2020

- S. Yazgan, "Untersuchung des Substratrauheiteinflusses in graphitgeschmierten Metallkontakten", Bachelor's thesis, Karlsruhe Institute of Technology (KIT), Institute of Applied Materials - Reliability and Microstructure (IAM-ZM), Karlsruhe, Germany, 2021

- A. Z. Neidhardt, "Mechanismem der Graphitschmierung unter Wälzreibung", Bachelor's thesis, Karlsruhe Institute of Technology (KIT), Institute of Applied Materials - Reliability and Microstructure (IAM-ZM), Karlsruhe, Germany, 2021

Contents

1 Introduction

1.1 Motivation and Background

Tribology is the science focused on the analysis of friction, wear, and lubrication of bodies in relative motion [1]. Although unbeknownst to many, this science is present in many aspects of everyday life. Some of these aspects require high and consistent friction, as for example between the brake pad and rim to stop a bike. For others, low friction and wear are desired, for example on bicycle chains to ensure a force translation with minimal friction loss. With climate change in mind, it becomes even more crucial to maximize the efficiency of mechanical systems. Tribology gives us the needed tools to realize these goals – by minimizing friction and wear losses and maximizing the longevity of technical components, thus increasing sustainability. In addition, there is an economic drive behind it as well, as friction losses through energy dissipation control the efficiency of tribological systems [2]. In industrial countries, these losses can account for yearly 2-7% of the nominal gross domestic product [3] and for 23% of the global energy consumption, which could potentially be reduced by 8.6% by avoiding these friction losses [4]. In Germany, friction causes costs in the range of 185 Million Euro [5] and the emission of 208 Mt of CO_2 per year [4]. All these economical losses and CO_2 emissions from tribological contacts can be drastically reduced by lubrication with a suitable lubricant to reduce friction, wear, and improve the components' lifetime. To achieve this goal, a detailed understanding of the tribological system is needed to tune the base material or the lubricant in the desired way. This dissertation will focus on the latter.

1.2 Scope of this Thesis

Due to its mechanical and chemical characteristics, graphite has immense potential as a lubricant for challenging applications in systems experiencing high mechanical pressures. The goal of this thesis is a detailed understanding of graphite as a solid lubricant and its lubrication mechanisms under high load. The dissertation is part of the focus project "SPP2074 - Fluidfree lubrication under high mechanical loads" by the German Research Foundation/Deutsche Forschungsgemeinschaft DFG (an overview of the different projects and the involved institutions can be found in the appendix, see Figure A.1). In collaboration with the Fraunhofer Institute of Materials Mechanics (Fraunhofer IWM, Freiburg) and the Institute for Product Development (IPEK) at

KIT, graphite is analyzed as a solid lubricant for rolling bearings where high Hertzian pressures prevail. This thesis concentrates on the possibility to maximize tribological performance by tuning different lubricant and experimental parameters. A graphite coating was manually applied with an airbrush spray gun and its nano- and microscopic wear mechanisms were examined. The coating thickness, normal force, substrate roughness, and humidity were varied to shed light on the role of these parameters and their influence on friction, wear, and coating lifetime. In the beginning, these studies focused on graphite lubrication under sliding motion and the gained conclusions were afterwards applied to a rolling contact. By microtribometry, confocal microscopy, scanning electron microscopy, focused ion beam preparations, and especially transmission electron microscopy, the samples were analyzed prior to and after the experiments to elaborate on observed changes in the coating lubrication behavior. In the first part, the analyses under sliding motion were conducted by microtribometer experiments in reversible sliding motion for a deep understanding of the mechanisms dominating friction, wear, and lubrication. In the second part of the thesis, additional studies were conducted with a rolling motion to yield better comparability to the industrial application – in this project a rolling bearing.

2 Literature and Theoretical Background

2.1 Solid lubricants

For most tribological applications in day-to-day life, conventional liquid lubricants such as oils and greases are applied. The liquids usually function as a shear-accommodating layer between two moving surfaces and thus to avoid solid-solid contact between them, which would cause wear. However, liquid lubricants are limited in their applications, especially under harsh conditions such as vacuum, high temperatures, high loads, or acidic environments [6, 7]. Solid alternatives can be used where liquid alternatives would fail and lead to contamination or creep into undesirable places, for example in the aerospace or the food industry. These promising, solid lubricants can be divided into four groups [6, 8, 9]:

- Materials with a lamellar structure: sulphides, selenides, molybdenum disulfide (MoS_2), graphite, etc.

- oxidic or fluoridic compounds: lead oxide, sodium fluoride, etc.

- soft metals: lead, silver, gold, etc.

- polymers: polytetrafluoroethylene (PTFE), amides, imide, etc.

The three most commonly used solid lubricants are molybdenum disulfide, PTFE, and graphite. They are either used in their pure form or as additives in oils and greases. MoS_2 and graphite both display a lamellar structure and a high humidity dependence regarding their lubrication behavior. The main lubrication mechanism of MoS_2 relies on the creation and subsequent reorientation of basal planes parallel to the shearing direction as well as the formation of a transfer film. Singer stressed the importance of this transfer film formation for MoS_2 and solid lubricants in general to reduce the interfacial shear strength [9]. However, while MoS_2 performs best in a vacuum and suffers from high wear in ambient conditions, an opposing behavior is observed for graphite - the best lubrication results are reported in ambient humidity conditions. In contrast to the former two solid lubricants, lubrication by PTFE does not rely on any surrounding volatile molecules and thus works well both in vacuum and in humid air. PTFE needs to be applied as a rather thick coating to function in the desired way. Individual molecular chains are drawn out of the bulk material upon shear under low contact stresses of several MPa, leading to the formation of a thin lubricating

film on itself or the counterbody. [6, 9] This thesis will concentrate on graphite as a solid lubricant, as the desired application in a rolling bearing requires the lubricant to perform well under high mechanical load and ambient humidity.

2.2 Graphite Structure

Graphite is built from individual carbon layers on top of each other, which consist of hexagonal C_6 rings built from sp^2 hybridized carbon atoms. Along the basal planes strong, covalent bonds prevail (4.3 eV) whereas the individual carbon layers are 6.7 Å apart and interact only via comparably weak van-der-Waals forces (0.07 eV) and π bonds. Graphite occurs naturally predominantly in two crystalline forms: the alpha (hexagonal) and beta (rhombohedral) form, which vary in their graphite layer stacking. For the alpha form, ABAB stacking prevails (see Figure 2.1) as opposed to ABCA in the less common beta form. Both forms can be transformed into each other by mechanical treatments (alpha to beta) or via heating (beta to alpha). [10]
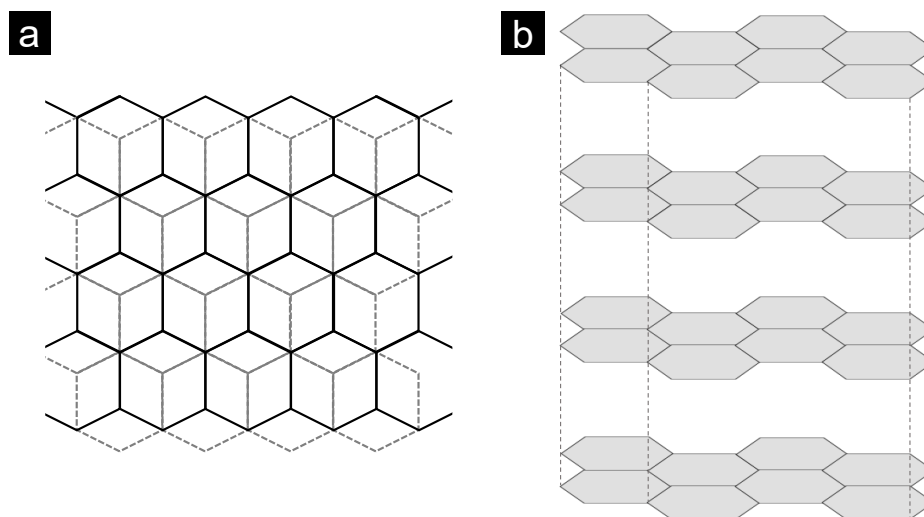
Figure 2.1: ABAB stacking of graphite, view from the top (a) and from the side (b), adapted from [10].

However, there is an additional graphite form, which is named turbostratic carbon (t-C). The turbostratic structure obtains a structural order ranging between amorphous and crystalline carbon. Amorphous carbon contains both sp^2- and sp^3-hybridized carbon and only short-range ordering. T-C has a graphite-like, layered structure where the basal planes are shifted and rotated out of alignment [11]. This shift leads to varying interlayer spacing with bent layers and smaller clusters [12]. This absence of stacking order leads to a weakening of the interplanar interaction, which is why t-C is usually considered a two-dimensional structure [13]. This graphite species can be produced for example by highly energetic material stressing in mechanical milling [14–

16]. However, t-C can also be found in soot or even in lunar soil samples, as shown by Mokhov et al. [17].

2.3 Lubrication Mechanisms and Humidity

Graphite is one of the oldest solid lubricants used [7]. Its lamellar structure was discovered by Bragg in 1928 via X-ray diffraction (XRD). Its lubrication behavior of graphite and other lamellar solid lubricants like molybdenum disulfide has since been often ascribed to the mutual sliding of the basal planes, as they are bound only by weak van-der-Waals forces. This structure leads to a low shear resistance [18] and the corresponding lubrication model is called the "deck-of-cards" [19] or "lattice-shear" model [20] (see Figure 2.2a, left panel). For many years up till this day, this model has been frequently cited by a number of papers and books [2, 6, 21]. For a better overview, the three most popular graphite lubrication models are summarized in Figure 2.2 and explained in the following paragraphs.

One problem with the deck-of-cards model arises as soon as the influence of humidity was discovered in the 1930s by Baker: in ambient conditions, friction and wear of graphite contacts are drastically low (μ = 0.08-0.18), whereas they suffer from high wear and "dusting" in dry, vacuum-like conditions (μ = 0.8) [22, 23]. This humidity dependence leads to a number of problems in everyday applications, for example in the aviation sector, where the power generators of multiple aircrafts failed. The aircrafts had risen to high altitudes, where a lack of humidity lead to high wear [24]. Savage revealed that graphite lubrication depends on the presence of water or other gases in the surrounding environment and is not, as one initially thought, an intrinsically good lubricant [23]. In conclusion, the original lattice-shear model fails to explain this behavior and demonstrated the need for alternative models.

G.W Rowe consequently hypothesized that water or gas molecules get intercalated in between basal planes, thus increasing the interlayer distance and reducing friction further (see Figure 2.2a, right panel). However, this hypothesis was tested experimentally by XRD experiments and no water was detected in the bulk [26] or between terminating graphite layers on the surface of graphite [20]. The lattice-shear model was in addition tested on microscale tribometry experiments with a wolfram stylus, where the failure of the model was reported for microscale tribological contacts [27].

The adsorption model by Savage offers an alternative mechanism for graphite lubricity, see Figure 2.2b [23]. He postulated the hypothesis that molecular water layers function as boundary lubrication films as they are adsorbed on the graphite surface. In addition, adsorbed water can saturate and passivate edges of reactive graphene layers on basal planes [29, 30] or graphite crystals perpendicular to the sliding direction [23, 27]. The adsorption model has been developed and tested in low-load technical applications, e.g. electrical contacts or journal bearings [23]. The graphite layer will most likely consist of multiple crystals with changing orientations. During sliding, the collision between two
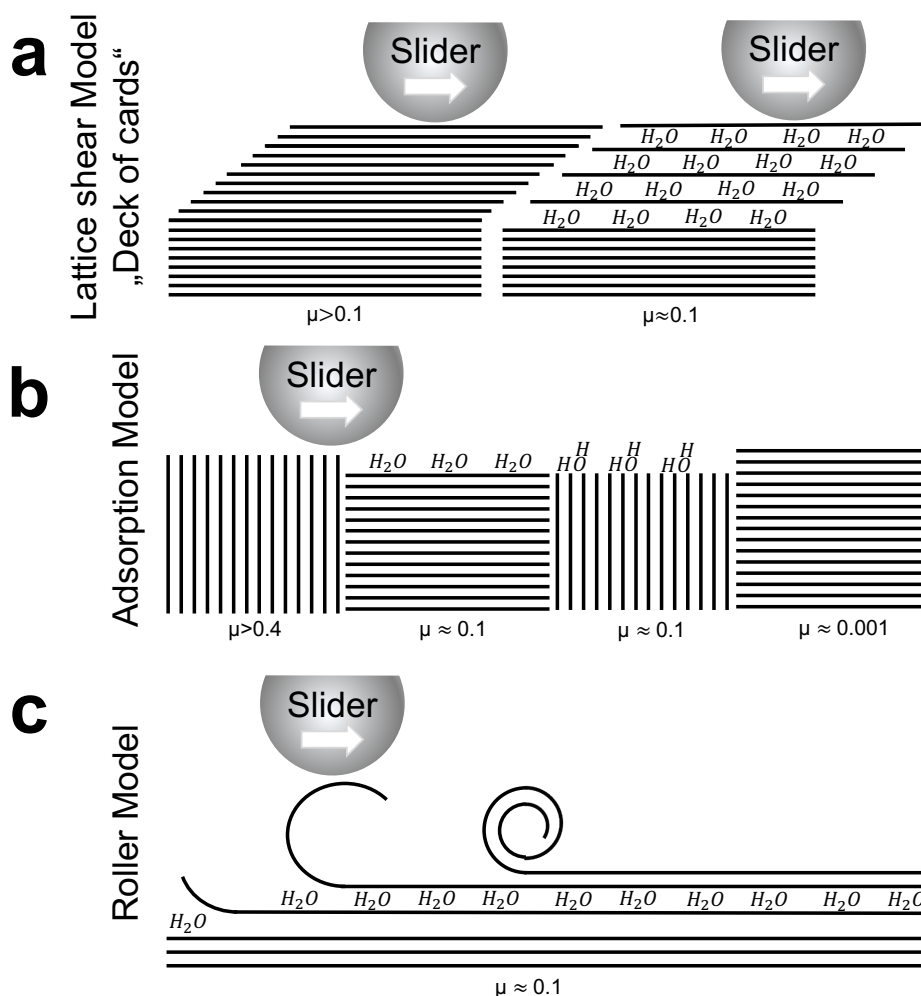
Figure 2.2: Schematic representation of the different models for solid lubrication by graphite. (a) Lattice-shear model: dry (left) and with water intercalation (right) (b) Adsorption model. (c) Roller model. Typical coefficients of friction μ values are given under the respective schematic drawing. Adapted from [28].

layers will lead to the continuous production of defects as well as changes in the crystal alignment. This is why, under dry conditions, increased friction is observed, which can be reduced in humid conditions due to the adsorption of water and hence passivation of defects. Different research groups have proven that carbon-based lubrication depends strongly on the number of defect sites and edges due to their negative influence on friction and wear [31, 32].

Non-commensurate dry contacts between two basal graphite crystals can lead to an increased friction reduction, as shown in Figure 2.2b, right panel [30, 33, 34]. Dienwiebel et al. have shown that the angle of two flat graphite surfaces plays an important role, as friction depends heavily on it. To enable this non-commensurate contact, both tribo-bodies in the sliding contact have to be covered by graphite. In most experimen-

tal set-ups, however, initially only one tribopartner is covered by the solid lubricant and thus, a transfer is required. Luckily, transfer of carbon films takes easily place in shearing experiments and has been observed by e.g. Merkle and Marks [35] for graphitic flakes and a tungsten sliding tip in their transmission electron microscopy (TEM) analyses. Another example was reported by Li, Ge, and Luo in a macroscopic sliding experiment between a steel sphere and HOPG [36].

Another mechanism explaining graphite's friction reduction is the so-called roller mechanism (see Figure 2.2c) proposed by Bollmann and Spreadborough. According to Bollmann and Spreadborough, individual packets of graphene layers can roll together when moved laterally, forming graphene rolls. They reduce friction in a bearing-like mechanism [37]. However, the humidity-dependence is here again explained by the intercalation of water (as in the work of G.W Rowe [25]), hence the model is in disagreement with the later-on conducted XRD experiments [26].

The majority of these models have been postulated under low loads and considerably low surface roughness. Hence, this thesis tackles the question of whether one of these models (especially the adsorption model) is valid under high pressure and how the surrounding water influences these applications. The water layers might get compressed and a push-out might occur under a pressure of 1 GPa and higher. This thesis aims to offer a more detailed understanding of the graphite lubrication mechanism, especially under high loads. Adding a piece of the puzzle to the knowledge about graphite lubrication might help the design of long-lived tribological parts applicable in extreme environments.

2.4 Graphite and Graphene in Tribology

Graphite is an extensively studied solid lubricant in a number of fundamental studies. However, most of these experiments and simulations have been conducted on the nanoscale [33, 38–41] and their gained results are hence only partially transferable to industrial applications. Nevertheless, these studies have proven that graphite is a suitable solid lubricant with extensive friction reduction for tribological contacts. In friction force microscopy experiments coefficients of friction (CoF) as low as 0.001 were yielded [42, 43].

A major drawback of graphite and graphene solid lubrication, however, is a high rupture-tendency of the layers at high loads, resulting in a lifetime limit and higher friction [41, 44–47]. This effect can be influenced by the thickness of the coating: for most research studies, the two-dimensional counterpart graphene yielded higher friction than multi-layer graphite. This effect was attributed to the increased flexibility and hence increase contact area [48, 49]. Other studies like the ones from Filleter et al. found higher friction for single-layer graphene in comparison to double-layer. This observation was explained by a better adhesion of the single-layer coating to the substrate [50]. Most of these conclusions were drawn after studies on thin, multilayer

graphene [51–53] and research on bulk graphite is lacking. However, this gap recently caught the attention from Shi et al. [53]. For soft, graphite-like carbon the group tested thicknesses from 0.55 to 1.55 µm against a Si_3N_4 sphere and yielded the best results for an intermediate thickness of 1.1 µm. Nonetheless, their CoF varied from 0.1 to 0.3 and is hence considerably higher than in comparable studies while exhibiting a long running-in period [53].

Graphene as a solid lubricant was extensively studied by Berman, Erdemir, and Sumant, often dispersed in ethanol solution for sliding contacts. They yielded 3-5 times reduced friction in comparison to an unlubricated metal-metal contact, as well as orders of magnitude lower wear [32, 54–56]. In general, graphite and graphene protect the underlying steel or iron surface from extensive oxidation by passivation. The passivated iron surface displays a nearly inert behavior and thus exhibits low shear strength and low adhesion, as demonstrated by Marchetto et al. [57]. Extreme conditions for graphite lubrication were demonstrated by S. Shaji for high temperature grinding [58] or wheel/rail systems by Fasihi et al. [59]. Conventionally, graphite is often used as a lubricant for high-temperature forming as well [60].

Another important factor influencing the tribological performance of graphite and graphene is substrate roughness. Many research groups focus on low substrate roughness in the nanometer range. Reinert et al. emphasized the importance of tuning the substrate roughness for the desired tribological application. For multi-wall carbon nanotubes and onion-like carbon, the best results were achieved on the smoothest substrate [61]. This outcome stresses the need for lubricants that can be applied to industrial applications with considerably higher roughness as the production of perfectly flat, defect-free substrates or lubricants is expensive and time-consuming.

Graphite is seldomly applied as a lubricant in larger machine elements like slide or rolling bearings. This might be due to the fact that solid lubrication is rarely thoroughly discussed in machine elements literature for engineers [62]. Nevertheless, some applications can be found. Sharma et al. investigated an alloy enforced with graphite particles, which decreased friction if boundary lubrication took place [63]. SKF advertises a graphite lubricated rolling bearing on their website [64] suitable for applications up to 350 °C, although the production line has been discontinued. Other companies focus either on whole rolling bodies made of a polymer-graphite mix [65] or incorporate graphite pockets in their machining parts [66]. However, in general there seems to be a lack of publications dealing with pure graphite lubrication for industrial machine elements.

2.5 Theoretical Discussions

2.5.1 Bowden-Tabor

For conventional, liquid lubricants the friction depends on velocity, pressure, and the viscosity of the lubricant. These matters influence where the tribosystem acts on the so-called Stribeck-curve. The curve allows one to deduce in which friction regime the experiment or application takes place: boundary lubrication, mixed lubrication elasto-hydrodynamic lubrication, or hydrodynamic lubrication. For most liquid lubrication applications it is desirable to remain in the hydrodynamic regime where no contact between the tribo-bodies will occur. In this friction regime, friction will increase with increasing load.

For solid lubricants, the load-friction correlation is slightly different and exhibits a non-Amontonian behavior. Scharf and Prasad published an extensive review on the importance and differences of solid lubrication [6]. As evident from their summary, friction in solid-lubricated contacts usually decreases if a higher load is applied. This behavior can be explained by the theory of Bowden and Tabor and is described by the following equation [67]:

$$\mu = \frac{F}{L} = \frac{\tau \cdot A_{\mathrm{r}}}{L} = \frac{\tau}{P_{\mathrm{H}}} = \frac{\tau_0}{P_{\mathrm{H}}} + \alpha \tag{2.1}$$

Here F is the friction force, L the applied normal force, τ_0 the interfacial shear strength, P_{H} the mean Hertzian pressure, and α the pressure dependence of the shear strength $(\tau = \tau_0 + \alpha(L))$. For solid lubricants, the coefficient of friction (CoF) decreases as the load increases since the real surface area A_{r} increases only marginally. To investigate what friction-normal force correlation occurs for the graphite coating prepared in this thesis, a matching parameter study was conducted and will be discussed in Section 4.5.1.

3 Materials and Methods

3.1 Sample Preparation: Polishing

For the majority of the tribological analyses, iron plates (Goodfellow GmbH, Germany, purity 99.5 %, 0.9 mm thickness, as milled) were used as the substrate, laser cut to the size of 16×6 mm. The substrate material was matched to the molecular dynamics (MD) simulations material, which were conducted by Dr. Andreas Klemenz at the Fraunhofer Institute for Mechanics of Materials IWM as a part of the SPP2074. 100Cr6 steel counterbodies were utilized for all experiments. This tribological pairing was chosen to ensure comparability to the desired real-life application, a rolling bearing.

To polish the iron plates to the desired surface finish, eight plates were glued onto a polishing holder with thermoplastic glue (Crystalbond 509-1, T-E-Klebetechnik, Germany) and polished on a semi-automatic grinding machine (Buehler PowerPro 4000, Buehler ITW Test and Measurement GmbH, Germany). Silicon carbide (SiC) papers (WS flex 18 C SK, Hermes Schleifmittel GmbH, Germany) of varying roughness were applied while the rotational speed was kept constant at 150 rpm. In between polishing steps, the plates were rinsed with water to remove any abrasive particles. To avoid corrosion, each sample was cleaned after polishing ultrasonically for 10 min in succession with acetone and isopropanol and afterwards dried with pressurized air. The precise polishing steps are later explained in Section 3.3.1: Substrate Roughness.

3.2 Sample Preparation: Coating

Initially, multiple coating techniques like spin-coating, extrusion printing, dip-coating, and airbrush spray coating were tested to obtain a homogeneous graphite coating. However, only airbrush spray coating resulted a reproducible and tunable coating process. Thus, most of the samples for the experiments presented in this thesis were obtained by applying a graphite suspension (L-GP 386 ACHESON, Henkel, the Netherlands) onto the plates with an airbrush spray gun (Harder & Steenbeck Ultra Solo Double Action, Harder & Steenbeck GmbH & Co.KG, Germany), see Figure 3.1a. At a working distance of approximately 15 cm, graphite coatings were manually deposited onto polished iron plates by moving the airbrush in consecutive sweeps across the substrate surface.

The graphite layer thickness was evaluated for all samples by confocal microscopy (Sensofar Plμ 2300, Sensofar Tech S.L., Spain). For this purpose, one end of the iron plate was covered with adhesive tape during the deposition process and the tape removed afterwards to determine the step height between substrate and coating. Two confocal images were taken at different light intensity (LS = 40 and 150) to capture both the highly reflective iron and the dark graphite coating and afterwards merged into one image in the Sensofar software "Mountainsview V6". An exception was made regarding the thickness of the thinnest coatings (0.2 μm), which was determined not by confocal microscopy but by optical measurements on FIB cross sections, as the graphite flakes did not lay flat on the substrate.
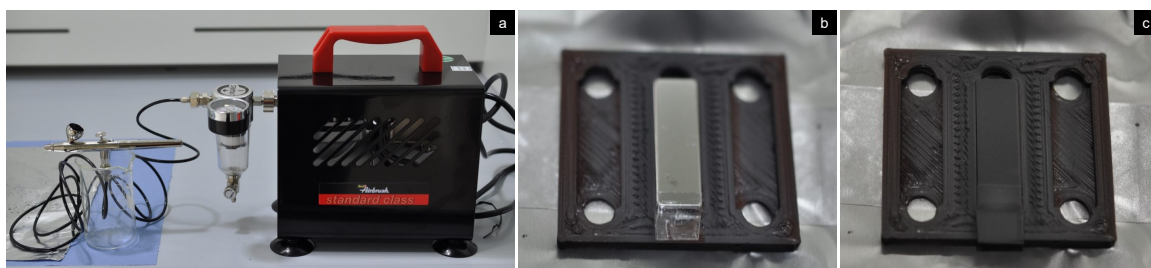
Figure 3.1: Setup for the graphite coating deposition with an airbrush spray gun. (a) airbrush pistol with compressor, (b) polished iron plate prior to coating, and (c) polished iron plate after the coating process. The plates are fixed with a small piece of scotch tape for the evaluation of the coating thickness afterwards by confocal microscopy.

3.3 Tribological experiments

In the scope of this thesis, the tribological performance of these graphite solid lubricants was tested; for this goal, different tribometers were utilized. For a detailed investigation under sliding motion, the microtribometer (Tetra Basalt Must, Tetra Ilmenau, Germany) and an ultra-high vacuum (UHV) tribometer were used in a linear-reversible sliding motion. The humidity of the microtribometer atmosphere was always controlled by purging either with pure dry or with humidified pressurized air. The UHV experiments were conducted in a vacuum with a small vial containing deionized water connected to the chamber – this vial allowed the controlled opening and thus dosage of humidity in the experimental chamber.

As a step towards understanding the real-life application of a rolling bearing, the same system was later investigated under rolling motion as well. For these investigations, a mini-traction-machine (MTM, PCS Instruments Ltd, England) was lent from the Fraunhofer IWM. The machine allows for tuning of the slide-to-roll-ration (SRR) and all experiments were conducted under a controlled atmosphere of dry pressurized air. For more parameters see Section 3.3.3.

If not denoted differently, all experiments were conducted at least three times to ensure reproducibility. The data points presented in this work represent the numerical average of these measurements, while the error bars display the standard error of the mean. By doing so, statistically secured statements or hypotheses were deducted. All experiments were conducted with different batches of iron plates and steel spheres and conducted on different days.

3.3.1 Microtribometer
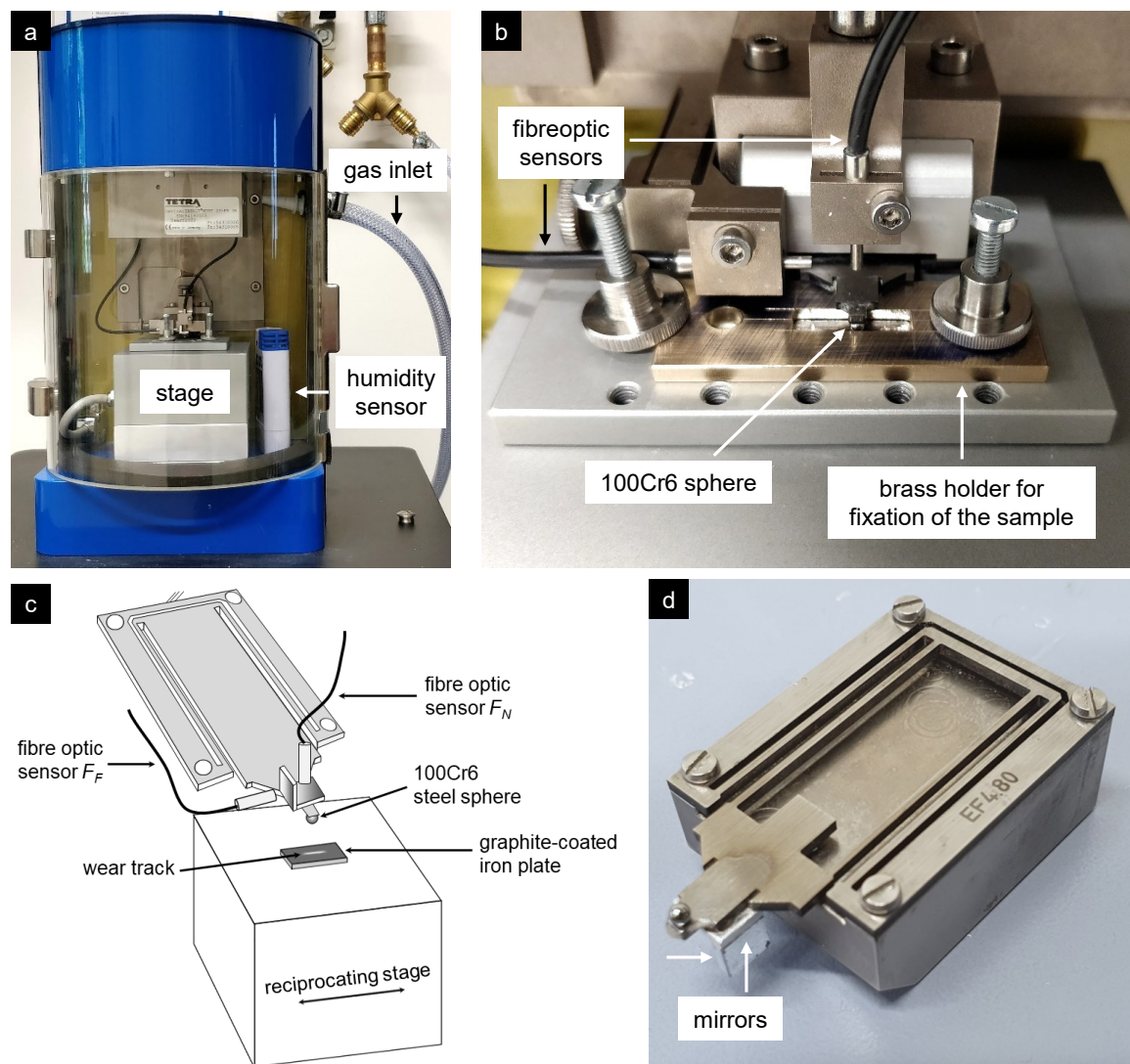
Figure 3.2: Microtribometer setup. (a) microtribometer, (b) spring cantilever with sample, (c) schematics of the microtribometer setup, (d) mounted cantilever.

The graphite-covered iron plates were tested in a microtribometer in linear reciprocating mode, as described in detail in [68]. Experiments were conducted at approx. 30 °C

under a constant pressurized air atmosphere and with a fresh counterbody for each experiment. In a sphere-on-flat setup, a 100Cr6 steel sphere (G10, Spherotech GmbH, Germany) with a diameter of 2 mm was used as a counterbody. The sphere was glued with cyanoacrylate glue (UHU Super Glue, UHU GmbH & Co. KG, Germany) onto a double-leaf cantilever with spring constants of $k_t = 4.802$ and $k_N = 1.914\,\mathrm{mN\,\mu m^{-1}}$. The normal and friction forces was continuously calculated and monitored by the software. For these calculations, fiber-optic sensors measured the distance to mirrors glued onto the cantilever. By regularly conducted weight calibrations with weights ranging from 5 - 50 g, the spring constants k could be determined. With the dislocation x of the mirrors and thus a change in distance between the fiber-optic sensor and mirror, the frictional force F_F (in x- or y-direction) and normal force F_N (z-direction) can be calculated according to Hooke's law, respectively (Equation 3.1):

$$k = \frac{F}{x} \tag{3.1}$$

In return, the friction coefficient μ is calculated by dividing the frictional force through the normal force, see Equation 3.2:

$$\mu = \frac{F_F}{F_N} \tag{3.2}$$

For the reciprocating linear sliding experiments in the microtribometer, a number of 500 linear reversing cycles were conducted at a stroke length of 1 mm and speeds of $0.1\,\mathrm{mm\,s^{-1}}$ or $0.5\,\mathrm{mm\,s^{-1}}$. The normal and the friction force was measured continuously during the experiment. Prior to the experiment, all residual glue on the steel sphere was removed with acetone and isopropanol to avoid any contamination or unwanted influence.

In the scope of this thesis, different parameters were varied to conduct parameter studies and to investigate their influence on friction, wear, and the mechanism of graphite lubrication. While varying one parameter, all the other ones were kept constant to enable a systematic investigation of the different parameters and their influence on friction and wear. The parameters were:

- graphite layer thickness (0.2 to 17 µm)

- normal force (69, 165, and 402 mN)

- different experimental run times (10, 100, 200, and 500 cycles)

- substrate roughness ($S_a = (11 \pm 2)$ to $(153 \pm 19)\,\mathrm{nm}$)

- relative humidity (≤ 5 to $45\,\%\,\mathrm{RH}$)

- slide-to-roll-ratio (0 to 15 %), investigated on the mini-traction-machine.

Graphite Layer Thickness

In a first parameter study conducted in the scope of this thesis, the influence of the graphite layer thickness was investigated. To do so, the volume flow rate was adjusted manually and the number of passes over the sample was varied to obtain five different coating thicknesses: 0.2, 3.5, 6, 10, and 17 μm. To create the thinnest tested layer, a different suspension (conductive graphene dispersion, Graphene Laboratories Inc., USA) was diluted with ethanol in a 3:1 ratio, ultra-sonicated for 24 h and applied in two consecutive sweeps. As a reference some polished iron plates remained uncoated to have the direct comparison to an unlubricated steel-iron contact. After this study, the coating thickness of 3.5 μm was found to be ideal and thus selected for all following experiments.

Normal Force

The above listed five different coating thicknesses and uncoated reference were thereafter investigated at three different normal forces each: 69, 165, 402 mN. The forces were chosen to cover a large range of resulting Hertzian contact pressures – 500, 750, and 1008 MPa, respectively. As the main focus of this thesis lies in the tribological performance of graphite at high loads, most of the following experiments were investigated with a normal force of 402 mN.

Substrate Roughness

In a first test, two different surface finishes were tested to investigate the substrate roughness influence on friction and wear. These included a mirror-like substrate, with an arithmetic average roughness of S_a of (11 ± 2) nm and a rougher, industrial-like finish with S_a of (70 ± 4) nm. Later, B.Sc. Serhan Yazgan conducted a deep parameter later study where six roughness states were analyzed. To achieve these different roughness states, different SiC papers were used, ranging from grain sizes of P320 to P4000. For the mirror-like finish, two polishing steps with polishing cloths (Microcloth SPT069-PT Seda S, Cloeren Technology GmbH, Germany) and monocrystalline diamond paste (DPA-M006 and DPA-M007, 3 and 1 μm, Cloeren Technology GmbH, Germany) were added. For the SiC steps the polishing contact was lubricated and cooled down with tap water; for the diamond paste steps, an ethanol-based lubricant (Lubricant Blue, Cloeren Technology GmbH, Germany) was used instead. These lubricants swept away continuously formed abrasive particles as well. Depending on the polishing steps different polishing times, normal forces, and rotational speeds were used. A complete list can be seen in Table 3.1:

Table 3.1: Repetition of polishing steps used for achieving the different roughness samples. Additional parameters: For all SiC Papers from P320 to P2500: duration = 3 min, force = 35 N, and speed = 200 rpm. For P4000 SiC paper and diamond paste: duration = 3 min, force = 50 N, and speed = 150 rpm.

Sample name	P320	P600	P1200	P2500	P4000	3 µm	1 µm
P320	2-6						
P600	3	4					
P1200			2				
P2500			2	1			
P4000			2	1	2		
mirror-like			2	1	2	1	1

Relative Humidity

The next parameter study revolved around the influence of humidity on friction and wear of graphite lubrication. The measurements were conducted by B.Sc. Harun Candan. To control the humidity inside the experimental chamber, a self-build humidifier system was incorporated, as depicted in Figure 3.3.
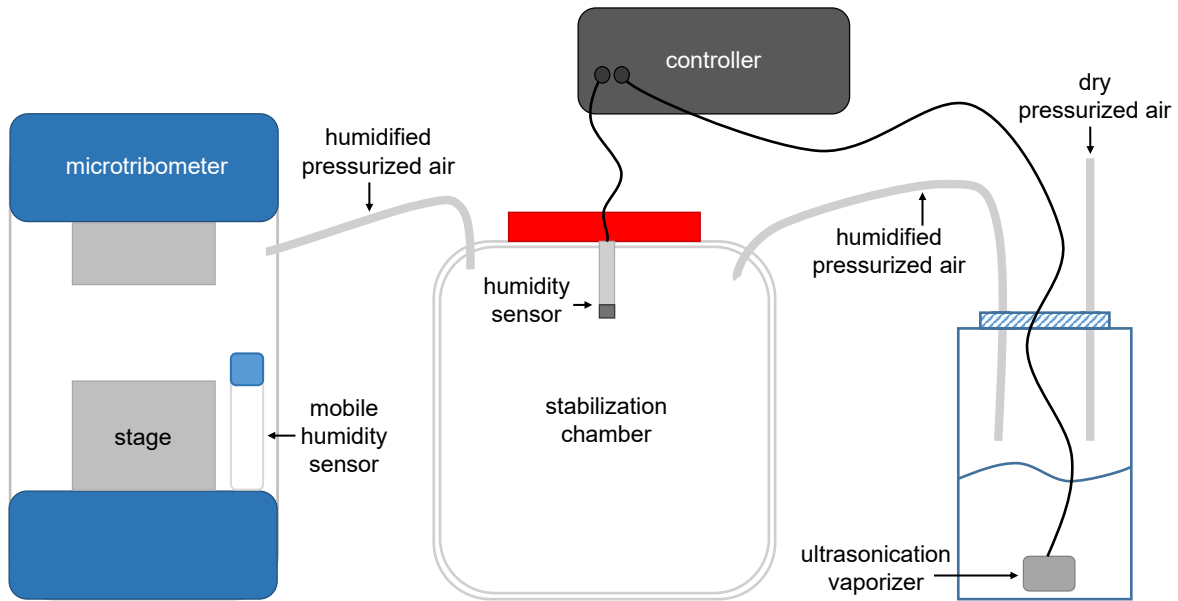
Figure 3.3: Schematics of the self-built humidifier setup for a controlled humidity environment in the microtribometer chamber.

First, a glass bottle was filled with 1 L of deionized water (containing 50 mL tap water) and an ultrasonication vaporizer was immersed in it. The desired relative humidity was monitored by the controller, which switched the vaporizer on and off accordingly. Through an inlet, dry pressurized air was purged into the closed glass bottle. Due to

Table 3.2: Tested relative humidity values and the respective stabilization time needed prior to the start of the experiment to ensure a stable humidity during it.

Relative Humidity [% RH]	Stabilization Time [min]
≤ 5	15
11	30
24	45
30	30
39	90
46	45

the water vapor, the air is humidified and flows through an outlet into a large barrel to stabilize the humidity and minimize large fluctuations. This barrel contained the humidity sensor connected to the controller to register the present relative humidity. Another tube led the humidified pressurized air into the microtribometer chamber, where the present relative humidity was monitored throughout the whole experimental duration with a mobile hygroscope (LOG210 PDF-data logger, Dostmann electronic, Germany). At low humidity (0-20 % RH) the hygroscope has a uncertainty of $\pm 5\%$ [69]. To ensure a stable and constant humidity inside the chamber, a stabilization time prior to the experiment start was determined, see Table 3.2. With this setup, the relative humidity was tuned between ≤ 5 and 45 % RH. Higher humidity values were not possible due to condensation at cold traps, thus heating of the whole setup would have been needed.

3.3.2 UHV-Tribometer

Another tribometer used in this thesis is the UHV tribometer built by Marchetto et al. [44]. For these analyses, the rougher (P1200) samples with a graphite coating of thickness of 3.5 µm were investigated. The sample was mounted on a sample holder positioned on a piezo actuator allowing for movements in x, y, and z direction with a motion range of 100 µm. Hence, a track length of 100 µm was chosen. Similarly as for the microtribometer experiments, a 100Cr6 sphere with a diameter of 2 mm was glued onto a double-leaf cantilever. A force of 402 mN was applied to yield a high contact pressure of 1 GPa. In the UHV tribometer, instead of fiber-optic sensors, a laser interferometer was used to measure the motion of the mirrors on the spring and thus the lateral and normal force. An extreme motion of the mirror would lead to the laser loosing focus, thus a harder spring with spring constants of $k_t = 25$ and $k_N = 39$ mN µm^{-1} was used. The humidity inside of the chamber could be varied by opening an attached valve containing deionized water prior to and throughout the experiment. By doing so, the humidity was altered between $6.5 \cdot 10^{-8}$ and $3.2 \cdot 10^{-4}$ Pa partial pressure of water. A mass spectrometer (MS) was attached to the UHV tribometer

chamber to determine both the water content and detect any volatile molecules that might be formed during the experiment. The mass spectrometer was equipped with a quadrupole analyzer and a Faraday detector (PrismaPlus QMG 220, Pfeiffer Vakuum GmbH, Germany) with a measuring range of 1-200 u.

3.3.3 Mini Traction Machine
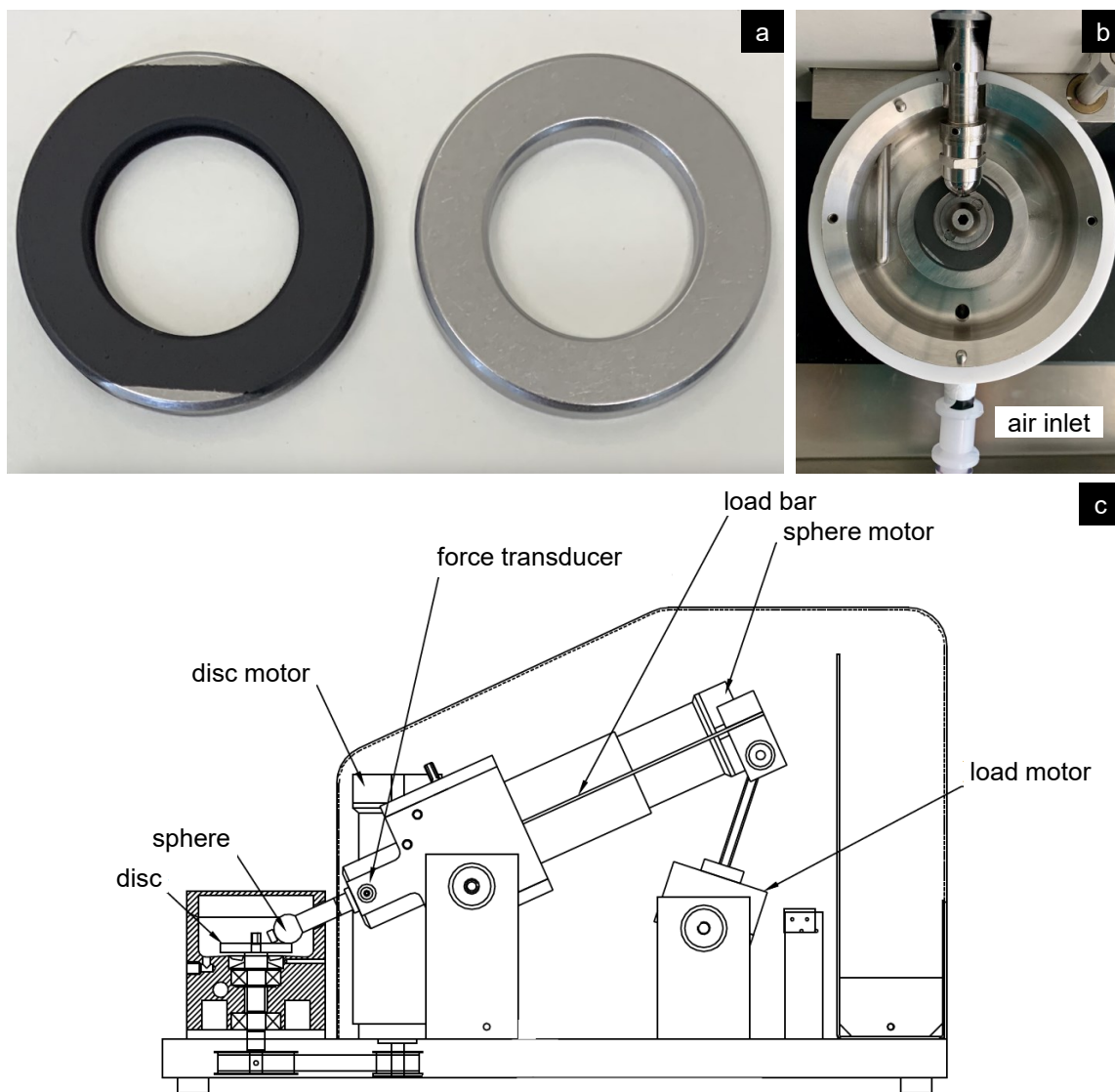
Figure 3.4: Mini traction machine. (a) steel bearing rings prior to and after coating process, (b) experimental chamber with mounted counterbody and pressurized air inlet, (c) technical drawing of the whole setup (modified from [70]).

To analyze the behavior of the graphite coating in rolling contact, experiments with a mini traction machine (MTM) (PCS Instruments Ltd, England) were conducted by

B.Sc. Antonia Neidhardt. The graphite coating was applied in the same way as for the microtribometer experiments but on commercially available steel rings instead of polished iron plates, see Figure 3.4a. The rings exhibited a roughness similar to other industrial surfaces with $S_a = 128\,nm$. The coating thickness was kept constant at $3.5\,\mu m$. By tuning the velocity of the plate and the rotating counterbody (1/2 inch 100Cr6 sphere), the slide-to-roll ratio (SRR) could be tuned to any desired value, in this work between 0 and $15\,\%$. To minimize the influence of humidity on the experiments, the MTM chamber was purged with dry pressurized air throughout the whole experimental duration, after a stabilization period of $20\,min$ prior to each experiment. For every experiment, a new counterbody and plate were used and the experiment repeated at least three times. The Hertzian pressure was again kept at an initial value of $1\,GPa$, thus a normal force of $15.6\,N$ was applied. The velocity was chosen to be $50\,mm\,s^{-1}$ as an intermediate compromise between the microtribometer and large-scale experiments conducted at the Institute for Product Development IPEK at KIT. A technical drawing of the MTM is depicted in Figure 3.4c.

3.4 Analysis Methods

3.4.1 Confocal Microscopy

For surface imaging and depth information of the samples, a confocal white light microscope Sensofar Plμ 2300 (Sensofar Tech S.L., Spain) was used. In the confocal microscope, white light is directed through a pinhole, focused on the sample, and afterwards directed through a LCD-micro display confocal to the focal point, onto the light recording element. The LCD-micro display functions as a switchable pinhole array. By a step-wise change of the distance to the specimen, a three-dimensional image of the target is generated. With the confocal microscope, the coating thickness was determined as described in Section 3.2. All images were taken at 20x magnification. Prior to and after the experiments, confocal images were recorded of both tribo-bodies to analyze the coating thickness and wear volume *ex situ*. A detailed description of the wear calculation can be found in the next Section (Section 3.4.1). The images were processed and analyzed with the Sensofar software SensoMAP 7.4.

Surface roughness parameters were determined by processing the confocal microscopy images with the software Vision 64 software from Bruker Corporation according to DIN EN ISO 25178-2. The image was straightened with an F-operator, outliers were removed by appropriate masking of the height histogram and a robust second-order Gaussian filter was applied. This filter is suitable for plateau surfaces and removes the filter and edge artifacts. Subsequently, the Abbott parameters S_k, S_{pk}, S_{vk}, and S_a were evaluated.

Wear

Due to the tribometric testing of the samples, they may have suffered from wear. The wear volume V of the plate was calculated by multiplying the length of the wear track with the average area of three sections perpendicular to it. These sections were positioned at 0.3, 0.5, and 0.7 mm distance from the start of the wear track. Due to an observed parabolic shape of the wear scar, this calculation method will lead to a slight overestimation of the wear volume. For the counterbody, the width D of the wear calotte was measured with confocal microscopy. The counterbody was wiped with acetone prior to wear measurements to wipe away particles and guarantee a precise determination of D. Together with the radius r of the sphere, the height h of the worn spherical cap could be calculated with Equation 3.3. The wear volume V of the sphere was then measured according to Equation 3.4 [32]. To yield the Archard wear coefficient k (see Equation 3.5) for both bodies, the wear volume V was divided by the applied load L and the overall sliding distance d.

$$h = r - \sqrt{r^2 - \frac{D^2}{4}} \tag{3.3}$$

$$V = \left(\frac{\pi h}{6}\right)\left(\frac{3D^2}{4} + h^2\right) \tag{3.4}$$

$$k = \frac{V}{L \cdot d} \tag{3.5}$$

3.4.2 Atomic Force Microscope

For some samples, a higher resolution image of the surface was needed than possible by confocal microscopy. For these cases, the surface of the unworn and worn samples was analyzed more in detail by atomic force microscopy (AFM). Due to the high expected roughness of the coating and substrate the images were recorded in tapping mode with a Bruker Veeco Dimension V AFM. The flexible cantilever with the AFM tip at its end is oscillated by a piezoelectric actuator at or close to its resonance frequency. The AFM probe is then lowered towards the sample surface until the AFM probe tip barely touches the surfaces and thus the oscillation is slightly dampened. The feedback loop maintains a constant AFM cantilever oscillation amplitude and hence a constant interaction force. Through the interactions with the surface, the phase shift of the cantilever oscillation changes, and thus rasterization of the surface record a topographic height map of the sample surface.

3.4.3 Scanning Electron Microscopy/Focused Ion Beam

To obtain high-resolution images of the sample surface at different magnifications, scanning electron microscopy (SEM) represented a suitable method. With a focused
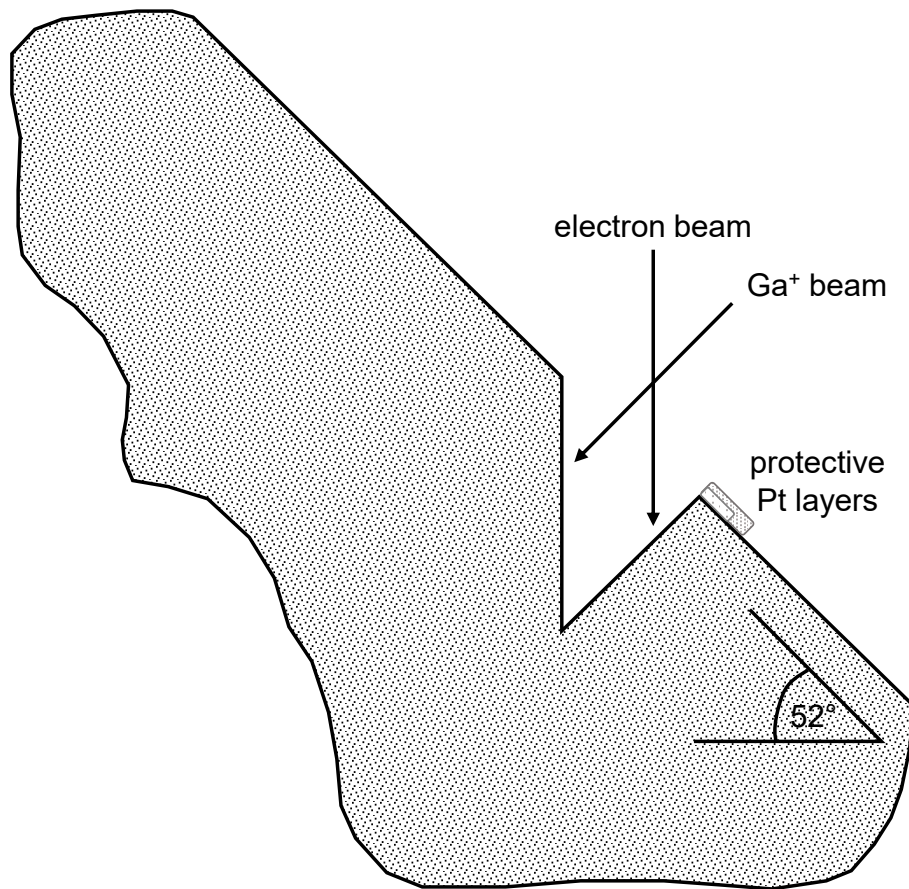
Figure 3.5: Schema of the cross section preparation principle with the 52° tilt of the sample and two protective Pt layers to protect the sample from damage during the preparation.

ion beam (FIB), the structure of the graphite coating as well as the underlying iron microstructure was analyzed prior to and after experiments. For these investigations, a dual-beam FIB scanning electron microscope (Helios NanoLabTM DualBeam 650, ThermoFisher Scientific, USA) was used. Cross sections were cut with the FIB by removing material via ion beam ablation, in this case with a Ga^+ ion beam. To protect the sample from beam damage, it was previously coated with two platinum layers. A first, thin layer ($\sim 0.2\,\mu m$) was deposited with the electron beam at an acceleration voltage of $2\,kV$ and a current of $6.4\,nA$. A second, thicker layer ($\sim 1\,\mu m$) was applied with the Ga^+ FIB at an acceleration voltage of $30\,kV$ and a current of $0.77\,nA$. Cross sections were cut perpendicular to the sliding direction to access information about the influence of the force distribution in the Hertzian contact. The Ga^+ FIB was used to cut cross sections at a width of $50\,\mu m$ and an angle of $52°$ with an acceleration voltage of $30\,kV$ and a current of $65\,nA$. Following this, a cleaning cross section was conducted with a current of $9.4\,nA$. Afterwards, the cross sections or the sample surface could be imaged by SEM at an acceleration voltage of $2\,kV$ and a current of $0.8\,nA$. During SEM the sample is examined with an electron beam, which leads to

beam-substrate interactions. Secondary electrons (SE), backscattered electrons, and X-rays are emitted. For their detection, various detectors are available. The images presented in this thesis were recorded with an "out-of-the-lens" Everhart-Thornley-Detector (ETD).[71]

3.4.4 Transmission Electron Microscopy

Transmission electron microscopy (TEM) was helpful in cases where a deeper insight into the individual graphene layers' structure was needed. TEM offers a significantly higher resolution and a higher contrast than SEM images. For the TEM lamellae preparation, a thin Pt protection layer was deposited on the sample surface via a Pt target. Afterwards, a thicker Pt layer was deposited on the region of interest for further protection and an electron-thin lamella was prepared. First, a cross-section was prepared by FIB milling using an FEI Strata 400 dual-beam instrument.

Coarse FIB milling was done at 30 kV accelerating voltage with Ga^+ ions, whereas for final polishing of the sample surfaces (ca. 5000 scans at each side) 5 kV with approximately 70 pA ion current was used. The TEM investigations were carried out with an FEI Titan3 80-300 (Thermo Fisher Scientific, Waltham, USA) equipped with a Gatan imaging filter of the type Tridiem 865 ER (Gatan Inc., Pleasanton, USA). All the TEM sample preparation and analyses were conducted by the group of Prof. Reinhard Schneider of the Laboratory of Electron Microscopy (LEM) at KIT.

3.4.5 Electron Energy Loss Spectroscopy

To gain further insight into the structural properties of the graphite coating, electron energy loss spectroscopy (EELS) analyses were conducted. For EELS measurements, an extremely thin sample that allows the surpassing of electrons is needed. EELS is a family of techniques where the sample is penetrated with electrons of defined energy (between 100 to 1000 keV). As the electrons surpass the sample, they interact with the atoms, hence information about the atomic structure and chemical properties of a sample can be drawn. Most of the electrons surpass the sample without losing energy, but some will lose energy due to inelastic scattering, which leaves the latter in an excited state. When leaving this excited state, energy is emitted either as visible photons, x-rays, or Auger electrons (see Figure 3.6). The initial, incident electron loses energy due to this interaction, which is detected with the spectrometer [73]. Usually, interactions with the inner electron shells of the atom (such as the carbon K edge) are most frequently analyzed for material composition detection [74]. Here, the incident electron ray interacted with an electron from the K-shell of the carbon atom, hence the innermost shell according to the model of Bohr, which corresponds to the C1s orbital [10].

The Titan microscope was operated in the scanning TEM (STEM) mode at 300 kV, during which an area of 20×20 nm was scanned to reduce possible changes of the
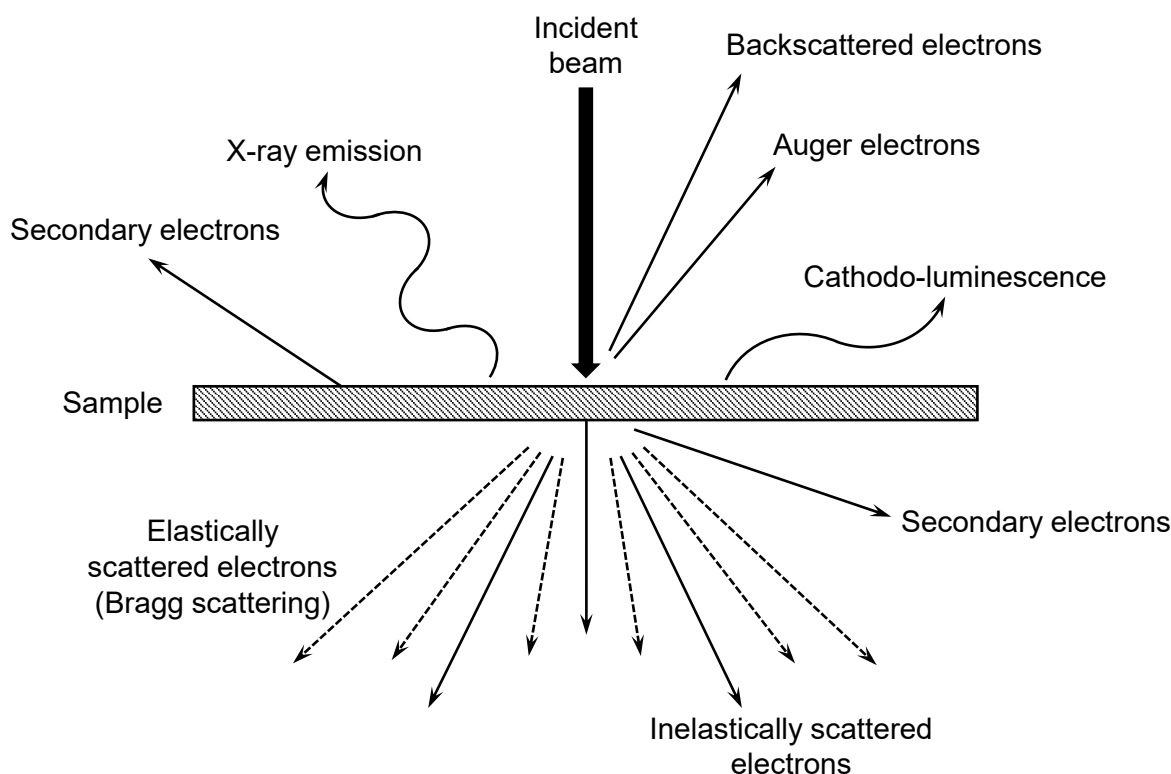
Figure 3.6: Schematic diagram of the different interactions created when a high-energy electron beam passes through a thin TEM sample (modified from [72]).

chemical bonding of carbon atoms. To record the carbon K-edge at 284 eV, multiple spectra were taken and integrated ranging from about 200 to 610 eV with a dispersion of 0.2 eV per channel. The full width at half maximum (FWHM) of the zero-loss peak was analyzed and resulted an energy resolution of approximately 0.7 eV. A typical measuring time for the acquisition was 1 to 3 s, and several spectra were accumulated for each region of interest. The spectra were processed with background subtraction and deconvolution to correct for multiple scattering due to varying thickness; for these steps, the DigitalMicrograph software (Gatan) was used.

For carbon-based materials, the carbon K-edge is of major interest, which shows the π^* and σ^* anti-bonding (unoccupied) states for differently hybridized carbon atoms. To determine the amount of sp^2 and sp^3 hybridized C atoms, the intensity ratio between both peaks has to be calculated. To do so, the two-window method was used for the integration of the two peaks – for this method, the definition of the windows is crucial [74]. In this work, the following range was used for the integration of the peaks (as used by [75]): 284.7 - 285.3 eV for π^* states and 292 - 307 eV for σ^* states. The sp^2 content will be influenced by the ion-induced damage during the lamella preparation [74]. However, as the samples investigated in this thesis are of quite similar nature, they can still be safely compared in a relative manner.

3.4.6 X-Ray Photoelectron Spectroscopy

Some of the samples were analyzed by X-ray photoelectron spectroscopy (XPS) to investigate the chemical composition and binding states of the carbon coating. A PHI 5000 Versaprobe II (ULVAC-PHI, Japan) spectrometer with 15 keV monochromatic Al-Kα X-rays and an energy resolution of 0.2 keV was used. This measurement technique relies on the photoelectric effect, which occurs if a sample is investigated by X-ray radiation and hence a photoelectron is released. Its kinetic energy can be measured with an analyzer to determine its binding energy with which the chemical components and their binding states can be determined. The latter is due to the fact that the work function and thus binding energy of an atom changes if it forms a bond with different other atoms. [10]

As photoelectrons only exhibit a free path length of a 5-10 nm (depending on their kinetic energy), XPS is used for surface-sensitive applications were the first 5 nm are of interest [76]. However, it is possible to obtain depth information by sputtering the sample with ions (in this case Ar^+ ions) with intermediate measurements in the sputtering area. For a proper resolution, a high vacuum of $\leq 10 \cdot 10^{-6}$ mbar is crucial.

Surface measurements were conducted with a sputtering spot of 200×200 µm over the range of 0 to 1400 eV with a pass energy of 187 eV for the whole spectral range and at 23 eV to analyze the exact atomic percentages. For depth profiles, a pass energy of 47 eV was used while sputtering with an Ar-ion canon at 1 kV and 500 nA which leads to a sputter rate of 2 nm/min (calibrated over a SiO_2 standard).

3.4.7 RAMAN Spectroscopy
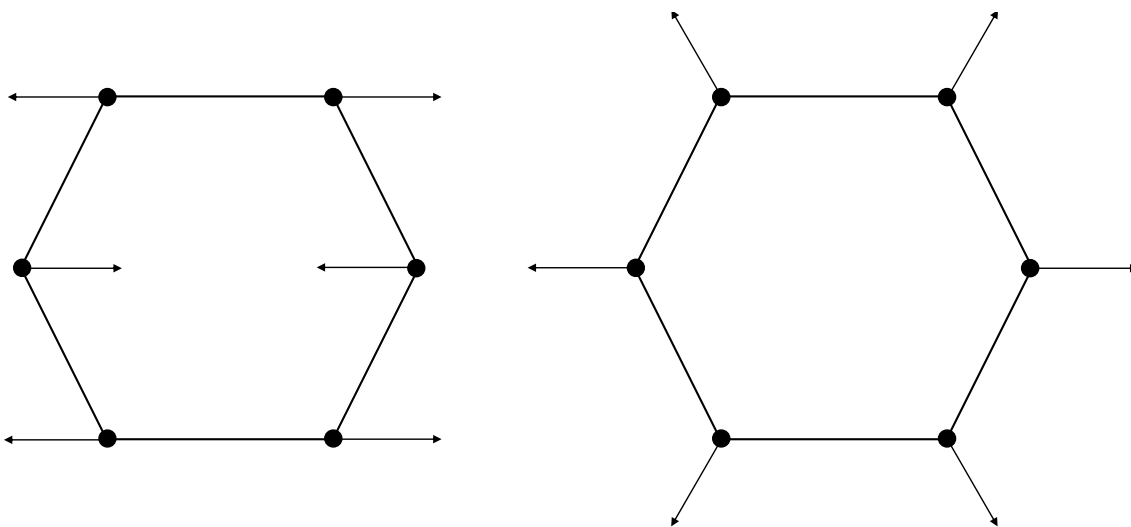
Figure 3.7: Left side: E_{2g} G mode, right side: A_{1g} D breathing mode (modified from [77]).

For larger regions of interest, the nondestructive, bulk method of Raman spectroscopy can be used. The method is based on the inelastic scattering of light caused by the so-called Raman effect as the sample gets analyzed with a monochromatic laser beam. In this thesis, green laser light at a wavelength of 632 nm was used to determine the vibrational modes of molecules. In inelastic/Raman scattering, the photons from the laser shift the valence electrons of atoms into higher energy levels. As the electrons fall back into their original energy level, they emit energy in form of an electromagnetic wave in all directions, which can be detected as Raman scattering. Due to the high energy, the photons penetrate deep into the sample, hence Raman is not surface sensitive and rather used as a bulk analysis method. In this work, Raman spectra were recorded at frequencies ranging from 100 to 3000 cm^{-1}. Three spectra were measured for 10 s each at a 100x magnification.

For carbon, the D (1350 cm^{-1}) and G band (1580-1610 cm^{-1}) are the most important features of the spectra frequently analyzed. The D motion corresponds to the A_{1g} breathing mode (see Figure 3.7 right side) and is forbidden in perfect graphite. It arises only in disordered graphite and in the presence of sixfold aromatic rings. The G motion originated from the E_{2g} mode (left side of Figure 3.7) and is connected to the motion of sp^2 carbon atoms, hence it is observed for carbon chains as well.[77] Another important feature often analyzed for carbon-based Raman spectra is the intensity ratio, where the D band intensity is divided through the G band intensity. During the scope of this thesis, the intensity ratio is calculated from the height of the peak maxima. All Raman analyses were conducted by the author at Campus North with a Raman-spectrometer LabRAM Soleil (HORIBA Europe GmbH, Germany).

4 Results: Sliding Friction

4.1 Coating Method

In the first part of this dissertation, the graphite lubrication and wear mechanisms are investigated under sliding friction and high mechanical load. For the graphite application on polished iron substrates, four different coating techniques were investigated: 3D printing, dip coating, spin coating, and airbrushing. Upon testing out the application methods, the following requirements were defined:

- reproducibility of the application method
- tunability of the coating thickness
- homogeneity of the coating

With the 3D printer used in this study (Stepcraft 600 CNC system with a ViproHead 5 printer head), no tunable coating thickness nor a homogeneous morphology was achieved due to the extrusion-like method of the application. The drop coating was conducted manually and yielded no reproducible result. With the spin coating, the thickness was not adjustable in the desired thickness range as all produced coatings exhibited a thickness in the nanometer range. Confocal images of these three coating methods are summarized in 4.1. Eventually, only the application of a commercially available graphite suspension with an airbrush pistol (see Section 3.2) fulfilled all requirements. Hence, this thesis focuses on graphite-coated iron samples produced with this coating method.
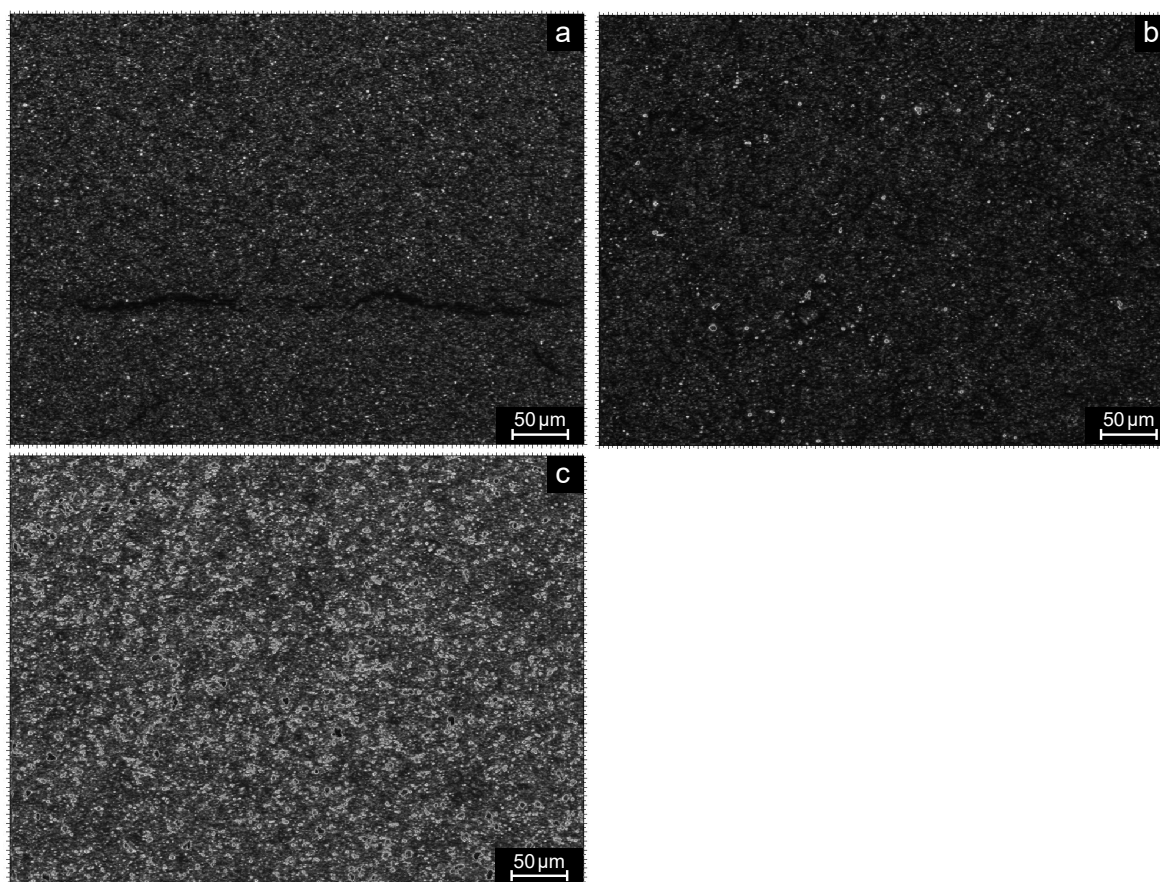
Figure 4.1: Confocal microscopy images of the different tested deposition methods. (a) extrusion printing, (b) drop coating, and (c) spin coating at 1500 rpm.

4.2 Cleaning Procedure of the Counterbody

For the microtribometer experiments, the spherical counterbodies (100Cr6 sphere, 2 mm) were glued with cyanoacrylate-based glue onto the double-leaf cantilevers. Due to its small size, the glue might get pulled along the sides of the sphere due to capillary forces and thus cover it completely. To avoid this, the counterbodies were cleaned with acetone and isopropanol prior to any microtribometer experiment. A series of XPS analyses was hence conducted to analyze the spherical surface: An analysis of the steel sphere without gluing, a glued sphere where no cleaning procedure was conducted, and a glued sphere after conducting the cleaning procedure. The resulting XPS surface analyses are depicted below in Figure 4.2.

Displayed are the most relevant chemical elements: Carbon (C), oxygen (O), nitrogen (N), and iron (Fe). On the initial, non-glued 100Cr6 sphere the surface consists of carbon and oxygen, with a small amount of nitrogen and iron. Hence, as often observed for steel surfaces, a thin iron oxide layer covers the steel sphere as well as airborne contaminants. If glue was added (grey bars in Figure 4.2) less carbon was measured, more oxygen, and distinctly more nitrogen, amounting to 10.3 at. %. Especially the

nitrogen content can hence be used as a marker for the cyanoacrylate on the surface.
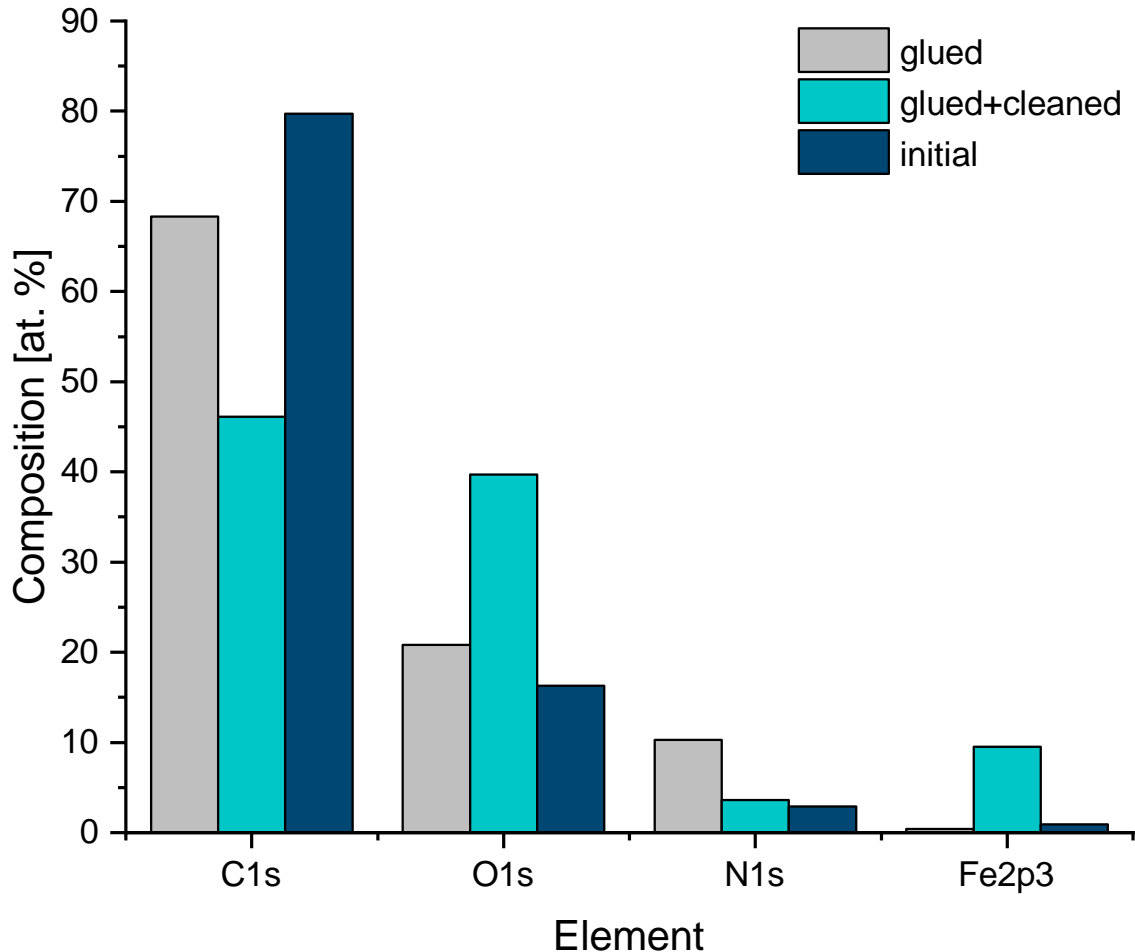
Figure 4.2: Chemical composition of the glued and cleaned spheres as determined by XPS.

After the cleaning procedure with acetone and isopropanol, the nitrogen content is on a similar level (3.6 at. %) as the initial state (2.9 at. %). In addition, an increase in oxygen and a decrease in carbon is measured compared to the initial state. This observation presumably is due to the removal of the airborne, carbon-based contaminants and hence the underlying iron oxide layer of the steel sphere was revealed. An increased amount of iron (9.5 at. %) detected on the surface supports this theory. In conclusion, glue residues from the sample preparation process could successfully be removed with the established cleaning process and thus contamination of the tribological experiment is avoided.

4.3 Morphology of the Coating

The chosen deposition method with an airbrush spray gun created a dark and dense coating with no visible defects. For a clearer image of the coverage, morphology, and structure of the coating, SEM images of the coating surface and a cross section were taken (displayed in Figure 4.3 and Figure 4.4). In the SEM surface images, it becomes evident that the deposition method yielded a homogeneous coating that covered the entire substrate. Larger clusters are visible as roughness peaks, presumably due to varying particle sizes in the suspension and clustering effects. An average particle size of 0.5-1 µm was determined from the high magnification images in Figure 4.3d.

For investigations of the graphite coatings' structure FIB cross-sections were prepared (Figure 4.4). The dried graphite coating consists of individual flakes stacked randomly on each other, with pores in between which led to a slight curtaining effect during the cross section preparation. As evident from the analyses, the coating thickness varies depending on the analyzed area.
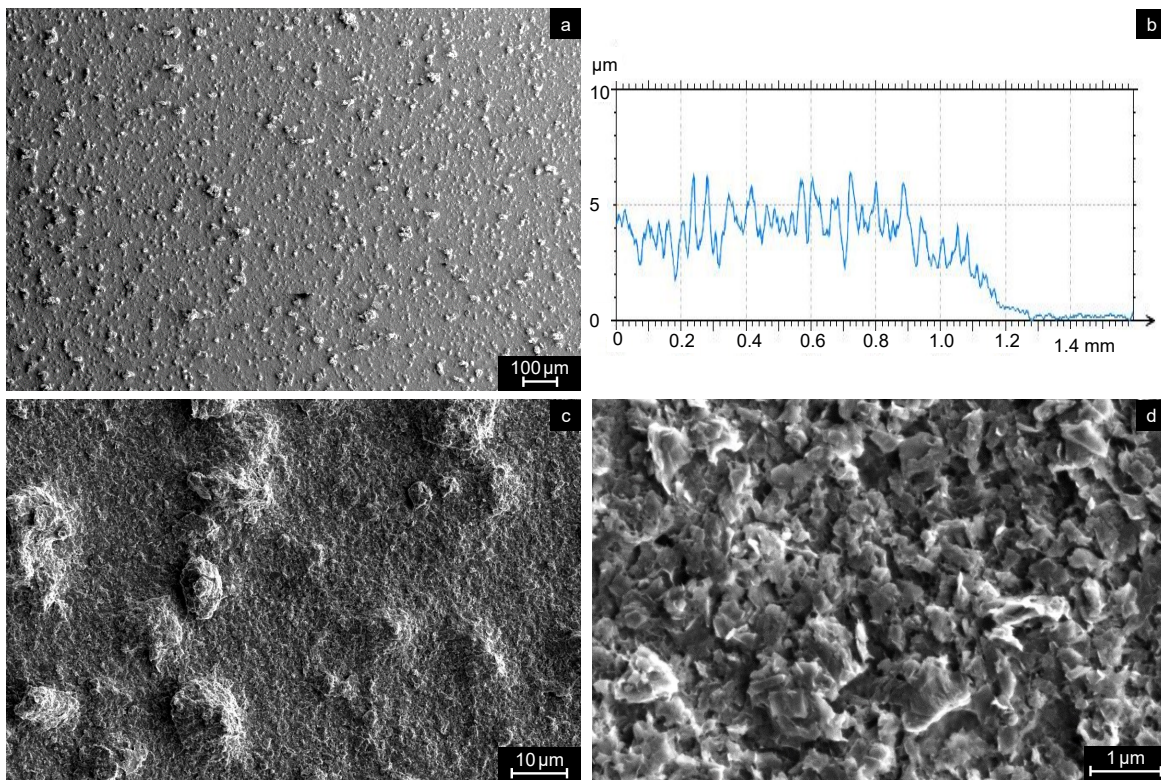
Figure 4.3: SEM images (a,c,d) and roughness profile (b) of the as-deposited coating via the airbrush spray gun method.
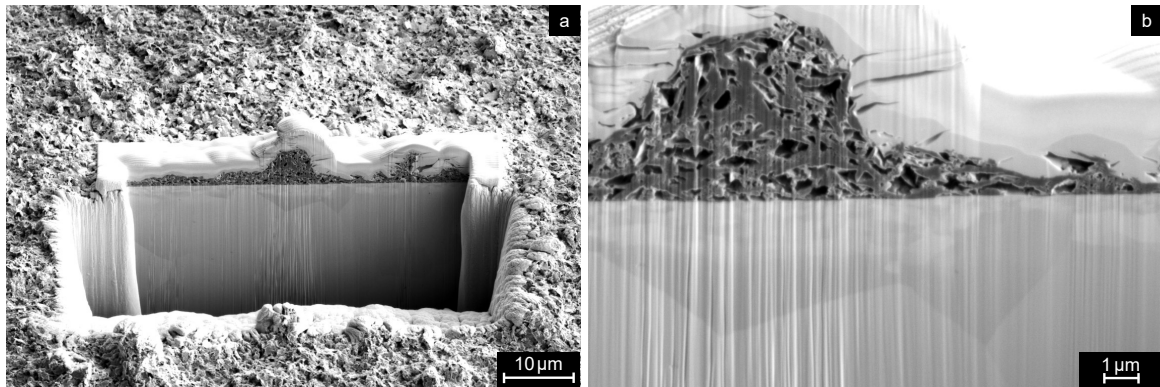
Figure 4.4: SEM images of the FIB cross sections cut into the as-deposited coating on mirror-like iron plates as a substrate with a roughness of $S_a = (11 \pm 2)\,\text{nm}$.

4.4 Mechanical Behavior of the Coating

4.4.1 Behavior under Compression

How do the porosity and the surface roughness of the coating influence its mechanical behavior? To answer this question properly, load-retract microtribometer experiments were conducted and the results published [78]. Two normal forces were tested for an additional evaluation of the force influence on material transfer onto the counterbody: 69 mN and 402 mN (Hertzian contact pressures of 560 and 1008 MPa). After the desired normal force was reached, the indenting body was automatically retracted.

As visible by confocal microscopy in Figure 4.5, indentation with a steel sphere sufficed to flatten the roughness peaks of the graphite coating (seen as brighter areas in the middle of the image) and presumably compacted the porous structure. Upon inspection of the counter body, small graphite flakes were visible on them, hence material transfer occurs and no shearing is needed.

To test the hypothesis of compression occurring during indentation and to investigate the differences between the two normal forces, cross sections were cut by FIB, and SEM images were taken. The cross sections were cut in the middle of the indentation area and their width was adjusted accordingly to cover the whole width, hence 30 μm for the 69 mN sample and 70 μm for 402 mN. For compression quantification of the graphite coating, multiple length measurements were taken by eye with the SEM at both the uncompressed side of the cross section (Figure 4.6b,e) and in the compressed middle (Figure 4.6c,f).

As seen in Section section 4.3, the initial coating exhibits a high surface roughness and local deviations of the coating thickness. To take this effect into account, an error of 5% was defined for the visual length measurements. For the lower normal force of 69 mN, the thickness determination derived 3.65 μm thickness at the uncompressed side and 3.02 μm in the indentation middle. The coating was thus indented by $(0.63 \pm 0.03)\,\text{μm}$
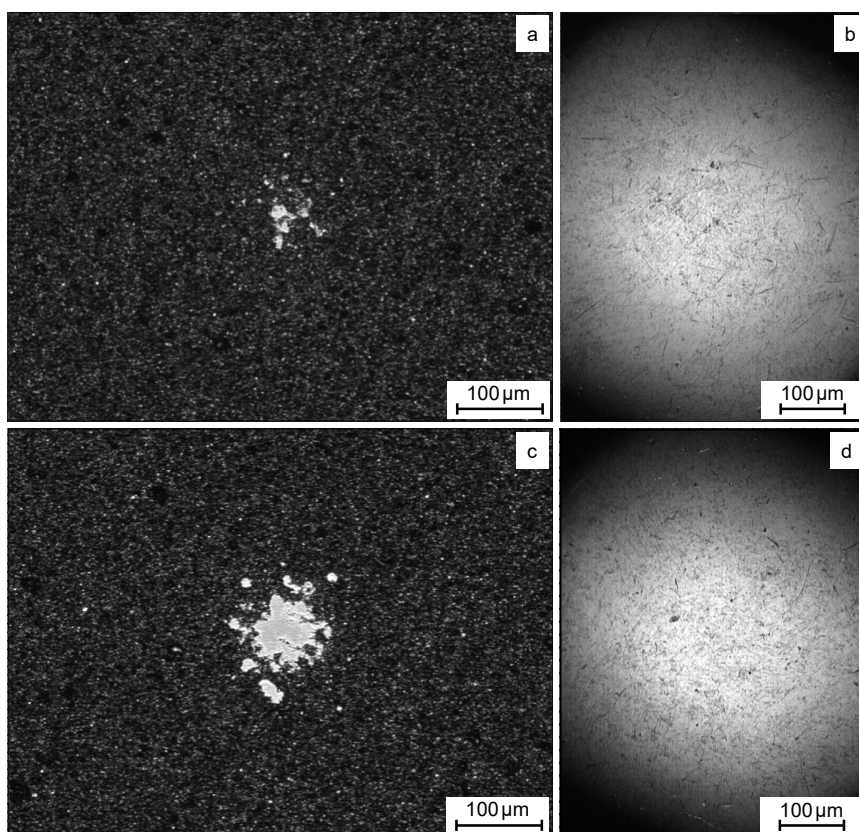
Figure 4.5: Confocal microscopy images after indentation at (a,b) 69 mN and (c,d) 402 mN. These experiments were conducted with polished iron plates as a substrate which were polished to a rougher finish, $S_a = (70 \pm 1)$ nm.

after a first contact, hence $(17.31 \pm 0.86)\%$ compression occurred. For 402 mN the coating was compressed by (0.86 ± 0.04) µm, thus $(34.51 \pm 1.73)\%$.

4.4.2 Behavior under Compression and Shear

As evident from the previous section, a material transfer takes place at the first initial contact. To elucidate how this transfer develops if shearing is initiated, an experiment was conducted on graphite-coated iron plates with a mirror-like finish and at a normal force of 69 mN. The experiment was stopped after different durations: 10, 20, and 300 cycles and the results are published in [79]. As evident from Figure 4.7a and b the material transfer onto the counterbody increases in the first 10 cycles. On the graphite-coated plate, the roughness peaks of the coating (darker spots) get flattened and the layer is compressed, as observed as well for the indentation experiments. After 20 cycles (Figure 4.7c and d) these effects are increased. In addition, some small patches of the coating start to delaminate, visible as small bright areas where the iron substrate is revealed. After 300 cycles, even larger areas delaminated. At a later point (see
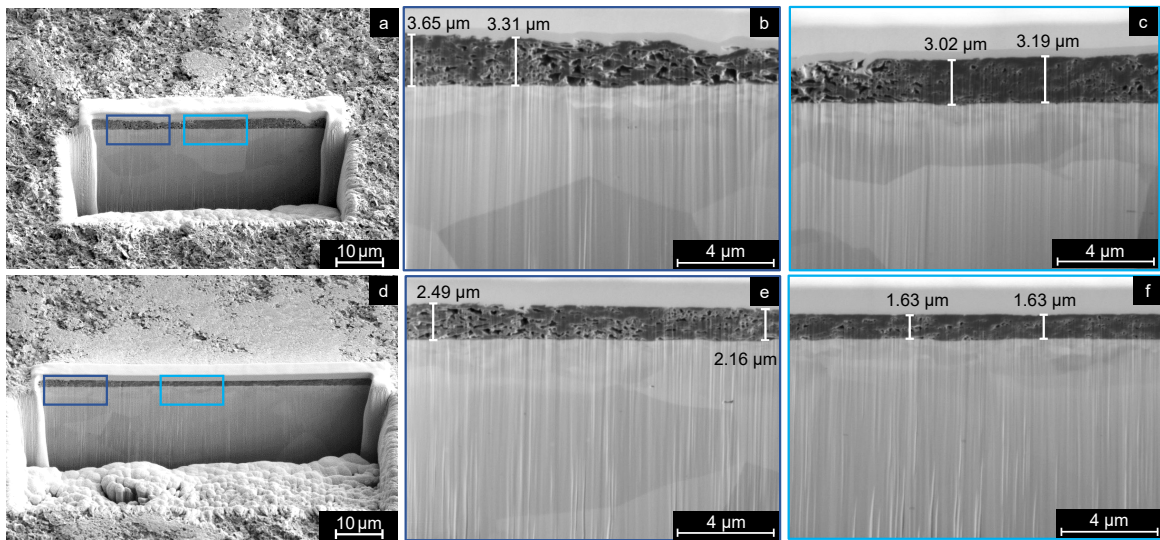
Figure 4.6: Scanning electron microscopy images after indentation at (a,b,c) 69 mN and (c, d, e) 402 mN taken at an acceleration voltage of 2 kV and a current of 0.8 nA. Adapted from [78].

Figure 4.10a), this patch-wise delamination leads to the complete reveal of the iron substrate.
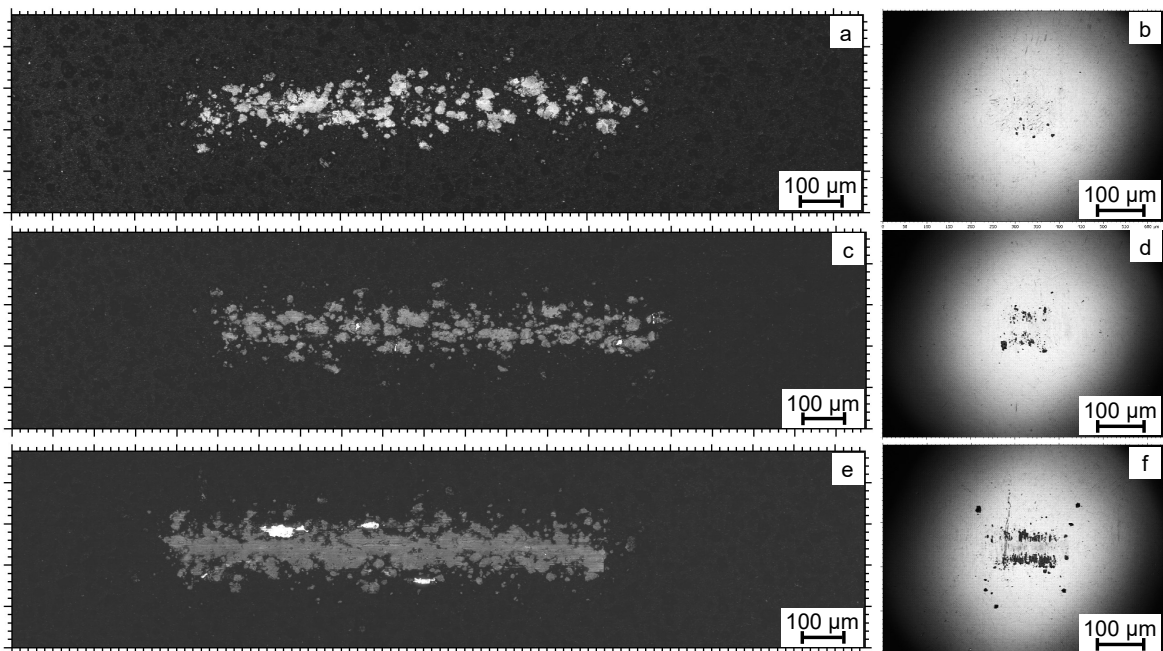
Figure 4.7: Confocal images of graphite coated plates (left) and counterbodies (right) after friction experiments at 69 mN and a layer thickness of 3.5 µm stopped after differing experimental duration. (a,b) 10 cycles, (c,d) 20 cycles, (e,f) 300 cycles. Sliding occurred in a reversing fashion from right to left for the wear tracks and from down to top for the steel spheres. From [79].

4.4.3 Discussion

In summary, the application method with an airbrush pistol created a porous, poly-crystalline, and soft coating. Material transfer onto the counter body immediately takes place upon the first contact, thereby leading to a graphite-graphite friction interface for the majority of the experimental time. This phenomenon is known and has been reported by e.g. Merkle and Marks for graphite-tungsten single asperity contacts [35]. Upon indentation, the coating gets compressed; at 402 mN by 50.2% more than at 69 mN [78]. Hence, the degree of compression correlates well to the Hertzian pressure: at 402 mN a Hertzian pressure of 1008 MPa is expected, which is 55.6% higher than at 69 mN. Of course, one has to note that only two data points were considered for this correlation - more experiments are needed to evaluate whether the increase follows a linear or exponential trend. However, the FEM simulations conducted by Joerger et al. allowed them to calculate the yield stress of the porous graphite coating, which lies at circa 40 MPa.

Upon shearing, wear seems to take place first as transfer onto the counterbody while compression of the coating occurs. Following that, the coating gets worn away layer by layer while simultaneously delamination of patches occurs [79]. Presented in this section are sliding results at 69 mN but delamination will supposedly increase at higher normal forces due to increased shear forces. This hypothesis is tested in the next section.

4.5 Variation of the Thickness and Normal Force

In this parameter study, the normal force and graphite coating thickness were tailored to elucidate the influence on the friction, lifetime, wear, and the delamination behavior. The tested normal forces were specifically: 69, 165, and 402 mN, which results in Hertzian pressure of 560, 750, and 1008 MPa. Five different thicknesses ranging from 0.2 to 17 µm (see Table 4.1) were applied on mirror-like substrates and their influence on the tribological properties analyzed. The results presented and discussed in this chapter 4.5 were previously published in [79].

2D and 3D roughness parameters were determined (on multiple samples at different places) for all samples according to ISO 25178. As the average roughness S_A is the parameter listed most in literature publications, it was used for a first comparison, see Table 4.1. The arithmetic mean roughness S_A generally increased at higher thickness. The substrate exhibited a low surface roughness of $S_A = 0.01$ µm and a mirror-like finish. All experiments were repeated at least three times for 500 cycles, a velocity of 0.1 or 0.5 mm s^{-1} and at the three different normal forces. To rule out any influence of humidity changes, all experiments presented in this section 4.5 were conducted while purging the experimental chamber with dry pressurized air, hence a relative humidity of $\leq 5\%$ RH.

Table 4.1: Thickness and roughness parameters for samples produced on a mirror-like (ML) substrate.

Sample	Thickness [µm]	S_A [µm]
ML uncoated	0	0.01
ML-1	0.2	–
ML-2	3.5	1.05
ML-3	6	3.01
ML-4	10	2.38
ML-5	17	11.6

4.5.1 Friction

Visualized in Figure 4.8 is the coefficient of friction (CoF) plotted vs. the full experimental duration in (a) and the steady-state-CoF vs. the tested layer thicknesses in (b,c, and d). For the plot in (a), the raw data of the microtribometer was run through a MATLAB script (written at the Leibniz Institute for new Materials, Saarbruecken, Germany) adapted by Markus Stricker to fit the requirements of the Tetra microtribometer. The script is used to deduct the first and last 10% data of each cycle to only consider the relevant portion in sliding motion and exclude the static friction. The remaining data is averaged to gather one value for each cycle. Error bars always represent the standard error of the mean.

The steady-state CoF values in Figure 4.8 were calculated by averaging over 10 cycles each, either at the experimental end or before a CoF increase occurred. The moment of this steep increase depended on the graphite coating thickness and normal force. From now on the steep increase is denoted as the "lifetime" of the coating and defined as the cycle at which the CoF exceeded the average of the previous ten cycles by 30%. Presented in Figure 4.8a, b, and c is the general trend: with a layer thickness increase, the steady-state CoF increased for all tested normal forces. The lowest CoF was always achieved with the thinnest coating (0.2 µm) and it increased by up to 3.6 times for the largest coating thickness (17 µm). In comparison to the unlubricated steel-iron contact (dashed black line), friction was reduced by up to five times. Depicted in Figure 4.8d is a second trend: an increase in normal force led to lower friction. This observation was the same for all tested coating thicknesses.

4.5.2 Lifetime

Previous studies on the stability of carbon-based lubricants revealed an overall limited lifetime of the lubricant, as it ruptures easily when exposed to large normal forces and therefore large shear forces [41, 44, 46, 47]. As visible from Figure 4.8a, this
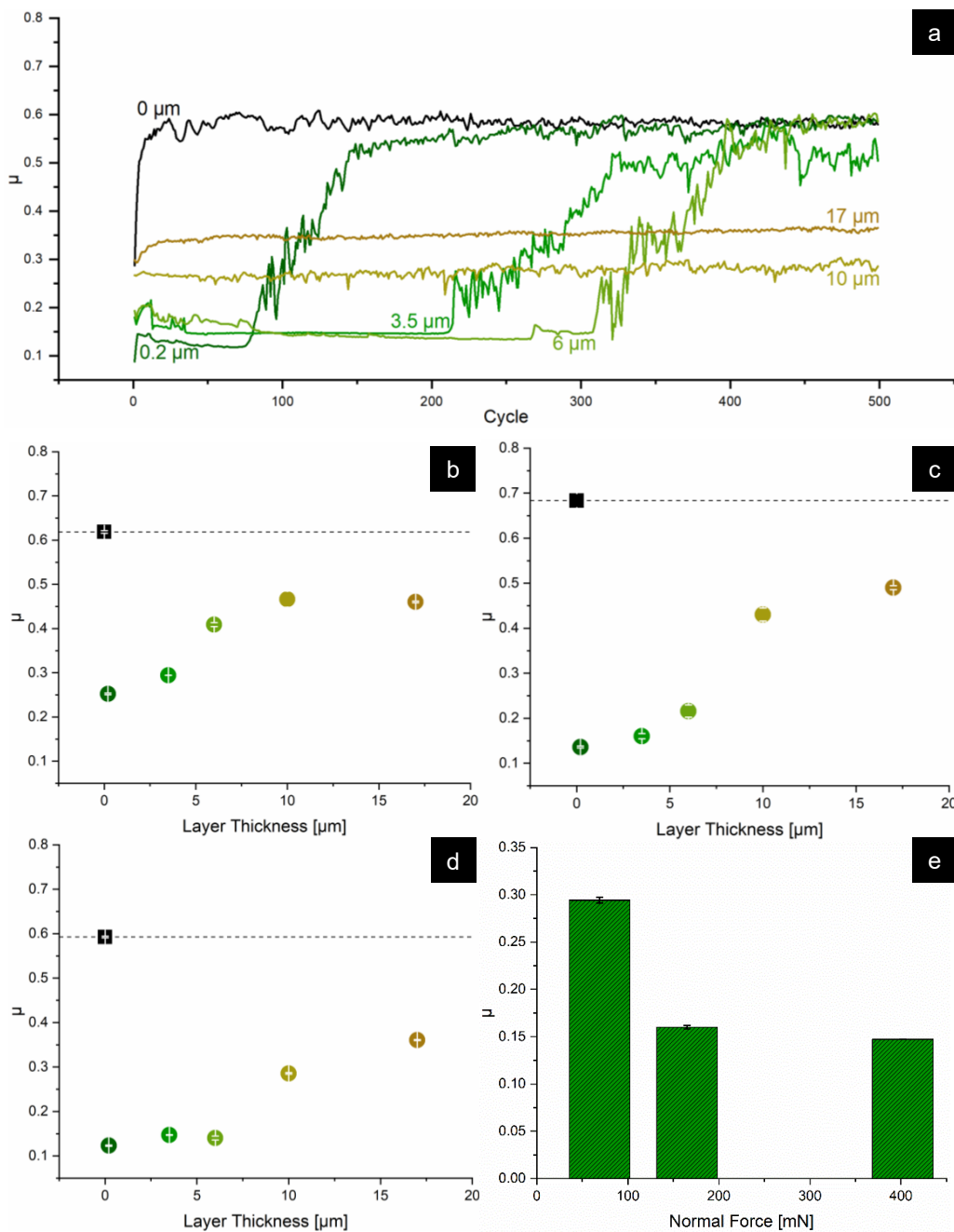
Figure 4.8: Coefficient of friction (µ) of coated mirror-like iron versus a 100Cr6 ball at different graphite layer thicknesses and normal forces. (a) CoF during the experiment, (b) average CoF at 69 mN normal force, (c) at 165 mN, (d) at 402 mN, and (e) CoF at 3.5 µm thickness over tested normal forces. The dotted black line in b-d represents the value of an unlubricated contact. From [79].

rupture most likely occurs during the microtribometer experiments as well. Figure 4.9 summarizes the average lifetime for the different coating thicknesses and normal forces.
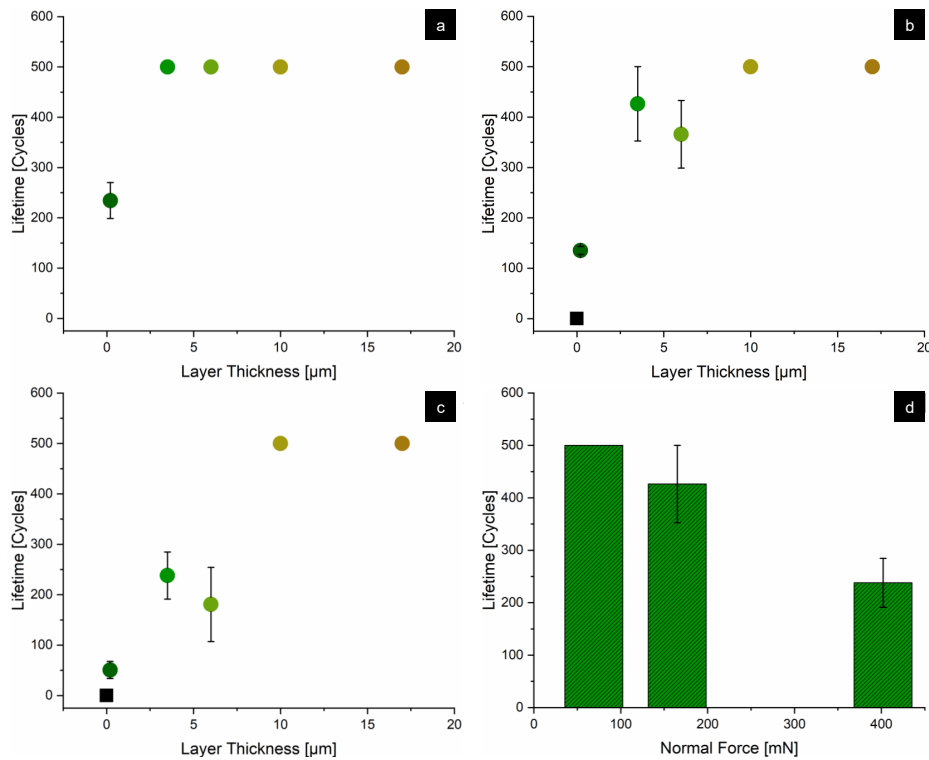
Figure 4.9: Lifetime of a graphite-coated mirror-like iron versus a 100Cr6 ball at different graphite layer thicknesses and normal forces. a) average lifetime at 69 mN normal force, b) at 165 mN, c) at 402 mN, and d) CoF at 3.5 μm thickness over tested normal forces. From [79].

At 500 cycles the experiment was stopped, thus this marks the maximal longevity.

For the uncoated contact, a protective layer of iron oxides and other adsorbates is expected at the surface (see XPS results in Section Figure 4.2). This layer quickly wore away, hence the bare steel-iron pairing exhibited a lifetime of 0 cycles for all normal forces (see black marks in Figure 4.9). Graphite as a solid lubricant improved the lifetime for all coating thicknesses and normal forces. Overall, an increase in coating thickness led to an increased longevity of the tribo-bodies. In addition, the coating lifetime is not only influence by the coating thickness, but by the normal force as well: Figure 4.9d depicts the trend at 3.5 μm coating thickness. This negative trend was observed for all coating thicknesses – a normal force increase led to a lifetime decrease. This decreased lifetime could presumably be due to an increase in wear and will be discussed in Section 4.5.5.

4.5.3 Wear

One reason for the short longevity of the graphite coating could be an high tendency to tear and hence increased wear. To investigate this hypothesis and understand the

wear mechanism of graphite, the microtribometer samples were analyzed after the experiments by confocal microscopy. While all thickness and normal force pairings were analyzed in this way, the coating thickness of 3.5 µm was selected for the display in Figure 4.10. This coating thickness was selected as the experiments conducted with it yielded the best tribological performance, as later on described in Section 4.5.5 . In these images, two-fold material transport became visible: On the one hand, graphite got transferred onto the counterbody, thus forming a graphite transfer layer. This layer formation in turn means that a graphite-graphite friction surface prevails during the experiment. These results are in coherence with the indentation experiments described in Section 4.4.1. On another hand, graphite got pushed aside and built up at the reversal points of the wear track. While these observations were reported for all coating thicknesses and normal forces, a clear increase of wear is visible with an increase in normal force. At 402 mN (see Figure 4.10e,f) abrasive and adhesive wear is visible on both tribo-bodies due to cold welding and the consecutive formation of hard abrasion particles.
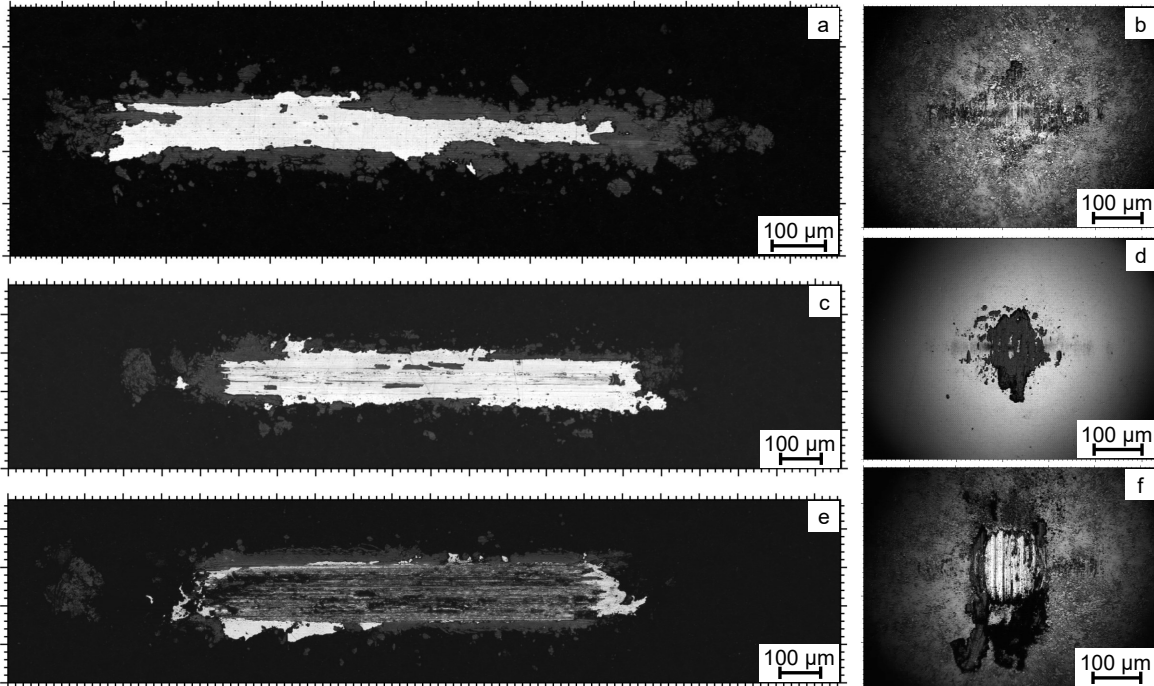
Figure 4.10: Confocal microscopy images of graphite coated iron plates (left column) and their respective steel counterbodies (right column) after the experiments at different normal forces. (a,b) at 69 mN, (c,d) at 165 mN, (e,f) at 402 mN, all at 3.5 µm coating thickness. From [79].

To quantify the increased wear at higher normal forces, the wear volume was determined as described in Section 3.4.1 by confocal microscopy for both the plate and the counterbody. Figure 4.11 depicts the normalized wear coefficients according to the Archard relationship for the graphite coatings and its underlying iron substrate. Due to the *ex situ* determination of the wear volume, no distinction between the wear of
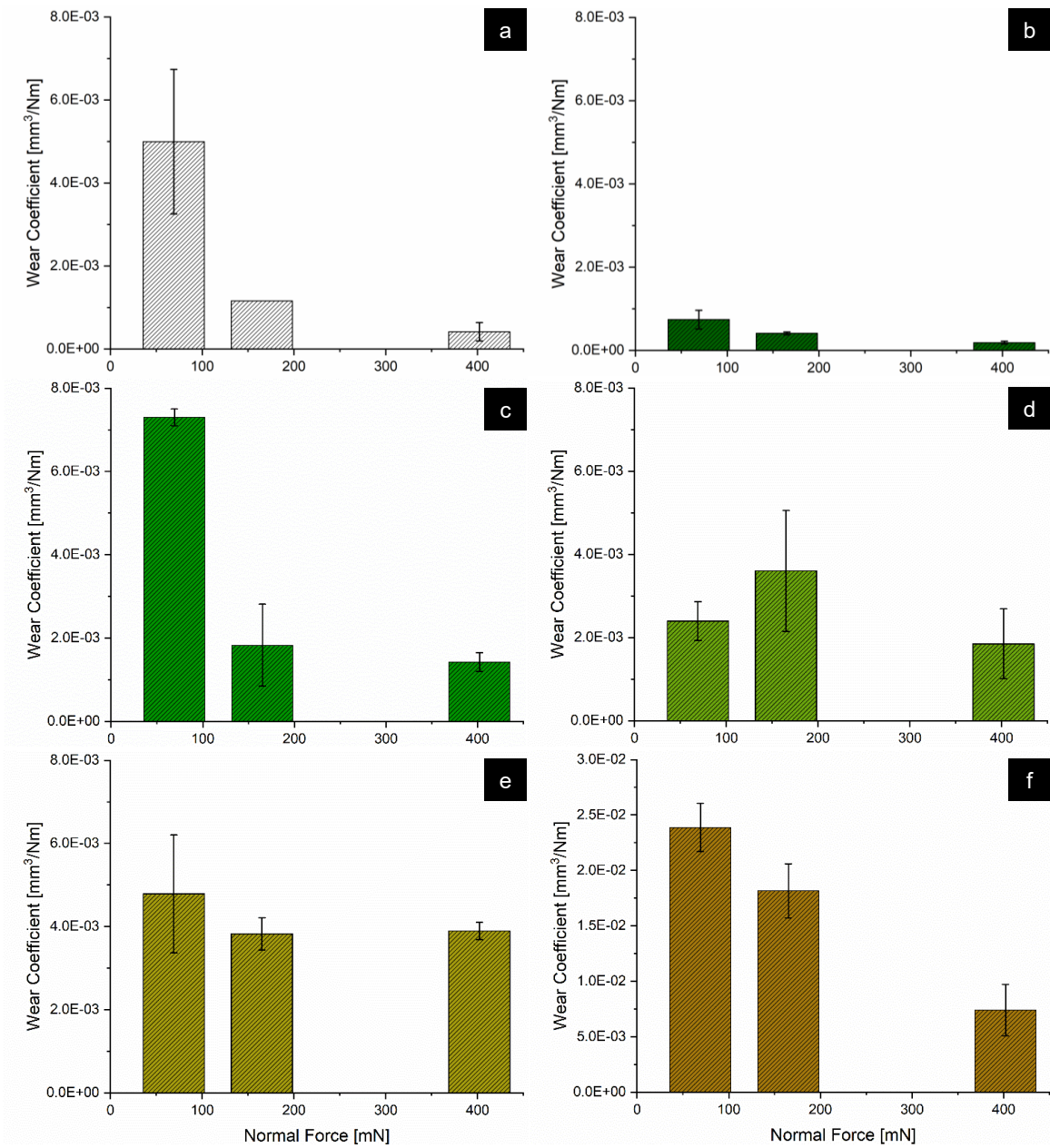
Figure 4.11: Normalized wear coefficients of the coated iron plate over normal force for all tested graphite film thicknesses: (a) 0 µm, unlubricated contact, (b) 0.2 µm, (c) 3.5 µm, (d) 6 µm, (e)10 µm, (f) 17 µm. Note the change in scale for Figure 4.11f. From [79].

the solid lubricant and the substrate is possible. In general, the wear coefficient of the plate followed a similar trend as the CoF in terms of the normal force dependence. A normal force increase led to a wear coefficient decrease. The coating thickness influenced the wear coefficient as well: for thicker coatings, an increase in wear was measured. The experiment at 69 mN and 3.5 µm coating thickness strays away from this trend. Here, extensive wear was observed. The images in Figure 4.10a displayed
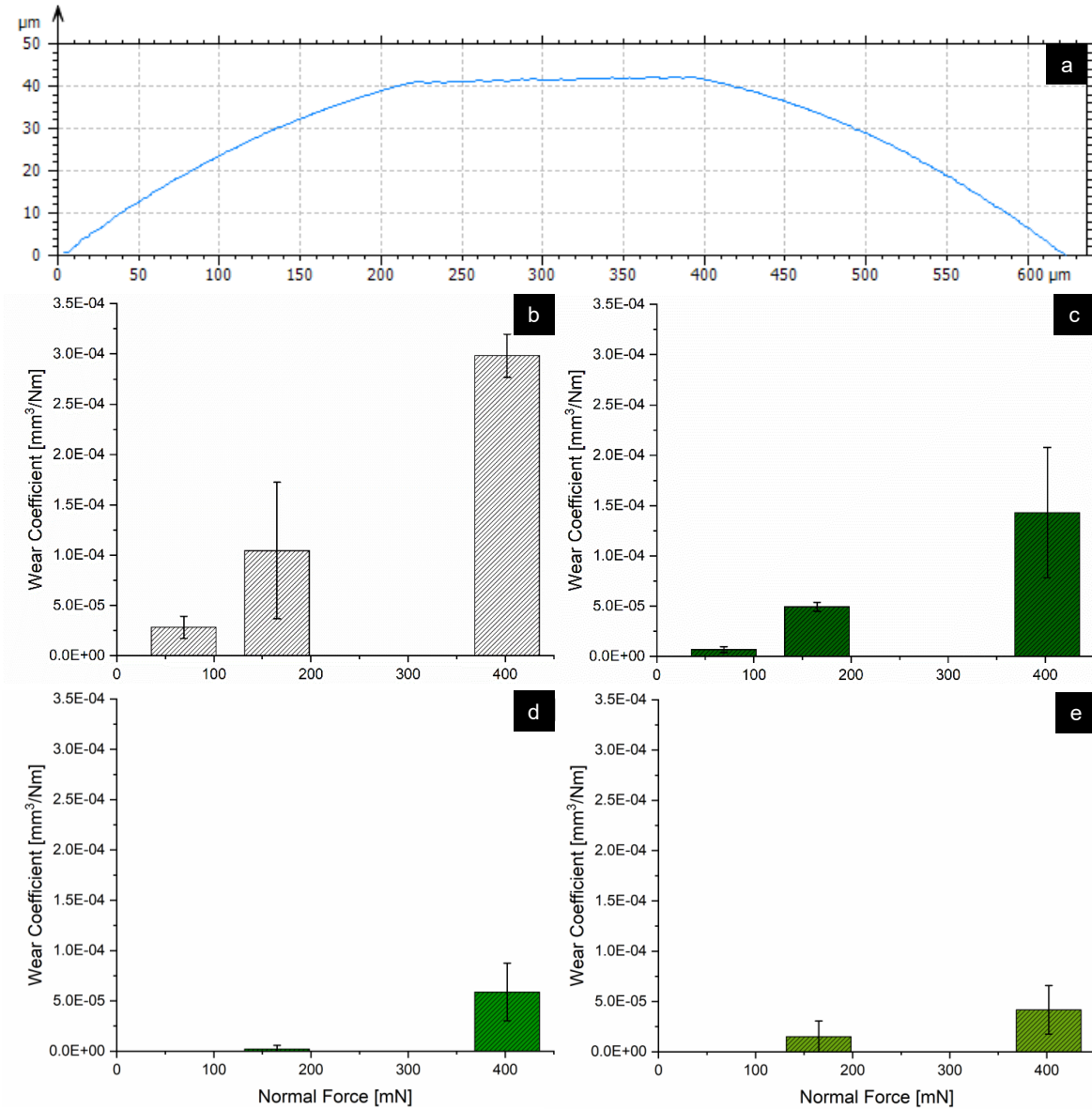
Figure 4.12: (a) Profile of a steel sphere after an experiment at 402 mN and 3.5 µm thickness. (b-e) Normalized wear coefficient of the counterbody over normal force for all tested thicknesses: (b) 0 µm, unlubricated contact, (c) 0.2 µm, (d) 3.5 µm, (e) 6 µm. At 10 µm and 17 µm thickness, no wear was detected at the counterbody. From [79].

a broad and wide wear track. Possible, the low contact pressure might not suffice to compress the graphite layer sufficiently, hence not being large enough to counteract delamination processes.

For the wear volume quantification on the spheres, the samples were cleaned carefully with acetone prior to confocal analysis to remove any transfer layer. For the worn spheres, a clear wear calotte was hence visible as a clear flattening in the side profile

(Figure 4.12a). The average wear coefficient data of the counterbodies is depicted in Figure 4.12. For the counterbodies, an opposing trend of the normal force and coating thickness in comparison to the plate wear coefficient was observed. The normalized wear coefficient of the steel spheres decreased as the coating thickness increased, leading to no wear at all for the two thickest coatings (10 and 17 μm). At larger normal forces, the sphere wear increased linearly.

4.5.4 Microstructure

The confocal images in Figure 4.10 revealed different signs of delamination and abrasive wear. To see whether or not the underlying mirror-like iron substrate underwent microstructural changes, cross sections were cut in the wear tracks and analyzed by SEM. For these investigations, a coating thickness of 3.5 μm and the three different normal forces (69, 165, and 402 mN) were selected. The cross sections were cut perpendicular to the sliding direction at a width of 50 μm to range from the middle of the wear track to the side. By doing so, two compression regions could be analyzed: the graphite-protected region (see Figure 4.13 left side) and contact was made between the steel sphere and the iron plate (see Figure 4.13 right side, inset).

All cross sections revealed the porous graphite structure that has already been discussed in Section 4.3 and the compression of the latter upon counterbody contact, as seen in Figure 4.6. The subjacent mirror-like iron consisted of large iron grains if no shear stress was applied. After sliding at 69 mN, a thin superficial layer at a brighter contrast becomes visible in the inset of Figure 4.13a. At 165 mN (Figure 4.13b) this brighter, nanometer-thin layer became more distinct, and slight grain refinement is evident. At higher forces of 402 mN, this influenced area became wider and deeper, hence plastic deformation of iron occurred up to a depth of 3 μm. At this high load, the surface roughness has increased as well (inset of Figure 4.13c).

4.5.5 Discussion

Friction

Overall, by coating the bare iron plate with graphite, friction could be drastically decreased by up to five times. The measured CoF for the bare steel-iron contact ranged between 0.59-0.68, which is in good agreement with values reported for other dry metal-metal contacts [80]. All CoF trends exhibited a short running-in in the first few cycles, followed by an intermediate stable phase, and at some point an abrupt increase in friction. Reinert et al. argued, that this initial running-in originates from an increase in the contact area due to mild wear of substrate roughness asperities in the beginning. The high fluctuations of the CoF after the rise in friction most likely originates from the continuous formation and destruction of abrasive wear particles, as well as the adhesion of counterbody material to the substrate [81, 82].
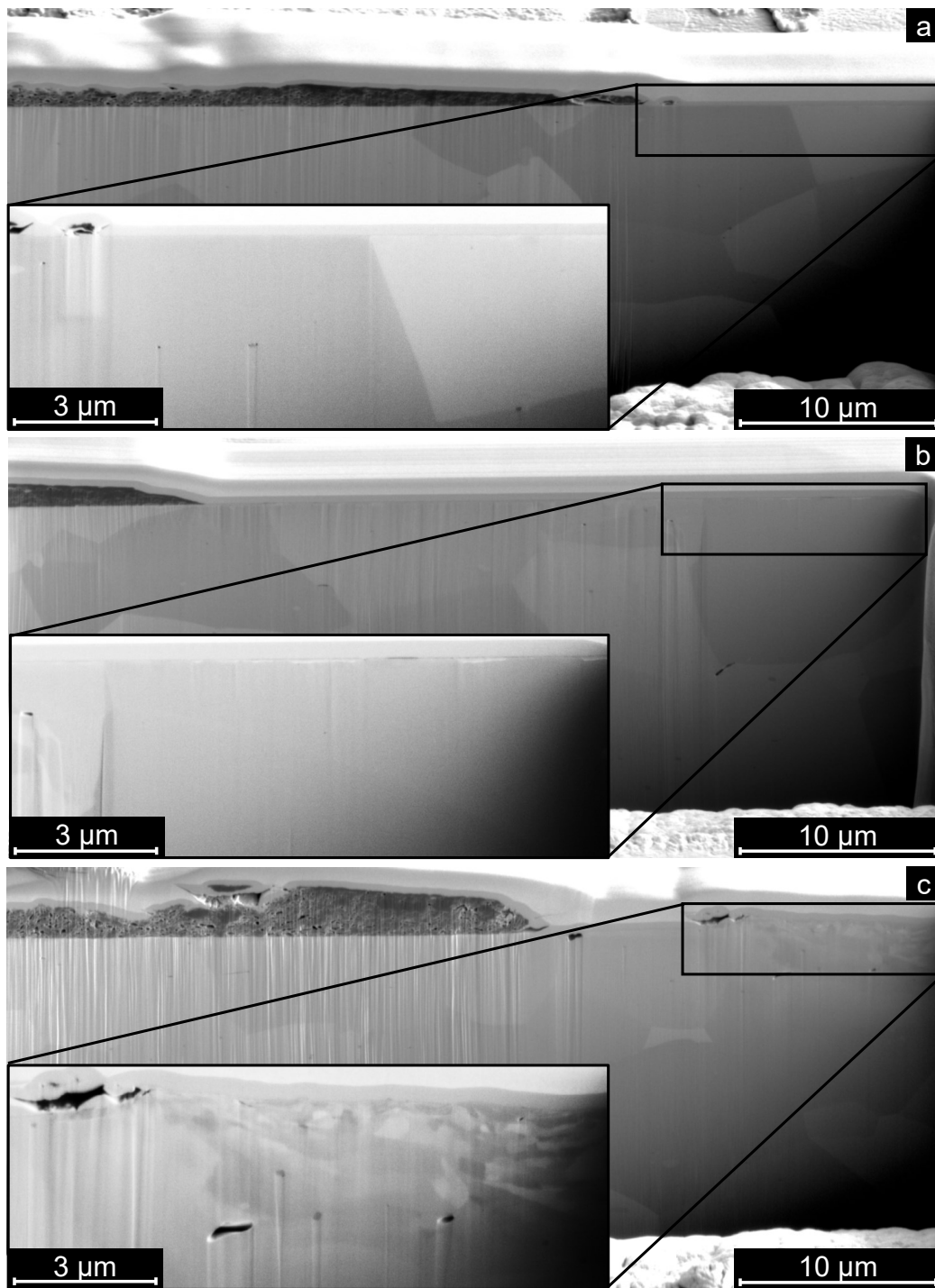
Figure 4.13: Scanning electron microscopy images of cross sections cut perpendicular to the sliding direction in the middle of the wear track after microtribometer experiments at $3.5\,\mu m$ thickness and (a) $69\,mN$, (b) $165\,mN$, and (c) $402\,mN$. From [79].

In this thesis, the highest friction reduction was observed with the thinnest coating of 0.2 µm thickness for all tested normal forces. This is in contrast to previous research dealing with the film thickness dependence of friction, where minimal friction was found at intermediate film thicknesses [51–53, 83–85]. This behavior was explained with a more elastic behavior of very thin coatings, hence an increased surface area is present. The most plausible explanation for the distinct worse performance of intermediate or thick coatings in this thesis is plowing effects [9, 53, 86, 87]. As layer thickness increases, the plowed area increases as well. This will lead to a larger contact area, a higher resistance, and hence higher frictional force. Bowden, Moore, and Tabor proposed a way to quantify the plowing force component of the overall increased frictional force via the wear track width [87]. However, it is difficult to apply these calculations to the soft graphite coating presented in this work, as the coating first gets compressed upon the first mechanical contact. In addition, the overall high roughness of the graphite solid lubricants masks a potential lateral bulging of the graphite coating, which makes a quantitative measurement of the wear track width difficult.

A possibility to reduce the high friction due to plowing effects is a normal force increase, as seen in Figure 4.8. The overall lowest CoF of 0.12 was achieved with a minimal coating thickness of 0.2 µm paired with the highest normal force of 402 mN, hence a Hertzian pressure of 1 GPa. This value is considerably lower than in other recent works on macroscale graphite [6] and graphene [54, 57] lubrication. In conclusion, tuning the graphite coating thickness and normal force led to a remarkable friction reduction. Despite the simple deposition method and the high surface roughness of the soft graphite coating, an excellent solid lubricant was obtained.

The observed friction decrease due to a pressure increase is in line with the theory of Bowden and Tabor, see Equation 2.1: In the case of solid lubricants, a CoF decrease is observed with increasing load as the real surface area A_r increases only slightly. Some groups reported a deviation of this behavior at lower pressures of several kilo or MPa, where friction increased at higher normal forces [6, 88]. However, for the high pressure investigated in this work, the trend is coherent with literature.

Lifetime and Wear

For the uncoated reference sample (black line in Figure 4.8a) a rise in friction occurred almost immediately in the microtribometer experiments. At the normal forces investigated in this study, the surface layer of iron oxide and adsorbates seems to wear away in the first cycles.

This short longevity could be improved by coating the iron with the commercially available graphite suspension with an airbrush spray gun. However, the lifetime of the graphite-coated plates was still limited, which is in line with previous investigations on the durability of carbon-based lubricants. If subjected to large normal forces and thus large shear forces, they have been reported to crack [41, 44, 46, 47]. In our work, an increase in the lifetime can be achieved by increasing the coating thickness. This

improvement can be explained as the coating separates both tribological partners, but this separation is limited by the lubricant layer wear. If no lubricant remains in the friction interface, the friction regime changes to boundary lubrication and wear takes place. However, a shorter lifetime is evident at higher normal forces, see Figure 4.9d) [79]. As reported in the literature, this vast removal of solid lubricants due to high wear occurs as soon as a certain critical load is overcome [41, 44, 46, 47]. Exceptions from this general trend are presumable due to local variations in the coating thickness, hence increasing the standard error of the mean for these deviations as well (e.g. for 7 µm a shorter lifetime was observed at 165 and 402 mN than for the 3.5 µm counterpart, see Figure 4.9b and c).

This high wear became evident in the confocal microscopy analyses as well (see Figure 4.10). Wear first occurs as a portion of the graphite material gets transferred onto the counterbody, hence leading to a graphite-graphite frictional interface for the majority of the experiment. This effect of swift graphite transfer has been reported by e.g. Merkle and Marks for single asperity contacts between graphite and a tungsten tip [35]. The majority of the solid lubricant, however, gets pushed to the reversal points and the sides of the wear track, hence limiting the prevailing lubricant in the contact. This material transport explains the decreased longevity at higher normal forces, as rupture of the coating and delamination takes place and abrasive and adhesive wear sets in, leaving a large wear scar. One possibility to limit this material transport could lie in a substrate roughness increase, hence improving the coating adhesion due to a larger contact area [50], lowering the contact pressure, and thereby leading to less wear. This hypothesis is tested and discussed in the next chapter.

The wear coefficient data presented in Figure 4.11 seems to show a contradictory trend. The confocal images showed increased coating wear at higher normal force, however, the Archard coefficient decreases at the same time. The increase of the normal force decreases the lifetime of the coating as the solid lubricant gets removed faster. However, the total wear volume seems to remain quite independent of the normal force after 500 cycles, as the wear track length and width remained comparable. The wear coefficient, nevertheless, is calculated by dividing the wear volume by the normal force and distance. As the distance remains the same for all experiments, the normal force factors into the resulting wear coefficient more, thus the wear coefficient decreases at higher forces, although the wear volume remains in a similar range. Consequently, for solid lubrication experiments with variations in either the normal force or distance, an analysis of the wear volume might be more significant. If other measurement parameters are tailored, however, the Archard coefficient is helpful for a comparison to other literature studies, as the coefficient is commonly used.

At a given normal force, the wear coefficient and wear volume of the graphite-coated plate increased as the applied coating grew in thickness. This is presumably due to the weak adhesion of the solid lubricant on the mirror-like substrate. For all the experiments, the majority of the coating was pushed to the reversal points without contributing to lubrication. Hence, the thicker the coating. the more material gets

transported and worn away. This adhesion-controlled wear stresses once again the importance of increasing the lubricant-substrate adhesion to ensure long lubrication.

The sphere wear coefficient was quantified as well, and a clear increase was reported in Figure 4.12 while increasing the normal force. Sphere wear only took place if no lubricant remained in the wear track anymore. Hence, this observation is in line with the previous observations: at higher forces, the coating gets worn away quicker, thereby reaching the end of the lifetime sooner and wear of the sphere set in. This negative effect was counteracted by increasing the layer thickness.

Microstructure

The SEM analyses in Figure 4.13 on mirror-like substrates showed a clear trend: with increasing normal force and hence Hertzian pressure, the area and depth of microstructural changes in the sliding contact increased. At 3.5 µm thickness and a force of 69 mN the coating seemed to protect the substrate from any wear. Upon shearing at 402 mN, the short longevity of the coating led to cold welding between both tribo-bodies, hence plastic deformation, grain refinement, and abrasive wear occurred. This cold welding explains the increased substrate roughness after the experiment observed under the SEM in Figure 4.13c as well.

Taking into consideration all the results presented in the previous paragraphs regarding friction, wear, lifetime, and microstructural changes, it seems like the highest coating thickness would be the best choice for high-load applications. However, the friction data demonstrated that a thicker coating in turn leads to higher friction due to plowing. Thereby, two coating thicknesses were chosen for further studies to ensure an optimized trade-off between a long lifetime and low friction: 0.2 and 3.5 µm. Any following analyses described in this thesis were conducted under a high normal force of 402 mN (Hertzian pressure of 1 GPa unless noted otherwise. This normal force was selected to investigate the limits of graphite lubrication under high pressure and to be comparable to the real-life rolling bearing where pressures ranging from 1 to 2 GPa prevail.

4.6 Variation of the Substrate Roughness

The previously discussed microtribometer experiments and surface analyses uncovered the main disadvantage of the graphite coating: its adhesion to the mirror-like iron substrate or the lack thereof. One possibility to increase the adhesion could be a surface roughness increase, which is thus tested and discussed in this section. For this substrate roughness test, iron plates with a seven-fold increased arithmetic mean roughness S_a were prepared and tested at a normal force of 402 mN for three samples - an unlubricated reference sample, and graphite-coated plates exhibiting 0.2 µm and 3.5 µm thickness. The rougher substrate exhibited an S_a of (70 ± 4) nm in comparison to $S_a = (11 \pm 2)$ nm for the mirror-like substrate and is thus comparable to industrial

surfaces such as rolling bearings. The results presented and discussed in this chapter 4.6 were previously published [79].

4.6.1 Confocal Microscopy
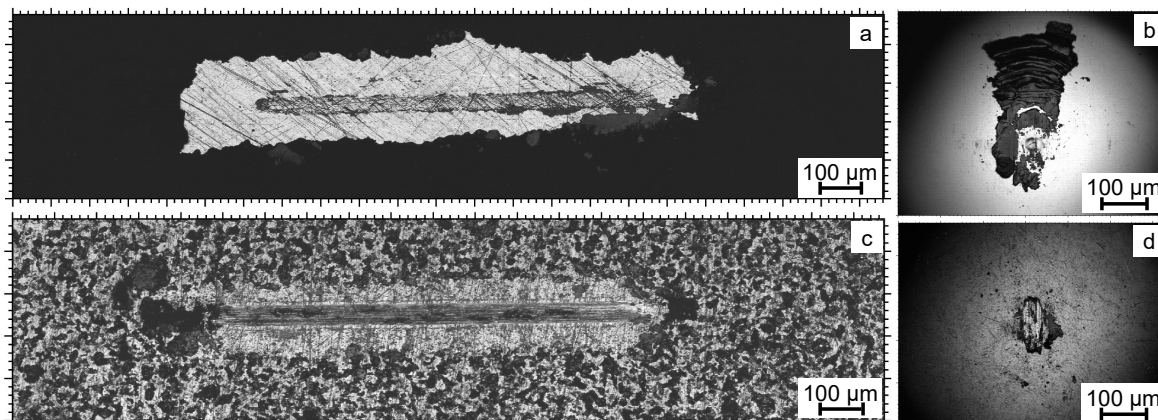
Figure 4.14: Confocal microscopy images of graphite-coated iron plates (left panels) and their respective steel counterbodies (right panels) after the experiments at 402 mN on rougher iron substrates. (a,b) 3.5 µm coating thickness. (c,d) 0.2 µm coating thickness. From [79].

Figure 4.14 displays confocal microscopy images taken after the experiments conducted on rougher substrates with the two coating thicknesses: 0.2 and 3.5 µm. Material transfer and material transport were not changed in comparison to the mirror-like (ML) counterpart: a counterbody transfer layer was formed and the majority of the coating material got pushed to the reversal points of the wear track. When comparing the wear track shape of the 3.5 µm sample (see Figure 4.14a) with the ML experiment (Figure 4.10c) it seems like a larger portion of the graphite coating got piled up at the sides in an accordion-like fashion. The same was observed for the material transfer on the counterbody.

However, a thin and seemingly durable carbon layer remained in the middle of the wear track and no abrasive wear took place, as observed in the mirror-like sample. With the thinner coating of 0.2 µm thickness, this thin carbon layer got worn away during the 500 cycles, and hence cold welding and abrasive wear set in. This thin carbon layer in the middle of the wear track presumably gets formed as graphite particles get trapped in the polishing grooves.

4.6.2 Tribological Performance

Summarized in Figure 4.15 is the tribological behavior of the graphite coating applied on the rougher substrates (red marks or dotted pattern) compared to the mirror-like
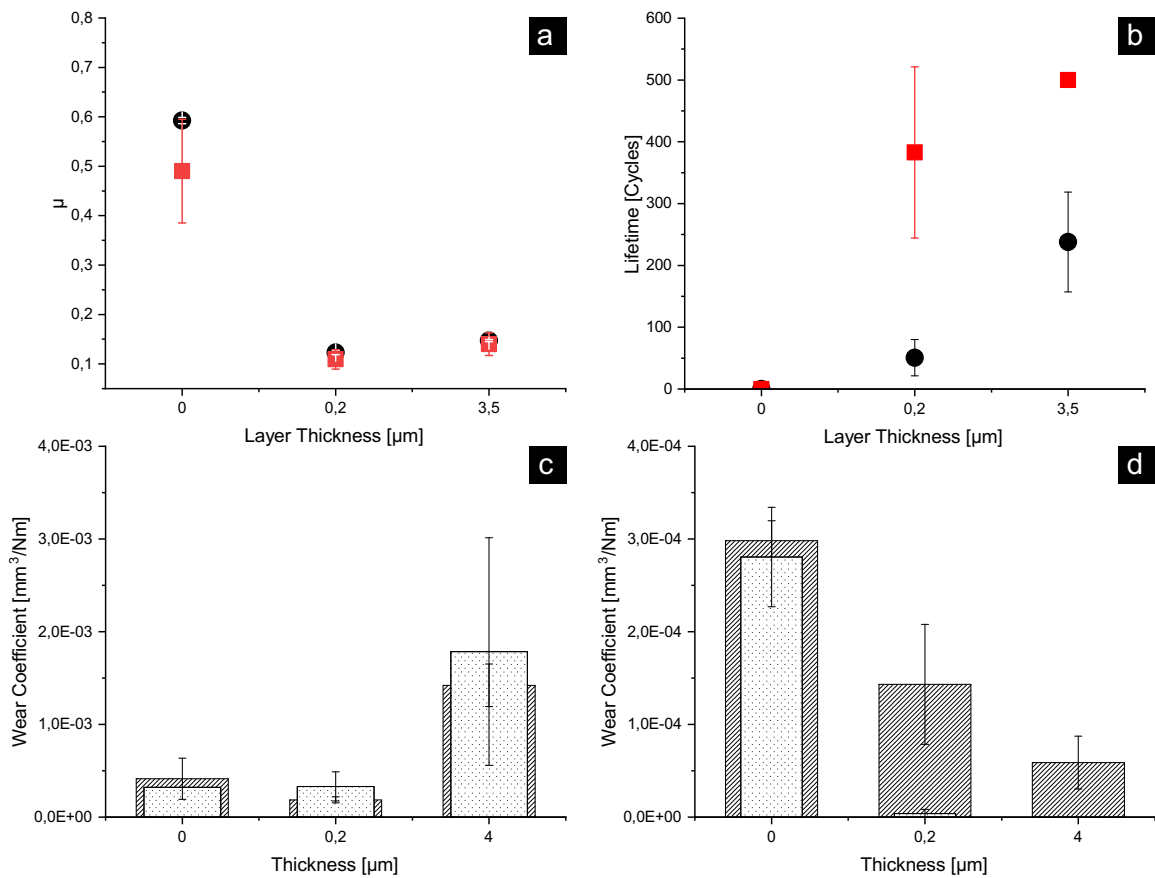
Figure 4.15: Tribological performance of rougher substrate compared to mirror-like substrate plotted over the tested layer thicknesses. (a) Coefficient of friction, black = mirror-like, red = rougher, (b) Lifetime of the coating, (c) wear coefficient of the graphite layer, lines = mirror-like, dotted = rougher, (d) wear coefficient of the counterbody. From [79].

samples (black marks or line pattern). The calculated average friction coefficient was consistently lower on the rougher substrates, which might be due to the observed thin carbon layer in the contact. Remarkable is the drastically increased longevity (Figure 4.15b), up to 7.6-fold for the 0.2 µm coating and 2.1-fold for 3.5 µm thick coating.

The wear coefficient of the plate and coating (see Figure 4.15c) was slightly increased for the rougher substrate and the overall trend was the same as for the mirror-like substrate: increasing wear was measured for larger coating thickness. The wear increase in comparison to the ML substrate is contradictory to the hypothesis postulated in the previous chapter – the substrate-coating adhesion was expected to increase with a rougher plate and thus the wear coefficient should decrease. The counterbody wear, however, was positively impacted with a rougher substrate with a wear coefficient of $3.7 \cdot 10^{-6}$ mm³/Nm at 0.2 µm, and no detectable wear with 3.5 µm coating thickness.

To gain a more detailed understanding of the formed thin carbon layer and its struc-

ture, cross sections were cut with FIB perpendicular to the sliding direction to cover the whole track width and analyzed with SEM (Figure 4.16a) and BF-TEM (Figure 4.16b). The underlying iron substrate shows signs of plastic deformation and grain refinement in the upper 1.5 μm that are most likely already created in the polishing process. A comparison with the cross-section cut after indentation at 69 mN (displayed in Figure 4.6b) confirms this hypothesis, as the indentation experiments were conducted on the rougher substrates and the same microstructure is revealed.

The thin carbon layer exhibits a compact structure with no pores. The thickness ranges from 30-150 nm as seen at the TEM lamella (Figure 4.16b). As hypothesized in previous sections, the graphite material seems to have gotten trapped in the polishing trenches, visible from the side view cross section in Figure 4.16a. A more detailed discussion of the thin carbon layer structure will be discussed in Section 4.8.3.

4.6.3 Thin Carbon Layer Built-up

How does the graphite coating thickness influence this thin carbon layer formation on rougher substrates? The thinner coating with 0.2 μm thickness exhibited a heterogeneous coverage by graphite flakes (presented in Figure 4.14c). In the wear track next to abrasive wear scars, the thin carbon layer is still visible, therefore, this little material is sufficient to form the layer. For a better understanding of the carbon layer formation, an additional set of microtribometer experiments was conducted. With the thin coating of 0.2 μm thickness, the microtribometer sliding experiment was stopped after varying experimental duration: 10, 100, 200, and 400 cycles.

Displayed in Figure 4.17 are SEM images of the thin carbon layer built-up during the experiment. As visible in Figure 4.17a, a thin carbon layer already formed during the initial 10 cycles with a single graphite flake lying on top of it (left side of the image). After 100 cycles the layer has grown in width which then stagnated for longer experiments. After an average duration of 382 cycles, the thin carbon layer has worn away, thereby leading to cold welding and abrasive wear of the two contacting surfaces.

4.6.4 Discussion

The goal of the previous section was to analyze whether the adhesion of coating and substrate could be improved by mere substrate roughness increment. As the confocal images in Figure 4.14 have shown, the graphite was pushed to the reversal sides in an accordion-like matter, leading to an even higher wear coefficient. Nonetheless, the measured tribological performance was still considerably increased in terms of friction reduction and lifetime improvement.

The reason for this observation is the formation of a thin carbon layer, which remains in the middle of the wear track. It formed as the graphite flakes got trapped in the polishing trenches and additional material got stuck alongside it. The SEM images

Figure 4.16: Images of cross sections cut perpendicular to the sliding direction in the middle of the wear track after microtribometer experiments at $3.5\,\mu m$ thickness and $402\,mN$ yielded by (a) SEM and (b) bright field TEM. From [79].

in Figure 4.17 have shown that the carbon layer is not only formed from graphite material already present in the contact line, but also from flakes transported from the sides. The layer seems to be sufficiently thick to cover the surface asperities of both tribopartners and hence separate them for a longer period of time in comparison to the ML substrate. In addition, the soft layer will lead to a larger contact area of the contacting surfaces and thus a smaller local contact pressure. The formation of this thin layer with the $0.2\,\mu m$ thin graphite coating is especially noteworthy, as it demonstrates the fact, that the initial coating does not need to homogeneously and completely cover the substrate surface for the layer formation.

The investigated increased roughness of $S_a = (70 \pm 1)\,nm$ is not only performing
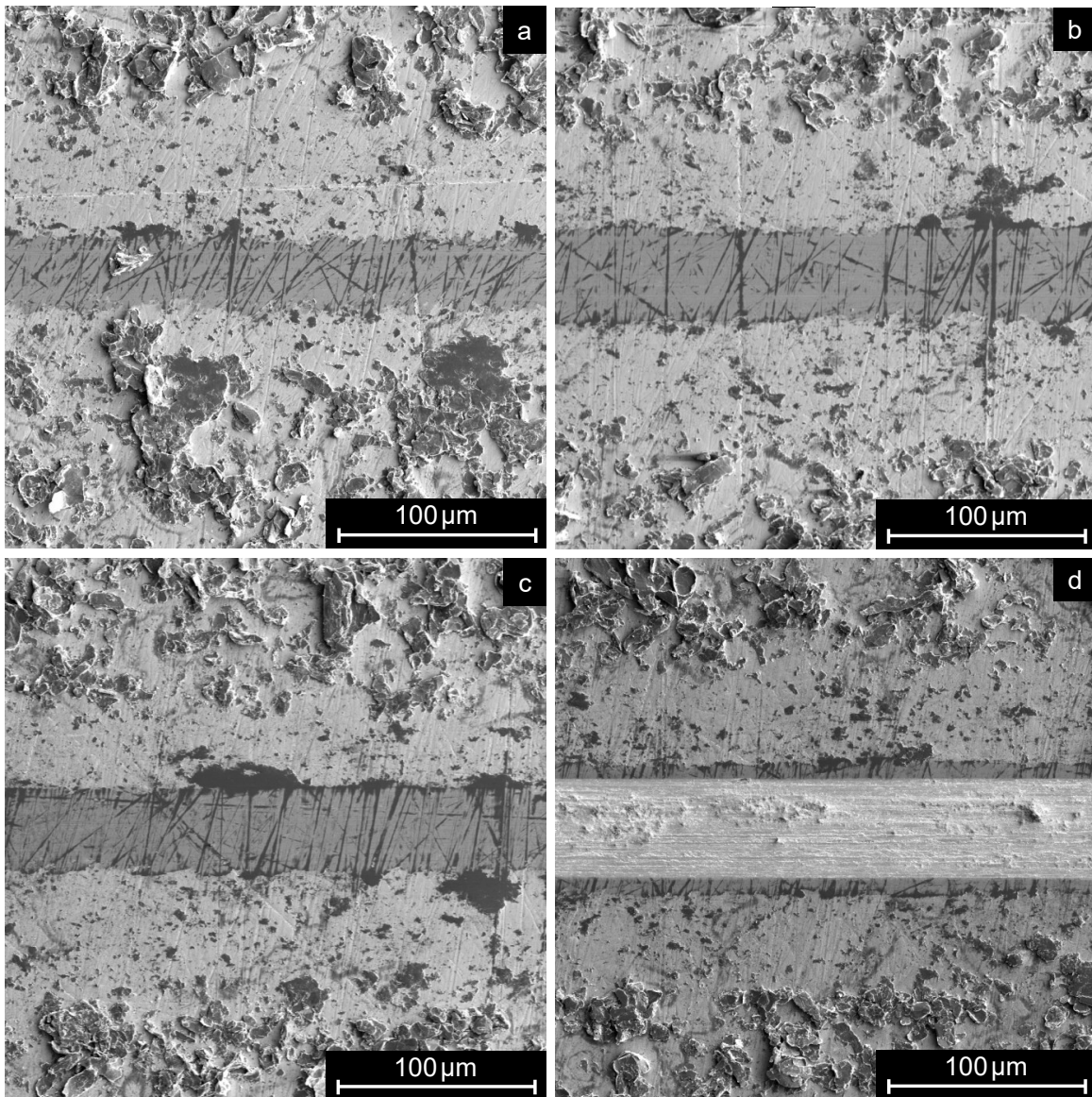
Figure 4.17: Scanning electron microscopy secondary electron (SE) images in the middle of the wear track after microtribometer sliding experiments vs. a 100Cr6 sphere for a 0.2 µm thick graphite film and after (a) 10 cycles, (b) 100 cycles, (c) 200 cycles, and (d) 500 cycles. From [79].

better in the tribological experiments than its mirror-like counterpart, but it is also considerably more comparable to industrial parts like rolling bearings. The reported friction decrease with roughness increase contradicts the findings of Reinert et al. [61], who found a friction increase at higher roughness values. However, this contradiction can be explained by a difference in the velocity accommodation (shearing instead of rolling).

4.7 Variation of the Substrate Roughness at larger Scale

The comparison between a ML and a rougher substrate only gives a vague understanding of the substrate roughness influence on friction and wear. Do friction and wear decrease linearly with roughness increase or is there an optimal value? How do the total roughness, roughness valleys, and roughness peaks factor into the tribological performance of graphite coatings? To elucidate these research questions, a parameter study with more variations of the different surface roughness parameters was conducted. For this study, the polishing process was adapted with SiC papers of differing grain sizes (see Section 3.3.1). The samples were tested in the same experimental setup as the previous analyses, with a normal force of $402\,\mathrm{mN}$ over a width of $1\,\mathrm{mm}$, a speed of $0.5\,\mathrm{mm\,s^{-1}}$, and under an atmosphere of dry, pressurized air (RH $\leq 5\%$).

4.7.1 Roughness Determination

To determine the areal roughness parameters S_k, S_{pk}, S_{vk}, and S_a, the different substrates were analyzed after polishing by confocal microscopy, and the images then processed with the *Vision 64* software from Bruker Corporation. During these measurements, the guidelines of the DIN ISO 25178-2 were followed accordingly [89]. The image was corrected with an F-operator, outliers were excluded by respective masking of the histogram, and the image was filtered with a robust, second-order Gaussian regression filter. This Gaussian filter is applicable for plateau surfaces and excludes edge and filter artifacts. Afterwards, the areal Abbott-parameters S_k, S_{pk}, S_{vk}, and S_a were calculated. The parameters represent the core height roughness, reduced peak height, reduced valley height, and arithmetic mean roughness, respectively [89].

4.7.2 Surface Roughness

Figure 4.18 displays confocal grey scale images of the iron plates after the different polishing procedures. As visible, the amount and optical depth of the grooves decreased if the grain size of the final SiC polishing step was decreased (P320 to P4000). For the smoothest sample (mirror-like, Figure 4.18f), two diamond suspensions on polishing cloths were used for the last polishing step, which eradicated the last remaining grooves in the surface. This qualitative decrease in roughness could be quantified as well by evaluating the areal roughness parameters (see Table 4.2) – a clear decrease of all roughness parameters is observed. For an analysis of the influence of peaks and valleys on friction and wear in later experiments, the ratio between S_{pk} and S_{vk} can be calculated. The yielded values are 1.20, 1.08, 0.80, 0.88, 0.65, and 1.00 for the P320 surface to ML. Hence, the P1200 sample and all samples with lower roughness exhibit more valleys than peaks from the polishing process.
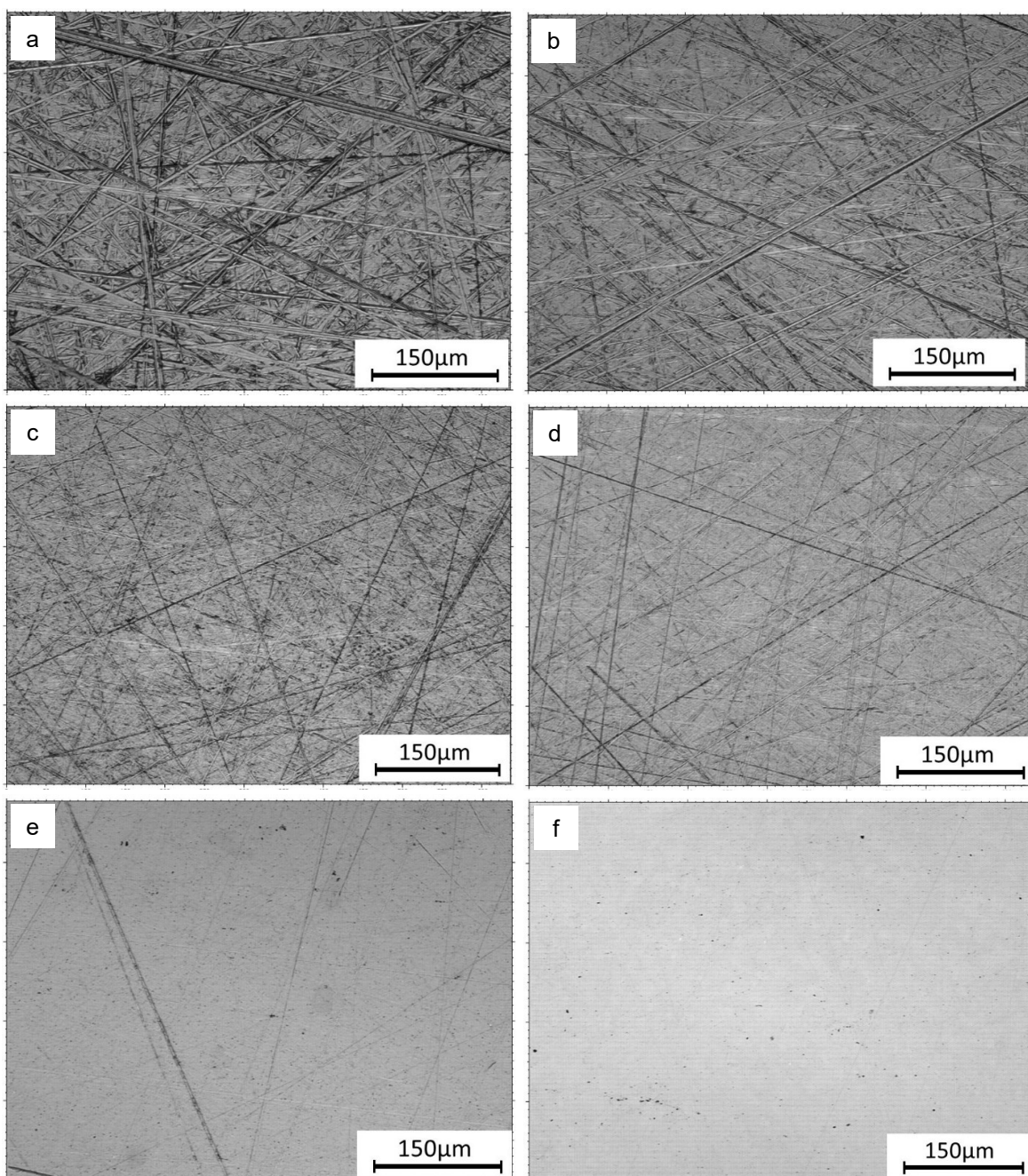
Figure 4.18: Confocal images of the iron plates after polishing up to different SiC grain sizes. (a) P320, (b) P600, (c) P1200, (d) P2500, (e) P4000, (f) mirror-like.

Table 4.2: Thickness and roughness parameters for samples produced on a mirror-like (ML) substrate.

End SiC grit Size	S_k [nm]	S_{pk} [nm]	S_{vk} [nm]	S_a [nm]
P320	433 ± 16	312 ± 13	261 ± 8	153 ± 4
P600	268 ± 8	183 ± 7	169 ± 5	94 ± 3
P1200	207 ± 2	107 ± 2	133 ± 7	70 ± 1
P2500	143 ± 3	78 ± 4	89 ± 6	48 ± 1
P4000	61 ± 4	49 ± 7	75 ± 9	24 ± 2
ML	38 ± 3	14 ± 1	14 ± 1	12 ± 1

4.7.3 Friction and Lifetime

For every roughness state, microtribometer experiments with at least three repetitions were conducted. A summary of the microtribometer experiments for each roughness state is attached in the Appendix (Figure A.2-Figure A.6). In general, for some of the experiments, the CoF remained stable during all 500 cycles, but for some of them, an abrupt increase in friction was observed. As previously discussed, this is due to starvation of the graphite solid lubricant caused by extensive material transport. Hence, the friction behavior was quite similar to the previous experiments on the substrate roughness influence, see Section 4.6.2.
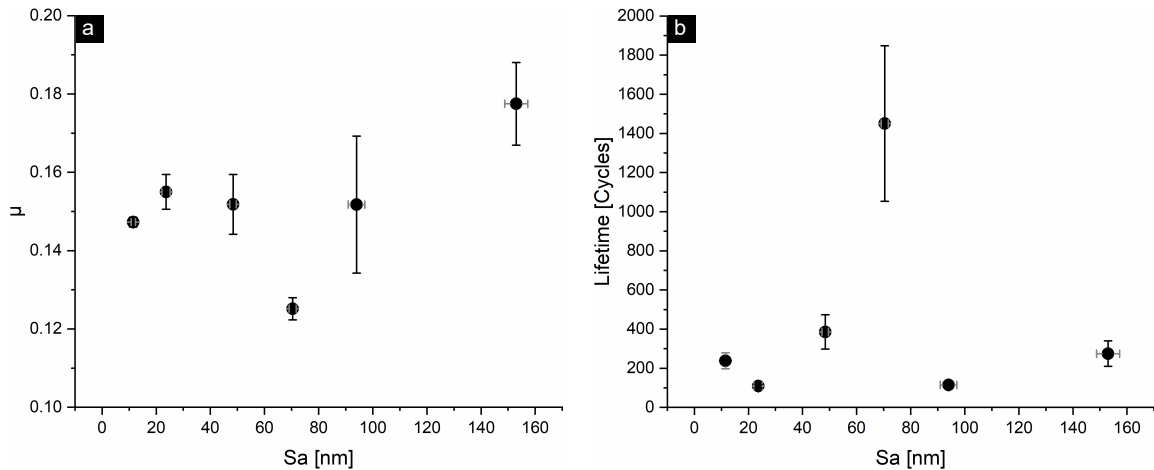
Figure 4.19: Steady-state CoF (a) and lifetime (b) in dependence of the different roughness states.

Figure 4.19 displays the summarized steady-state CoF values versus the gathered arithmetic mean roughness S_a. A slight friction increase at higher roughness values is visible, with one exception at $S_a = 70$ nm that corresponds to the P1200 sample. This roughness state corresponds to the roughness state already investigated in the previous section, ascribed as the "rougher" substrate. This roughness seems to provide the best tribological performance among the tested samples, both in terms of friction reduction

and longevity improvement (depicted in Figure 4.19b). In the lifetime experiments, two sets of experiments were conducted. In the first one, the experiment was stopped after 500 cycles. Some microtribometer experiments on different roughness states exhibited a lifetime close to these 500 cycles. For these roughness states (P1200 and P2500), an additional set of experiments with longer duration was conducted to investigate their lubrication limits. Overall, the lowest CoF of $\mu = 0.13$ and the longest lifetime at (1451 ± 398) cycles were achieved with the P1200 sample. A full list of the CoF and lifetime obtained with coatings on substrates with varying roughness states can be found in the Appendix in Table A.1. Although the results displayed here include only a comparison with the arithmetic mean roughness S_{a}, the same trends were observed for all of the investigated surface roughness parameters.

4.7.4 Wear
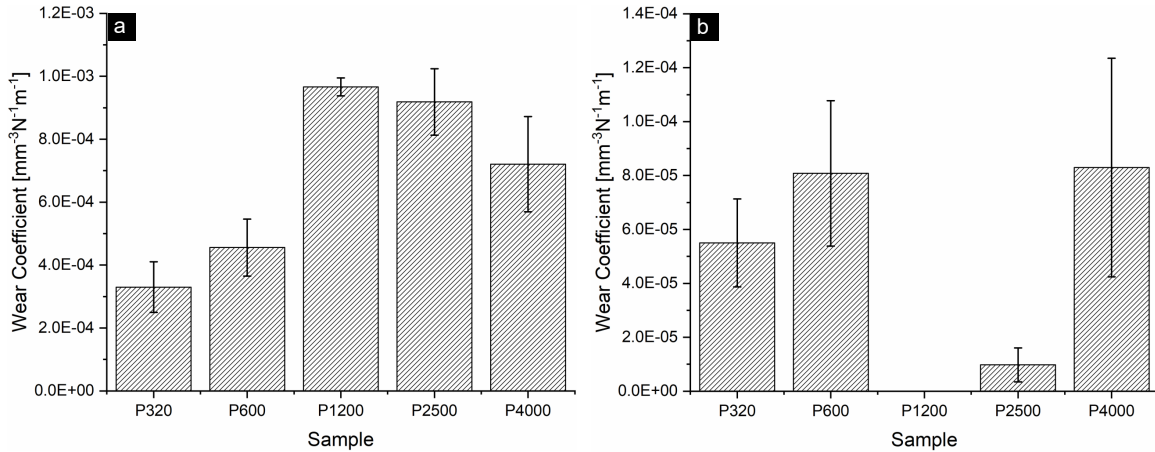
Figure 4.20: Normalized wear coefficient of the plate (a) and sphere (b) in dependence of the different roughness states.

To investigate the wear behavior and how it is influenced by the substrate roughness, the wear coefficient of both tribo-bodies was calculated and summarized in Figure 4.20. The graphite coating and iron plate wear (Figure 4.20a) both display a parabolic shape in terms of their roughness dependence. The highest wear coefficient of the graphite-coated plate was measured at the P1200 sample, which resulted in the lowest CoF and longest longevity; for both higher and lower roughness, less wear was measured. The counterbody wear coefficient (Figure 4.20b) yielded an opposing trend, as all steel spheres remained completely intact during the P1200 experiments. With other roughness states, higher wear was reported as well as a large scattering of the results. Thus, no clear correlation between counterbody wear and substrate roughness was visible.

To gain a deeper understanding of the wear behavior in dependence of the substrate roughness, additional microtribometer experiments with a shorter duration of 30 cycles
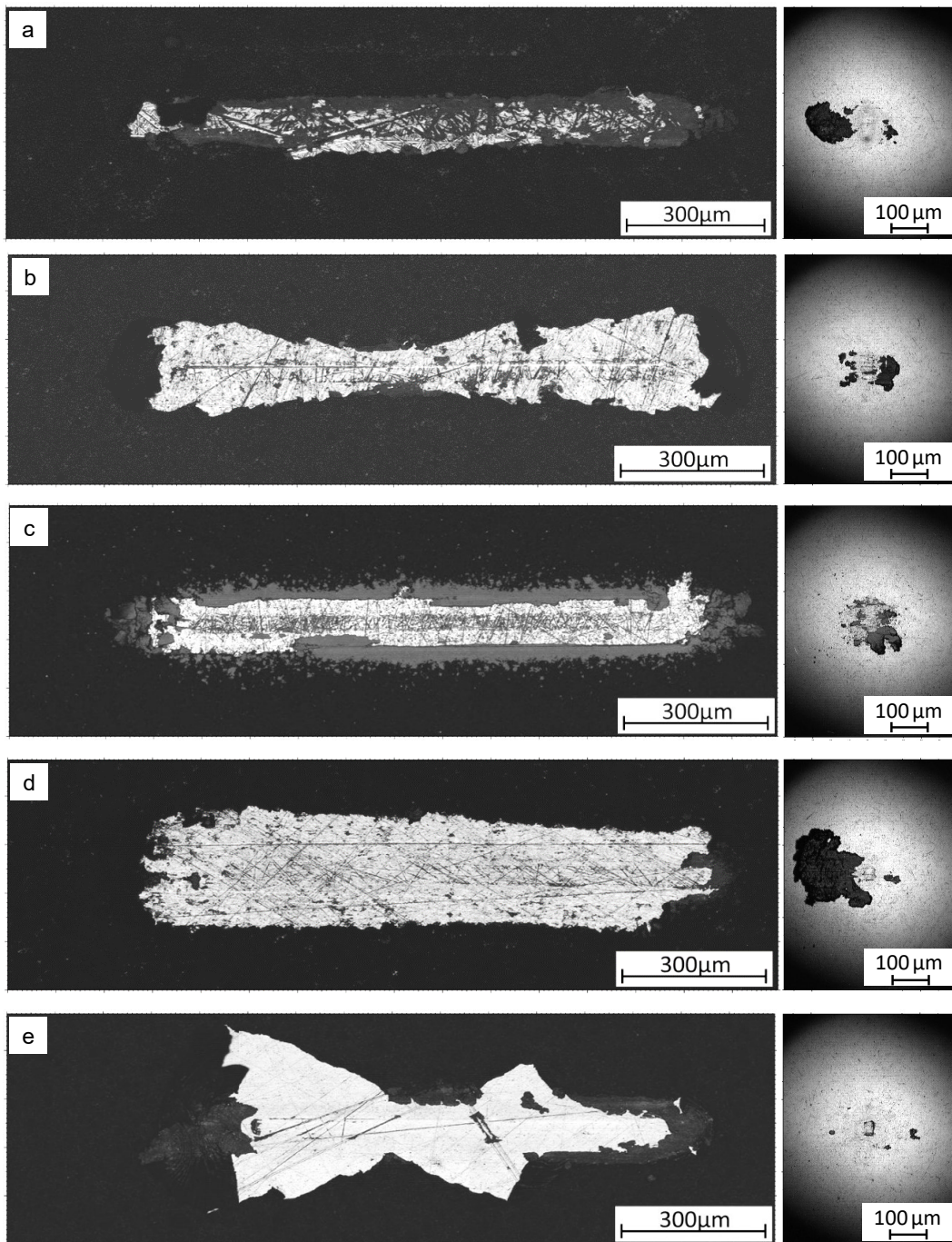
Figure 4.21: Confocal images of both tribo-bodies after 30 cycles under 1 GPa on varying substrate roughness states. (a) P320, (b) P600, (c) P1200, (d) P2500, (e) P4000. The waviness and fractal composition of rough surfaces were omitted for a clearer image.

were conducted for all roughness states. The results are depicted in Figure 4.21. This study should also reveal whether the crucial thin carbon layer forms independently of the substrate roughness or whether it depends on certain surface artefacts or struc-

tures.

For all samples, a material transfer of graphite onto the counterbody is evident, as well as material transport to the reversal points at the plate. This observation is in line with the findings discussed in the previous chapter. However, there were clear differences in the wear behavior as a function of the different substrate roughness samples. Although trapping of carbon material in the polishing grooves was observed for all roughness states, the extent of the material differed greatly. For the highest roughness sample, P320 in Figure 4.21a, large patches of graphite material got trapped alongside the sliding contact. Nevertheless, between them, large regions of blank iron are visible with no graphite coverage. For P600, less carbon coverage than for the P320 sample was visible in the wear track. The P1200 sample obtained a consistent and homogeneous coverage of the iron substrate due to the formation of the thin carbon layer. For the lower roughness samples, P2500 and P4000, graphite still got trapped in the polishing trenches but due to the fact that fewer grooves were present on the surface, no thin carbon layer is visible. The experiments with the mirror-like substrate are not displayed in this graph; for them, no trapping of carbon material was observed.

For some of the experiments, in particular with the P4000 sample in Figure 4.21e, delamination of the graphite coating was evident, especially on the sides of the wear track. This delamination hints at a decreased coating-substrate adhesion, presumably due to a lack of roughness peaks and trenches that the coating material could hold onto.

4.7.5 Discussion

Holmberg, Ronkainen, and Matthews emphasized the importance and influence of substrate roughness on lubrication with soft coatings due to variations in the asperity contacts [86]. The results presented in this thesis highlight the extraordinary behavior of the P1200 sample ($S_\mathrm{a} = (70\pm1)\,\mathrm{nm}$). With a lifetime of (1451 ± 398) cycles, a steady-state CoF of $\mu = 0.13$, and no counterbody wear, this roughness state resulted in the best tribological performance. The plate and coating wear coefficient, however, was quite high at $k = 9.66\cdot10^{-4}\,\mathrm{mm^3\,N^{-1}\,m}$. The reason for this good lubrication behavior seems to lie in the thin carbon layer formed in the tribological contact. As stated in Section 4.6.4, the graphite particles get trapped in the polishing trenches where they may act as lubricant reservoirs. However, the formation of this thin carbon layer varied between the different roughness samples. To demonstrate the differences between the samples more clearly, a schematic summarizes them in Figure 4.22.

The arithmetic mean roughness S_a decreased continuously when the SiC paper grain size of the polishing steps was decreased as well, hence P320 exhibited the highest surface roughness S_a. At the same time, the ratio of the core peak roughness S_pk and the core valley roughness S_vk changed for the different samples. Both parameters are critical for a better understanding of the lubrication behavior. S_a represents the
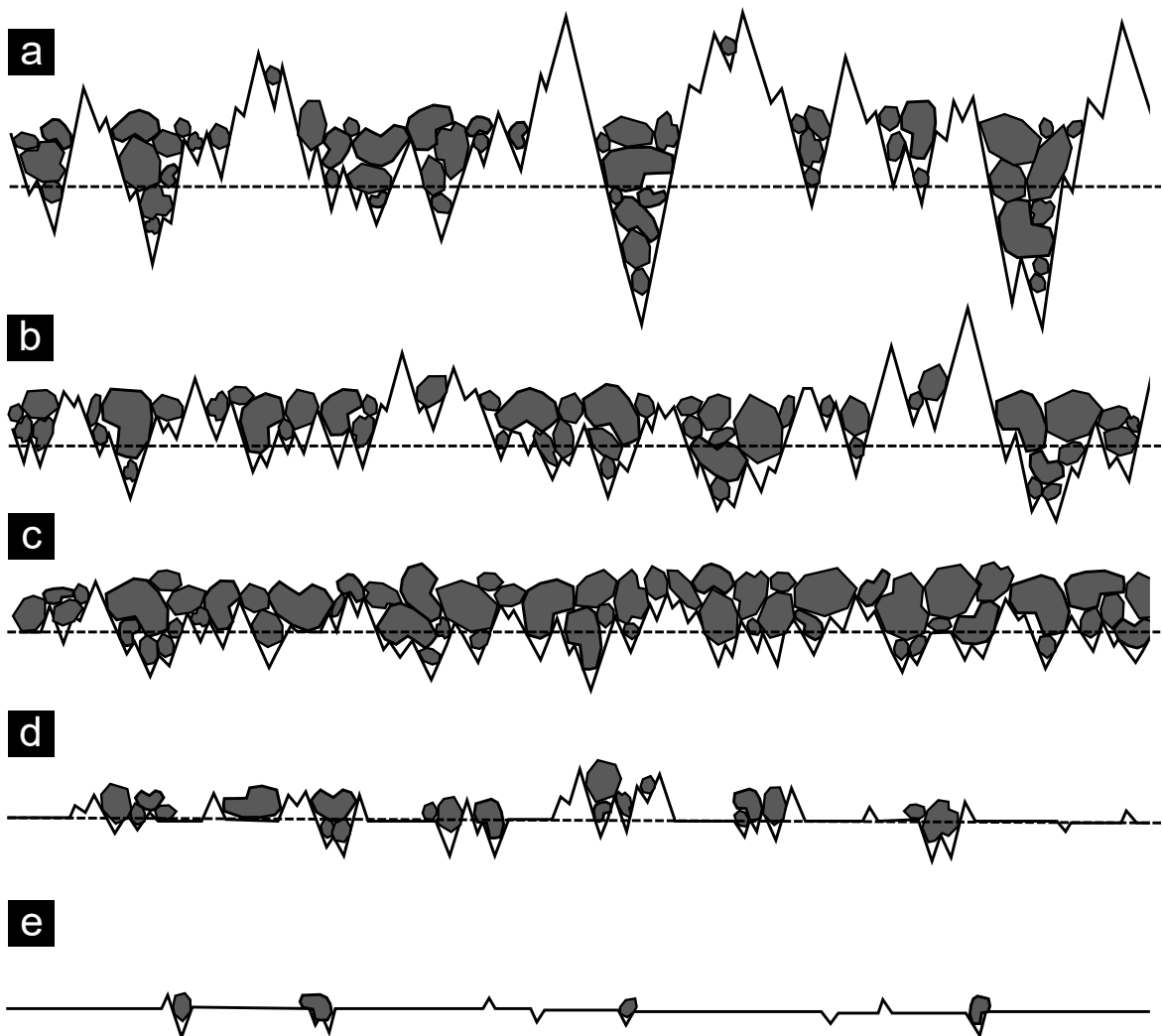
Figure 4.22: Schematic representation of different iron plate surface roughness states and the respective graphite particle entrapment. (a) P320, (b) P600, (c) P1200, (d) P2500, (e) P4000. For a better understanding, the waviness and fractal composition of rough surfaces is omitted and the main focus lies on the core peak height and core valley height.

arithmetic mean surface roughness. A high S_{pk} stands for a surface dominated by high peaks, which will lead to a small initial contact area and thus high contact stress in the first initial cycles. This high contact stress may lead to faster abrasion of the roughness peaks, which could lead to the formation of hard, abrasive wear particles and hence increase wear. S_{vk} is crucial for the lubrication behavior, as valleys can entrap both the solid lubricant and the abrasive wear particles, thus decreasing wear.

For the high roughness samples P320 and P600 (see Figure 4.22a and b), the $S_{\mathrm{pk}}/S_{\mathrm{vk}}$ ratio was larger than 1, hence peaks dominated the surface. The average roughness S_{a} was high as well, thus peaks and valleys will be of increased height or depth, respectively. Due to the overall high roughness, easy entrapment of graphite particles

in the deep polishing trenches of the surface will occur. However, it seems like the peaks determine the tribological performance of the samples - due to the height of the peaks, there will be not enough material to cover the surface asperities. Thus, first mixed and soon boundary lubrication will take place between the iron substrate and the steel counterbody. This insufficient lubrication at high surface roughness values was reported by Hirata, Igarashi, and Kaito as well for carbon onions [90]. Due to the contact between the surface asperities of the steel sphere and iron substrate, the substrate asperities will wear away due to high contact stress, which in conclusion leads to abrasive wear particle formation and a short longevity.

When investigating the P1200 sample (Figure 4.22c), the S_{pk}/S_{vk} ratio drops below 1 – more valleys than peaks prevail and thus they can entrap the graphite material and abrasive particles. Due to the overall decreased roughness S_a, the entrapped material seems to suffice to cover the majority of the substrate asperities. Another factor driving the lubricant entrapment might be an interplay between the size of the graphite flakes and the substrate topography features. Presumably, the P1200 sample provides an ideal surface for the 0.5-1 µm large graphite flakes. This leads to the observed thin carbon layer formation which enables low friction, a long lifetime, and low counterbody wear.

For the smoother samples (P2500 and P4000, see Figure 4.22d and e, respectively), the peak to valley ratio is below one as well. However, it seems like the ratio is not the only surface characteristic that influences the thin layer formation – the abundance of valleys and grooves matters, too. As visible in the confocal images in Figure 4.18d and e, the P2500 and P4000 samples exhibit fewer polishing grooves than P1200. The decreased amount of grooves is represented in an S_a as well. Fewer polishing trenches lead to decreased entrapment of graphite and worse adhesion of the material to the substrate, which explains the observed higher friction and wear compared to the P1200 sample. In summary, the lubrication behavior of graphite and especially the thin carbon layer formation depends strongly on the interplay between the peak to valley ratio – valleys need to dominate the surface –, the substrate topography feature sizes, and the overall roughness to yield the ideal adhesion of graphite to the substrate.

This interplay seems to be ideal for the P1200 sample, which is supported by the confocal images in Figure 4.18c as well. For the majority of the other samples delamination of the graphite coating is visible as the coating got teared away in large portions. For P1200, the wear scar is less wide and a compression of the coating on the wear scar sides is visible as lighter grey areas. Consequently, the coating gets easily compressed into the polishing valleys during the first initial cycles and remains there for a longer period of time. For lower roughness, the valleys are not deep enough to entrap the coating on the sides of the wear track and thus it gets dragged along. For higher roughness, high wear has been observed as well in the confocal images. Here, due to a smaller contact area higher local stress will occur, which might lead to cold welding between the graphite transfer layer on the counterbody and the graphite-coated plate. These newly formed covalent C-C bonds will lead to clustering and again additional material transport on the sides of the wear track. One has to note that this effect,

however, seems to be less pronounced than the additional material transport due to lack of polishing grooves, as seen in the lower wear coefficient for P320 and P600 than P2500 and P4000 (compare Figure 4.20).

There have been multiple studies on the influence of substrate roughness on lubrication that exhibited a beneficial effect of a lower roughness on the tribological performance [61, 81, 90–92]. However, the majority of them dealt with other solid lubricants than graphite or with carbon onions, which exhibit a different lubrication mechanism than graphite. Xiaowei et al. analyzed the roughness of nuclear grade graphite and reported lower friction at higher roughness [93]. In their work, both tribo-bodies consisted of graphite and thus an increased roughness led to the formation of wear debris, which increased lubrication due to their carbon-based nature.

The results presented in this chapter emphasize the importance of an individual analysis of graphite lubrication, as the results may vary greatly depending on the used substrate materials and their roughness. For the polycrystalline graphite investigated in this thesis, the interplay between the overall roughness and the peak-to-valley ratio determines and limits the lifetime and performance of the coating – the best results were achieved with an intermediate roughness and with a peak-to-valley ratio smaller than one.

4.8 Variation of the Humidity

4.8.1 Tribological Performance

The previous chapters have demonstrated that multiple experimental parameters influence friction, wear, and the coating lifetime upon solid lubrication with graphite. As mentioned in the introduction (section 2.3), graphite lubrication depends strongly on the surrounding humidity. However, many publications only compare graphite's behavior in vacuum and under ambient conditions, sometimes without quantifying the humidity. To close this gap and to investigate the humidity influence on graphite friction and wear, a detailed parameter study was conducted over a broad range of relative humidity (RH) values. The results presented and discussed in this chapter 4.8.1 were previously published [28].

As the previous section revealed the best tribological performance with the P1200 sample of intermediate roughness, this roughness state was selected for all substrates of the following microtribometer experiments. The plates were again coated with graphite of an average thickness of 3.5 µm and tested in the microtribometer at a sliding distance of 1 mm and a velocity of 0.5 mm. Both low and high loads were investigated with experiments conducted at 50 MPa and 1 GPa. The relative humidity was varied by humidifying pressurized air with a self-built humidifier (see Section 3.3.1 for schematics). By doing so, the relative humidity was varied between values below 5 % RH (dry compressed air) and 45 % RH. To simulate complete immersion of the
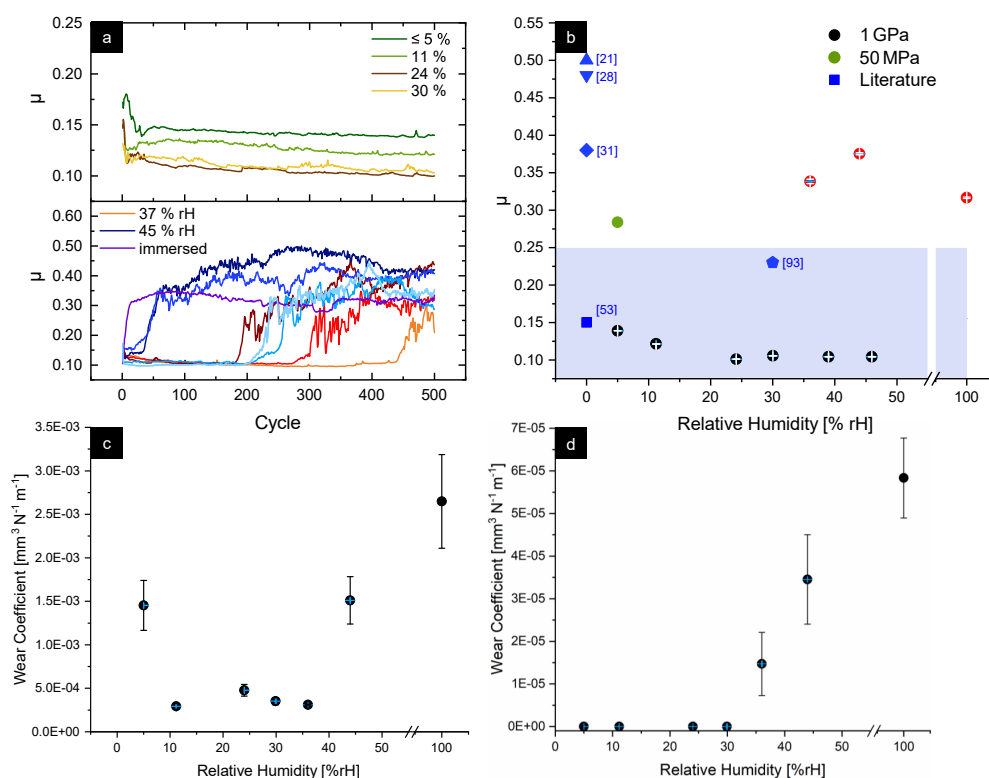
Figure 4.23: Tribometric results of the humidity dependence on graphite lubrication. (a) CoF (μ) over the experimental duration for various humidity values. For the experiments conducted at lower humidity (RH $\leq$ 30%), the average of three consecutive measurements for each humidity is shown in the upper panel. The standard deviation of three measurements is marked as the semi-transparent areas. In the lower panel all measurements at the higher humidity values (37% and 45 % RH) are shown (shades of orange/red: 37 % RH, shades of blue: 45 % RH, purple: contact immersed in deionized water). (b) Average steady-state CoF with standard error of the mean as error bars, and literature values as a comparison [21, 29, 32, 54, 94]. Black circles represent the average of 100 cycles at the end of the experiment for RH $\leq$ 30% or the average of 20 cycles prior to rise in μ for RH $>$ 30%. In the latter case, the steady-state high friction values are plotted in red (average of the last 100 cycles). (c) Normalized wear coefficient of the graphite-coated iron plate after 500 cycles. (d) Normalized wear coefficient of the counterbody after 500 cycles. Adapted from [28].

tribologal contact, another experiment was conducted with a drop of deionized water that was added to the contact. The wear coefficient of the plate and counter body were again determined by confocal microscopy as described in the Material and Methods Section 3.4.1.

Displayed in Figure 4.23a is the CoF evolution for the investigated humidities. A short

running-in period was observed (lasting less than 80 cycles) for all experiments. For experiments conducted under RH ≤ 30%, the CoF remained low and stable, whereas at higher humidity values (37% and 45 % RH) an intermediate low friction period after running-in was observed which ended with a steep rise of the CoF. The duration of this stable low CoF phase is again referred to as the lifetime and corresponds to the cycle number before the CoF exceeds the average of the previous ten cycles by 30%. As evident from the graph, a distinct scatter of the lifetime for the different repetitions could be observed. However, a general trend was visible as the longevity decreased while increasing the humidity (>500 for RH ≤ 30%, 300 for 37 % RH, and 153 cycles for 45 % RH). For the immersed contact (purple), no stable phase was observed.

Figure 4.23b depicts the humidity dependence of the steady-state CoF. Even at high loads of 1 GPa there seemed to be an influence of the surrounding humidity on friction. A first increase in humidity from ≤ 5% to 24% led to a slight decrease in friction from $\mu = 0.14$ to 0.10. At higher humidity (RH > 24%) a plateau with $\mu \approx 0.1$ was reached.

The experiment at reduced Hertz pressure of 50 MPa at RH ≤ 5% yielded a CoF of 0.28 (see green circle in Figure 4.23b). This CoF value is in line with the previous results presented in Section 4.5.1, where a decrease in pressure led to higher friction, for example at $P_{\text{Hertz}} = 250$ MPa a CoF of $\mu = 0.29$ was measured. For comparison, experimental literature values are depicted as blue symbols in Figure 4.23b, where the light blue area represents the typical friction range for experiments with no reported humidity. As visible from these data points, the friction measured in this thesis lies on the lower end; the resulting CoF are always similar or even lower than for comparable graphite/graphene systems [21, 29, 32, 54, 94].

In Figure 4.23c, the wear coefficient of the plate is depicted against the tested RH. The values were obtained by confocal microscopy, as described in Section 3.4.1. High wear was observed under dry pressurized air (RH ≤ 5%) and under high relative humidity values above 45%. In between, hence at intermediate RH, the wear coefficient was decreased by an order of magnitude and shows little variation. The counterbody wear coefficient is depicted in Figure 4.23d and evidently, the sphere did not suffer from any wear for humidity values ≤ 30 % RH. Under high humidity, the counterbody suffered from continuously more severe wear if the humidity was increased.

4.8.2 Electron Microscopy Investigations

To gain some further insight into the wear behavior of the graphite coating at different humidity values, SEM images were taken of the wear tracks and counterbodies. At low load (Figure 4.24a) a flattening of the roughness peaks was visible, hence barely no wear took place. At increased load, wear was drastically increased with a pronounced RH dependence being visible regarding the wear track width. A thin carbon layer remained in the middle of the wear track for RH ≤ 30%, (Figure 4.24b, c), which is in coherence with previous observations on substrates with industrial surface roughness [79].
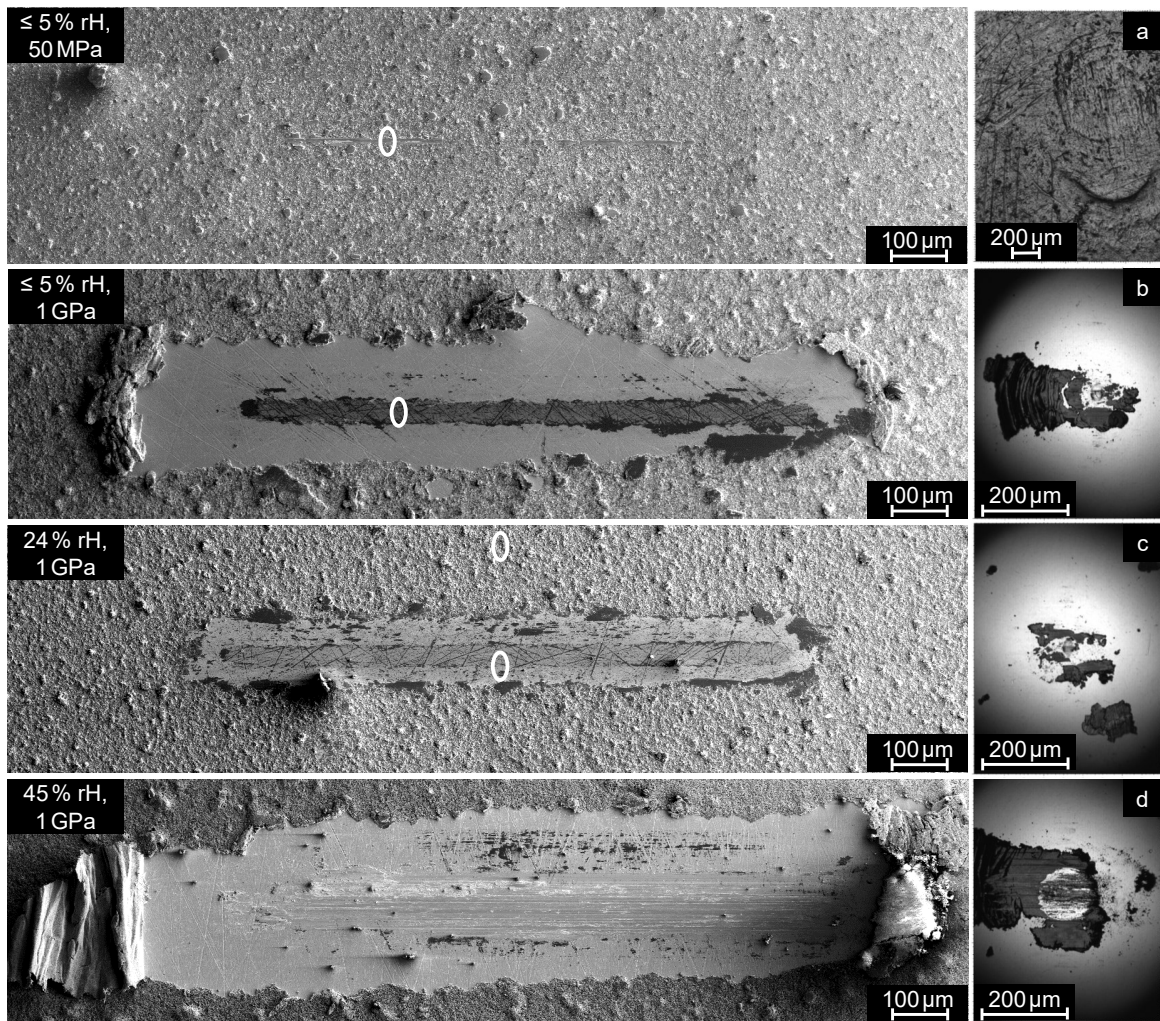
Figure 4.24: Scanning Electron Microscopy images of wear tracks and counter bodies taken after microtribometer experiments at different pressure and humidity values. (a) $\leq 5\,\%$ RH (dry pressurized air) at $50\,$MPa, (b) $\leq 5\,\%$ RH (dry pressurized air) at $1\,$GPa, (c) $24\,\%$ RH at $1\,$GPa, and (d) $45\,\%$ RH at $1\,$GPa. The marked areas in a), b) and c) represent regions of interest for a preparation of lamellae that are analyzed in consecutive TEM characterization. From [28].

This thin layer wore away at high RH ($45\,\%$ RH, Figure 4.24d) and adhesive wear is reported due to cold welding between steel counterbody and iron substrate. In addition, large material transport became evident, especially for high and low humidity values (Figure 4.24b and d). The main portion of the graphite seems to have delaminated during sliding and was piled up at the reversing points in a puckered, accordion-like fashion. Material transport onto the counterbody took place as well. For all experiments conducted at $1\,$GPa, a transfer layer on the steel sphere was visible (see Figure 4.24 right column). Under low loads, only small material transfer was observed. The material transfer and transfer film formation align with previously
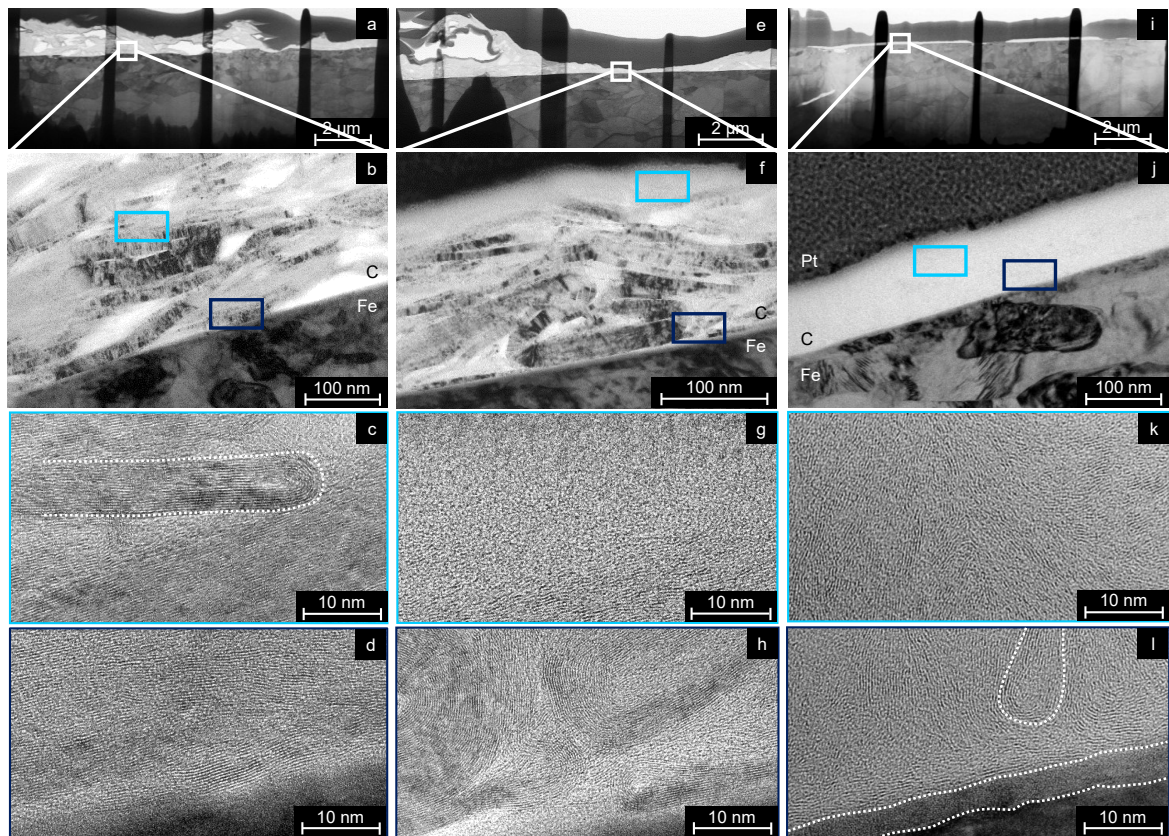
Figure 4.25: (upper half) Bright field transmission electron microscopy (BF-TEM) and (lower half) high resolution transmission electron microscopy (HR-TEM) images taken from TEM lamella prepared in an unworn region (a-d), after sliding under 50 MPa and in $\leq 5\,\%$ RH humidity (e-h), and after sliding under 1 GPa and in 24 % RH humidity (i-l). Marked in b,f, and j) are the iron substrate (Fe), the graphite layer (C), as well as the protective platinum layer (Pt) on the TEM lamella. Marked in light and dark blue are the approximate positions of the HR-TEM studies in the BF-TEM images. From [28].

discussed experiments (see Section 4.6.4) and literature reports [35].

As a next step, the structure of the formed thin carbon layer on the iron plate was analyzed in detail. To do so, four 10 µm wide TEM lamellae were prepared in collaboration with the group of Prof. Reinhard Schneider at the Laboratory for Electron Microscopy (LEM) at KIT (for the placements of the lamellae see Figure 4.24a, b, and c). One lamella originated from an unworn area to function as a reference, one was cut from the sample after the low load experiment at $\leq 5\,\%$ RH and 50 MPa, and two were cut after the high load experiments at 1 GPa ($\leq 5\,\%$ RH and 24 % RH, for the former see Appendix Figure A.7). This lamellae selection covered the full range of all relevant normal forces and humidity values.

The four lamellae were analyzed by bright field (BF) and high-resolution (HR)-TEM.

As visible in the left column of Figure 4.25, the prepared graphite coating has a porous structure due to the pile-up of individual graphite flakes during the deposition process. This structure is in line with the FIB analyses discussed earlier in this work in Section 4.3. If the magnification was increased (Figure 4.25b), graphitic bands became visible as darker stripes. They in turn consisted of large bundles of parallel graphene layers (Figure 4.25c). These bundles were randomly oriented in the majority of the graphite coating, except for the interface to the metal substrate, were parallel graphene layers were observed (see Figure 4.25d).

In the middle of Figure 4.25 structural changes of the graphite coating become evident after sliding at low load with $P_{\text{Hertz}} = 50\,\text{MPa}$. The coating is compressed to a thickness of 180 nm and the porous structure had disappeared (Figure 4.25f). Overall, the graphitic bands were not destroyed in the bulk of the coating (Figure 4.25f,h) but at the sliding interface, where a thin blurry structure had formed, which, upon larger magnification (see Figure 4.25g), was ascribed to a turbostratic carbon (t-C) structure.

At high loads of $P_{\text{Hertz}} = 1\,\text{GPa}$, the coating got compressed even further to a thickness of 30 to 150 nm (as visible in Figure 4.25i and j). The graphitic bands have been destroyed completely as well as the graphene bundles, which have disappeared in both the bulk and the surface of the graphite layer. As visible in Figure 4.25k, the whole layer consisted of t-C, hence the thickness of the t-C varied based on the applied load. Parallel graphene layers were observed only at the iron substrate interface (see Figure 4.25l). In this panel, a newly formed layer in between the graphene and the iron is marked with dotted lines. Energy-dispersive X-ray spectroscopy (EDXS) was conducted to analyze the chemical nature of the newly formed layer (see Appendix Figure A.8). According to the EDXS analysis, this layer consisted of iron carbides. The fourth lamella from the experiment at $1\,\text{GPa}$ and $\leq 5\,\%\,\text{RH}$ led to similar results as the one at $24\,\%\,\text{RH}$ (see Appendix Figure A.7), indicating that the structural transformation of graphite to t-C upon shearing occurred independently from the surrounding humidity.

For a detailed view of the coating surface with its structural transformation before and after sliding further HR-TEM analyses were performed. The initial graphene bundles in the graphite coating prior to any shearing were observed to be either parallel to the surface (Figure 4.26a) or perpendicular to it (Figure 4.26b). After sliding took place, these graphene bundles were transformed to t-C structures close to the surface both for low (Figure 4.26c) and high (Figure 4.26d) pressure values.

4.8.3 Hybridization of Carbon

The (HR)-TEM images allowed only a qualitative analysis of the shear-induced transformation from graphite to t-C. To get a quantitative insight, too, the fraction of sp^2-hybridized carbon was determined by spatially resolved electron energy loss spectroscopy (EELS). The carbon K-edge was measured at different regions of interest
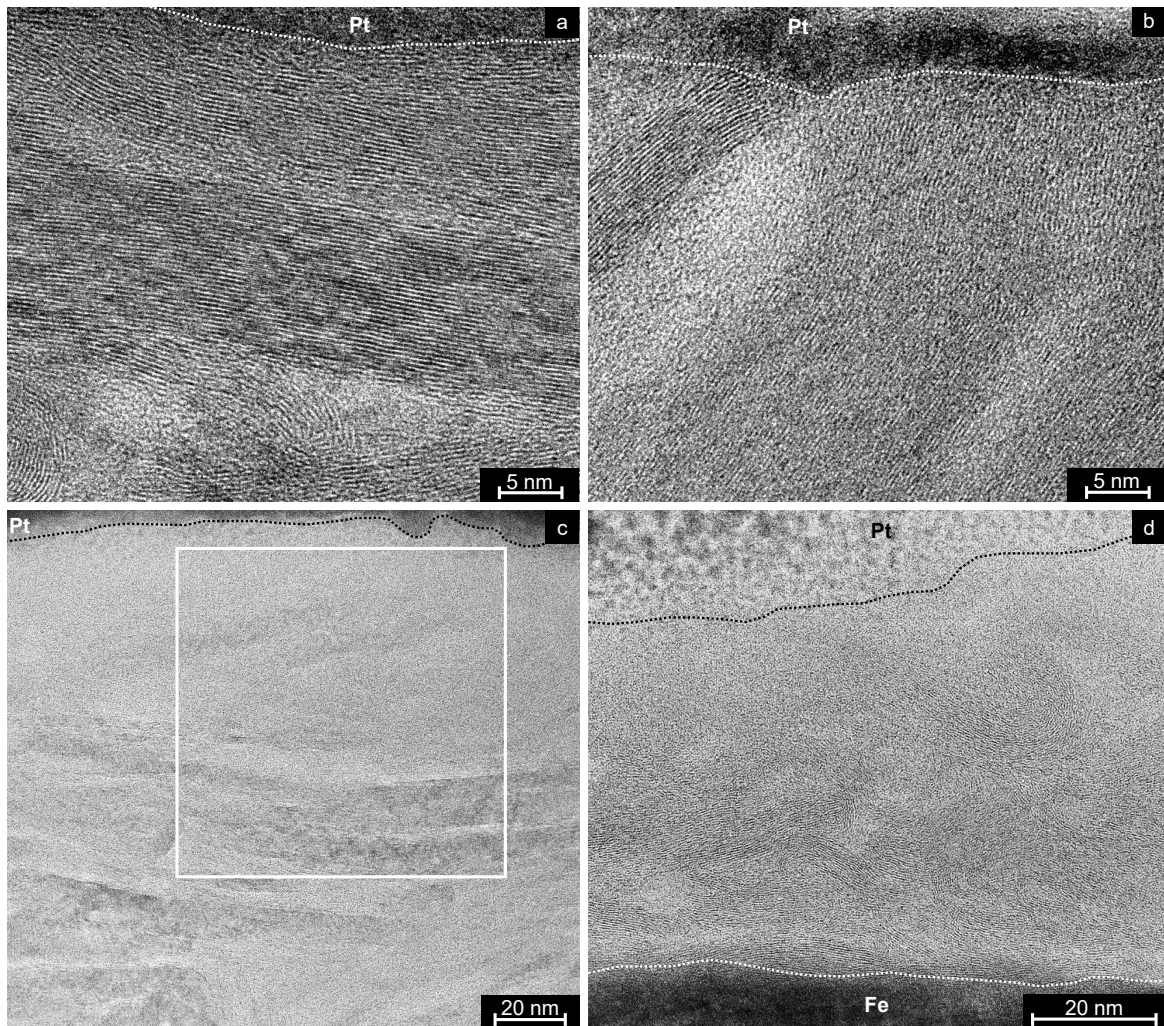
Figure 4.26: HR-TEM images of the graphite layer at the free surface (here covered by a Pt layer to avoid damage by TEM preparation) prior to (a,b) and after (c,d) the sliding experiments at (c) $50\,\mathrm{MPa}$ and $\leq 5\,\%\,\mathrm{RH}$; (d) $1\,\mathrm{GPa}$ and $24\,\%\,\mathrm{RH}$. For a larger magnification of (c) see Figure A.9, position marked with the square. From [28].

(ROI) which are marked in the left column of Figure 4.27. To calculate the carbon sp^2 content, the ratio of the integrated energy losses of the π^* and the σ^* state was calculated (for details see Section 3.4.5). The error for the determination of the sp^2 content is estimated to be 2%.

The unworn layer (Figure 4.27a) yielded an average sp^2 value of $(97 \pm 5)\%$ with a homogeneous value over the whole coating thickness, thus the airbrush deposition method resulted in a purely graphitic coating.

After sliding at $50\,\mathrm{MPa}$ and consequently exposing the sample to shear forces, a difference in the shape and height of the σ^* peaks was observed in Figure 4.27b. At the ROIs close to the surface and hence the sliding interface, the σ^* peaks were distinctly
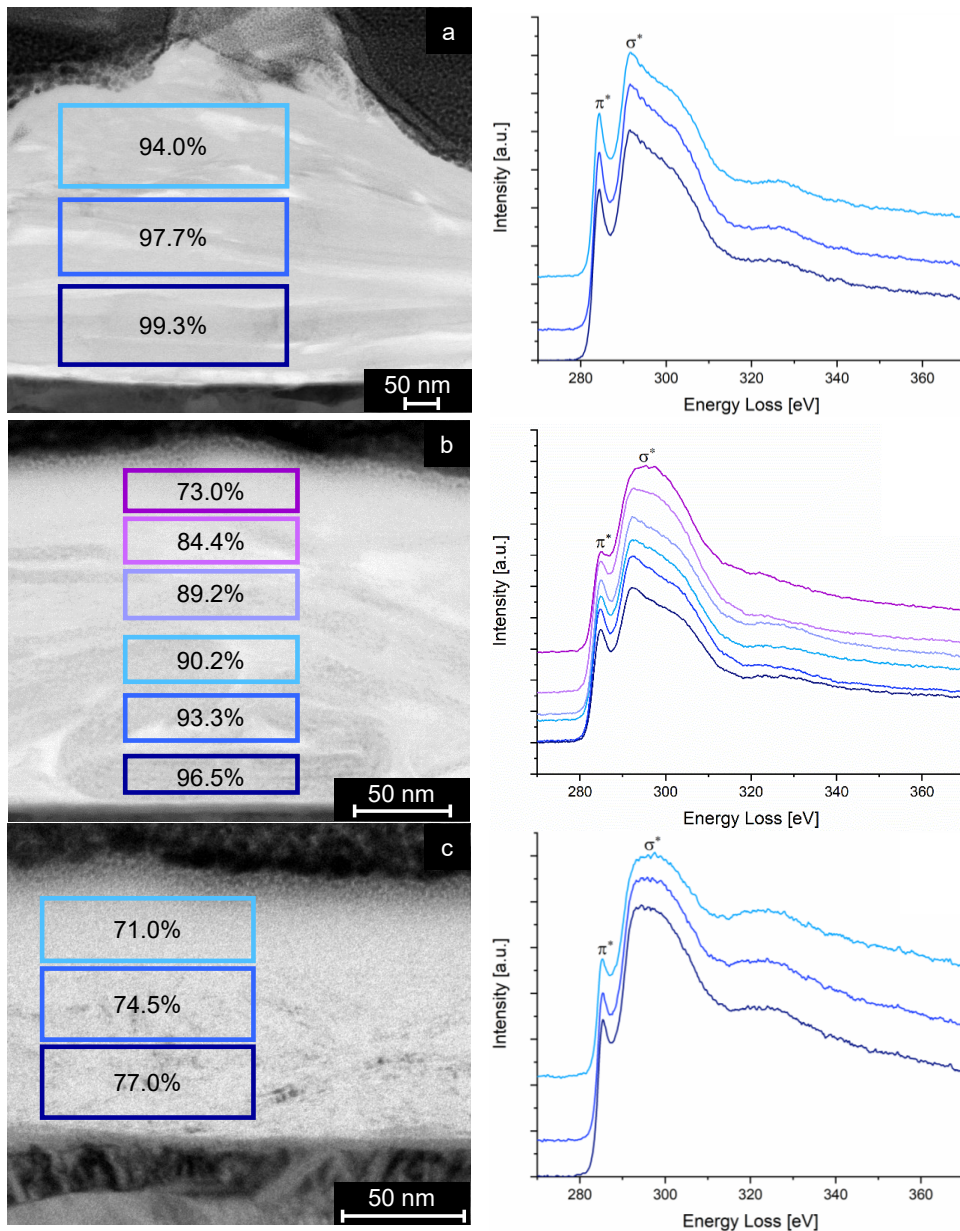
Figure 4.27: (left column) BF-TEM image of the regions of interests where EELS were taken in a broad, bar-like fashion. (right column) corresponding EELS spectra. (a) Unworn reference layer, (b) graphite after sliding experiment at 50 MPa, (c) graphite after sliding experiment at 1 GPa. For the sample at 50 MPa six ROI were taken instead of three, as the TEM analysis exhibited a more changing morphology throughout the whole layer than the other lamellae. From [28].

higher and broader, whereas the π^* peaks were diminished. As a result, the sp^2 was reduced by more than 20% in absolute numbers. Overall, a clear sp^2 gradient was observed ranging from 96.5% close to the substrate to 73.0% near the sliding interface. This correlates well to the observed t-C transformation of the coating reported in the

previous section, see Figure 4.25f.

At higher loads of $P_{\mathrm{Hertz}} = 1\,\mathrm{GPa}$, the sp^2 content (Figure 4.27c) was reduced overall and exhibited a gradient as well. A higher percentage of graphitic carbon was measured close to the iron substrate (77%) than at the sliding interface (71%).

4.8.4 Discussion

The previous results section resulted in multiple important observations. The SEM analyses (Figure 4.24) revealed a thin carbon film formed on the counterbody sliding against the graphite-coated iron plate for low loads. The transfer-film mass and coverage increased at the high load experiments. In coherence with the statements made in Section 4.4.3 sliding will take place between the carbon layer on the counterbody and the carbon layer formed on the iron plate for the majority of the experimental duration.

This observation was important as it matched the atomistic sliding simulations conducted at Fraunhofer IWM by Dr. Andreas Klemenz to a very high degree. In these simulations, two graphite plates were used as a starting configuration to investigate structural changes of graphite upon sliding on the atomic scale. More information about the methodological part of the simulations as well as detailed results can be found in the joint publication [28]. The most important finding that became evident only in the simulations, however, was a crucial water density which controlled the shear-induced transformation of graphite. Depending on the applied normal force, cold welding occurred between the two contacting graphite surfaces, followed by amorphization. This amorphization coincides with the t-C formation observed in the microtribometer experiments. Depending on the amount of water in the MD contact, two other behaviors may be observed as well: pure cold welding leading to high friction, if a low amount of water was present in the contact, and a lubricating water film if a lot of water molecules were present. Amorphization after cold welding occurs if the water density falls below the crucial water density, as revealed by the MD simulations. At higher normal forces, this crucial water density is increased.

The microtribometer experiments have shown that under moist conditions below 37% RH, the graphite material stays in the wear track as a thin carbon layer, leading to a low CoF of 0.10-0.14. According to both the deck-of-cards model [18] and the initial adsorption model postulated by Savage, this carbon material should keep its graphitic character [23].

Prior to any shear, the graphite coating had a porous structure and consisted of loosely stacked, randomly oriented graphite microcrystals (as seen by TEM analyses in Figure 4.28a). The microcrystals themselves were composed of randomly stacked multilayer graphene bundles, which exhibited a parallel orientation close to the iron substrate. EELS measurements confirmed the homogeneous sp^2 hybridization of $(97\pm5)\%$ and a hence high degree of graphitization throughout the whole coating. Thus, the

airbrush deposition method with a commercially available graphite suspension leads to a porous coating with high graphitic ordering.

During sliding however, this porous layer gets compressed and experiences shear forces which led to a tribo-induced phase transition, hence a t-C layer at the top of the graphite coating. At low loads of 50 MPa, only the uppermost layer was transformed to t-C while the bulk of the graphite coating got slightly compressed but retained most of its original structure (Figure 4.28b). In coherence, the sp^2 content measured by EELS revealed a distinct gradient from the iron substrate to the free interface (see Figure 4.27).

According to the deck-of-cards and adsorption model, parallel graphene layers should be observed at the sliding interface. As the results of this chapter have shown, an opposing behavior has been observed for the airbrush-deposited graphite coating, as no increased order but t-C formation occurred. The t-C layer thickness increases with an increase in normal load, as at high pressures of 1 GPa the whole solid lubricant was transformed (Figure 4.28c). The bulk of the coating lost its microscale ordering and transformed into t-C with shorter range ordering, with feature sizes in the order of 2-10 nm. Most likely, the transfer layer on the counterbody underwent the same phase transformation. Unfortunately, it was not possible to analyze the counterbody further in this work due to its small size of 2 mm. For a better overview, the t-C phase transformation in dependence on the load was schematically summarized in Figure 4.28.

In both pressure regions, the t-C material increased its sp^3 content by more than 20% which indicates densification. Hence, the low friction observed during the experiments cannot be explained by a velocity accommodation mode which would include shearing of the bulk t-C. However, the sliding of two t-C surfaces (on the plate and the counter sphere, respectively) seems to elucidate the low friction upon graphite lubrication. All these results lead to the conclusion that both the deck-of-cards/lattice-shear model (Figure 2.2a) as well as the adsorption model in its original form (Figure 2.2b) can be ruled out for commercial graphite lubricant sliding under both low and high contact pressures.

One has to mention that the transformation of graphite to t-C during tribological testing has already been reported by other groups but so far, this transformation occurred only during milling, where more severe conditions prevail [14–16]. This dissertation demonstrates that shearing is sufficient to trigger the t-C formation and that no high-impact mechanical milling is needed. Other research groups investigated similar tribosystems, for example carbon nanotubes [95], multilayer graphene [82], or t-C [96] in high pressure experiments and ambient conditions. When comparing their results with this thesis, similar trends are observed. Kumar et al. reported decreasing friction with an increase in humidity for t-C, too, but the polycrystalline graphite presented in the previous chapters decreased friction considerably more [96].

Bhowmick, Banerji, and Alpas conducted research on multi-layer graphene and reported the formation of amorphous carbon after sliding [82]. In contrast to this dis-
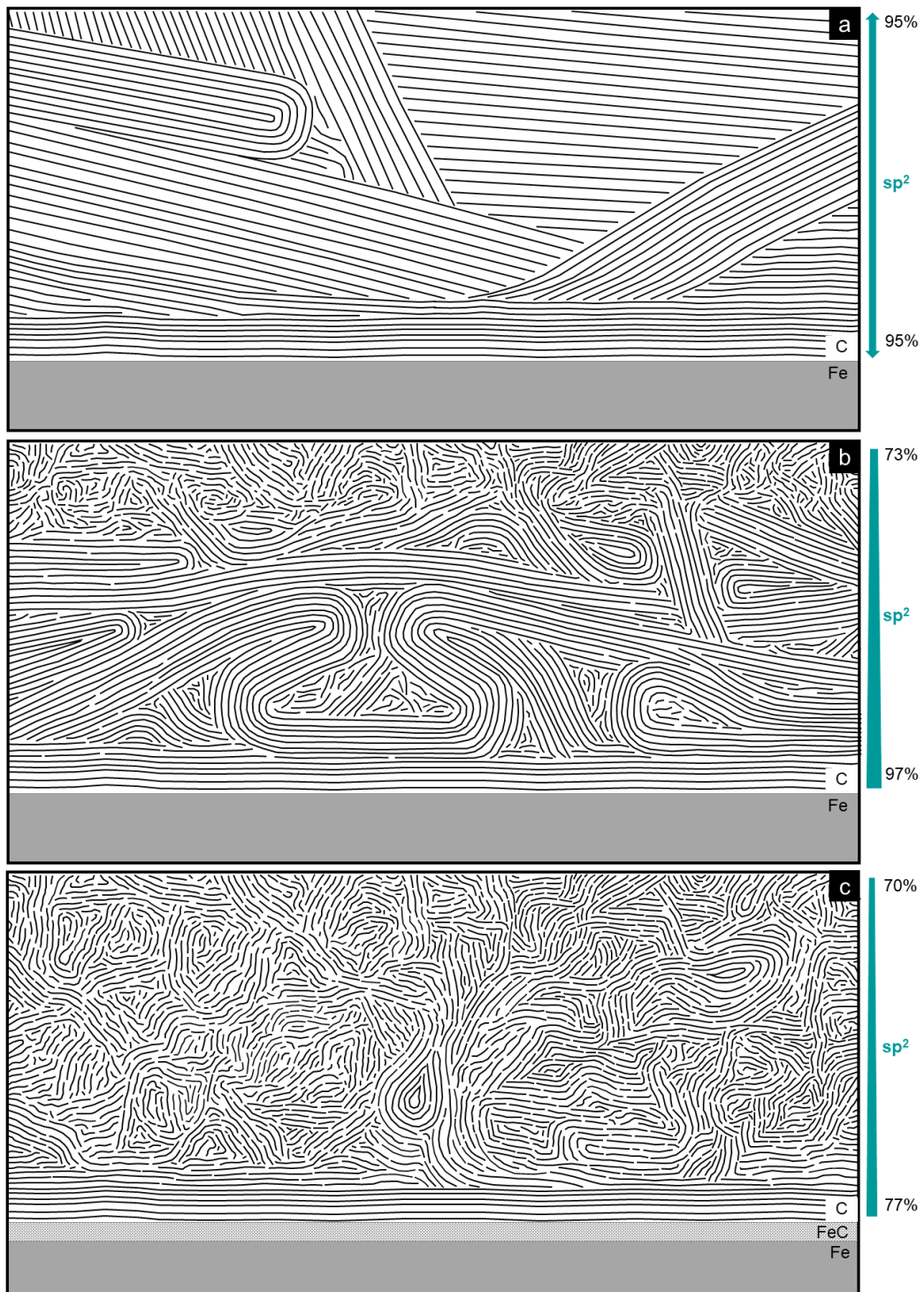
Figure 4.28: Schematic of the structure in the graphite solid lubricant prior to (a) and after sliding experiment with low (b) and high load (c). From [28].

sertation, only partial amorphization took place in their work, leading to graphene stacks embedded in the amorphous material, and hence no height gradient in the sp²

hybridization was observed. In the thesis presented here, the sp^2 gradient was homogeneous over the whole lamella and hence wear track width, and was evident both from the HR-TEM images and EELS analyses. The experimental results are further supported by the MD simulations conducted by Dr. Andreas Klemenz. In his simulations, upon shear of two graphite slaps, cold welding followed by amorphization was observed at comparable pressure and humidity regions, leading to the transformation to t-C and hence low friction in the range of $\mu = 0.14$. This CoF value is well within the range observed in the tribometric experiments.

Another mechanism for graphite lubrication discussed in the introduction is the roller mechanism proposed by Bollmann and Spreadborough [37, 97]. For the highly loaded contacts investigated in this work, no rollers were observed, neither in the MD simulations nor in the HR-TEM analyses. If applicable for high loads, one would have observed rollers on the surface of the compressed carbon material or at the very least at the sides of the wear track. As none of these rollers were observed, the roller mechanism does not apply to the highly-loaded contacts investigated in this thesis.

A missing puzzle piece, however, is an explanation for the high wear at high humidity values. As mentioned in Section 4.8.1, at high humidity ($\geqslant 37\,\%\,\mathrm{RH}$) the steady-state low friction was only short-lived and an abrupt rise in friction occurred due to extensive material transport of the graphite coating out of the wear track, as observed in previous research [79] Visible in Figure 4.23c is the extend of this trend: wear at high humidity is drastically increased and the wear scar in Figure 4.24d exhibits signs of cold welding.

This cold welding occurs despite the fact that abundant water should be present in the contact. One possible explanation for the high wear at high humidity is the presence of an additional force component due to capillary bridges and necks, as observed by Arif, Colas, and Filleter [98, 99]. The capillary bridges would lead to higher adhesion between the steel sphere and graphite coating. To examine this hypothesis, the capillary forces F_c were calculated as stated in Equation 4.1 [100].

$$F_c = 4\pi\gamma R \cos\theta \qquad (4.1)$$

In this equation γ represents the surface tension (for water at $25\,°\mathrm{C}$ circa $72.8 \cdot 10^{-3}\,\mathrm{N\,m^{-1}}$), R the counterbody radius ($1 \cdot 10^{-3}\,\mathrm{m}$), θ is the contact angle, which was estimated to be $60°$ for a mildly hydrophilic surface [101]. The capillary force F_c hence results as $F_c = 0.46\,\mathrm{mN}$. As this only accounts for 0.1% of the applied force, it is negligible, and the hypothesis of capillary necks being the major cause of high wear at high humidity can be omitted. Even higher hydrophilicity of the graphite with a contact angle of $\theta = 10°$ would only account for $F_c = 0.90\,\mathrm{mN}$. [28]

Another hypothesis for the high wear explanation at high humidity revolved around the idea that excess water could promote dissolution of the graphite or even delamination. The water might diffuse into and in between the coating-substrate interface at high humidity (here $\geq 45\,\%\,\mathrm{RH}$), which would lead to the formation of a water
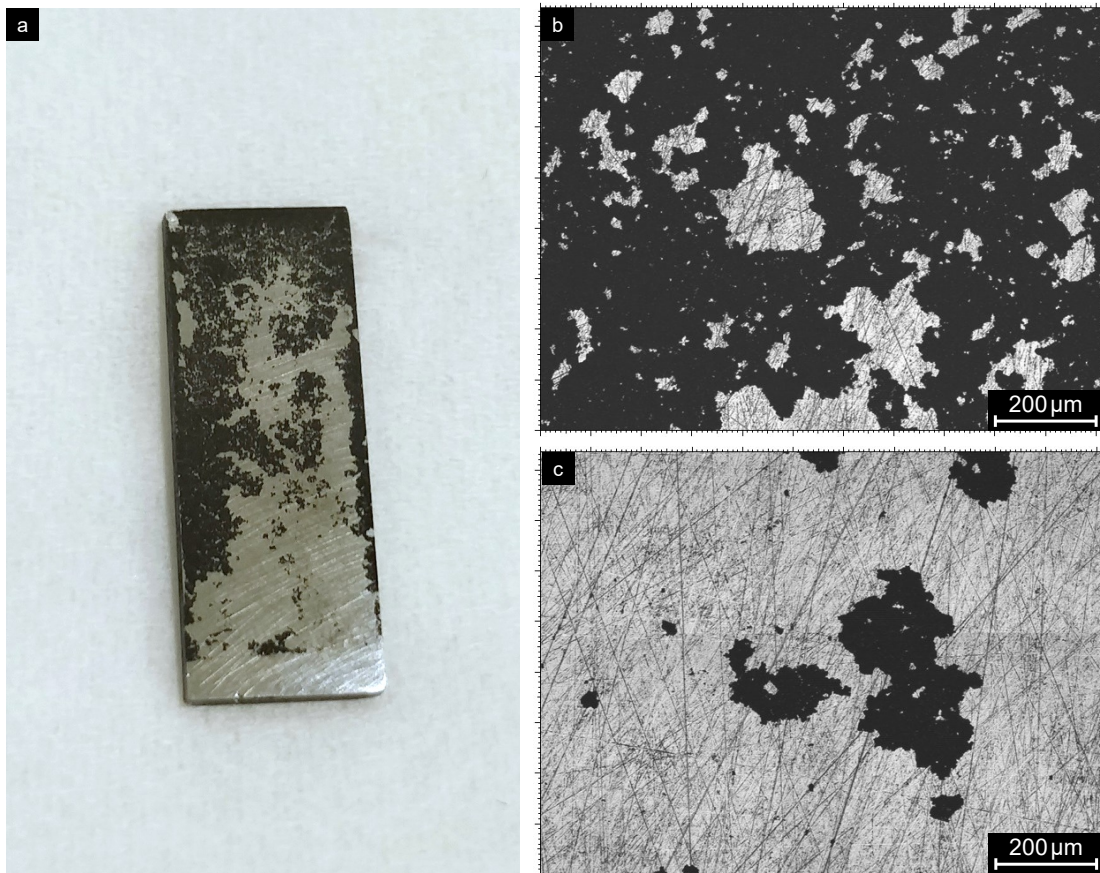
Figure 4.29: Photographic and microscopic images of an graphite-coated iron plate after the immersion experiment. (a) Photography of an graphite coated iron plate was immersed in water and put into an ultrasonication bath for 1 min. (b and c) confocal microscopy images of two randomly selected regions on the plate. As one can see, the majority of the coating was swept away as it detached easily from the substrate. From [28].

film. To test this hypothesis, two extreme experiments were conducted. In the first experiment, microtribometer experiments were run while guaranteeing complete immersion of the tribological contact. A drop of deionized water was placed on the plate and the sphere lowered until contact between both tribo-bodies was established. The results of this experiment are presented in Figure 4.23a, where the purple CoF line almost instantaneously rises to high values, accompanied by high wear coefficients (see Figure 4.23c and d). Hence, quick removal of the coating was observed.

To investigate this matter further, a graphite-coated iron plate was fully immersed in deionized water and placed in an ultrasonication bath. After the first few seconds, delamination of the coating occurred, followed by its complete removal after 1 min (depicted in Figure 4.29). These two experiments prove that the increased wear at high relative humidity can be linked to the dissolution of the coating by macroscopic amounts of water in the contact.
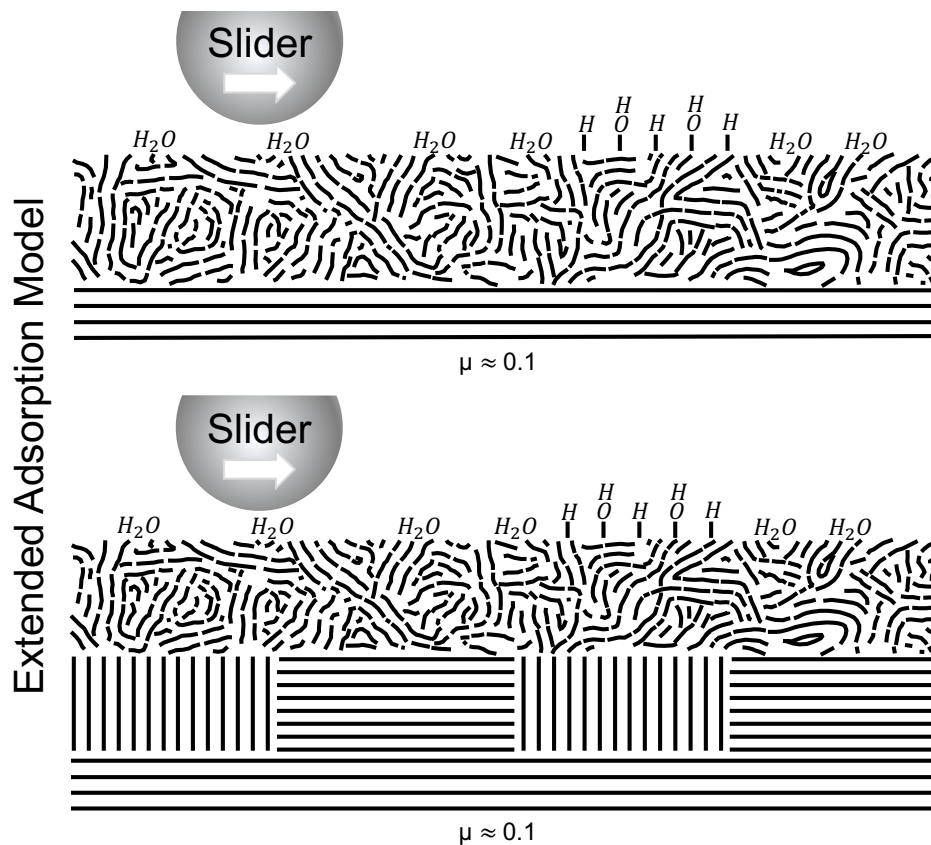
Figure 4.30: Adsorption model for graphite extended by shear-induced formation of turbostratic carbon for high loads (1 GPa, upper panel) and low loads (50 MPa, lower panel). Adapted from [28].

In conclusion, this chapter explored the applicability of a technical graphite coating as a solid lubricant under high mechanical loads. Both the experimental analyses and MD simulations revealed that the basic assumptions of the adsorption model apply for graphite lubrication at high loads, as friction is decreased by saturation of the newly formed edges and kinks. However, the t-C formation plays a crucial role as well. Therefore, in this thesis a new extended adsorption model is suggested to explain the good lubrication behavior of graphite and its humidity dependence, as displayed schematically below in Figure 4.30. The model is valid for a broad range of loads and relative humidities (as evident from the data collected at 50 MPa/RH $<5\%$ as well as 1 GPa/RH $<5\%$). This extension of the adsorption model closes a gap in the understanding of graphite lubrication and stresses the importance of the t-C formation, as it has been observed to be responsible for the long lifetime of the graphite coating and allows for large friction reduction.
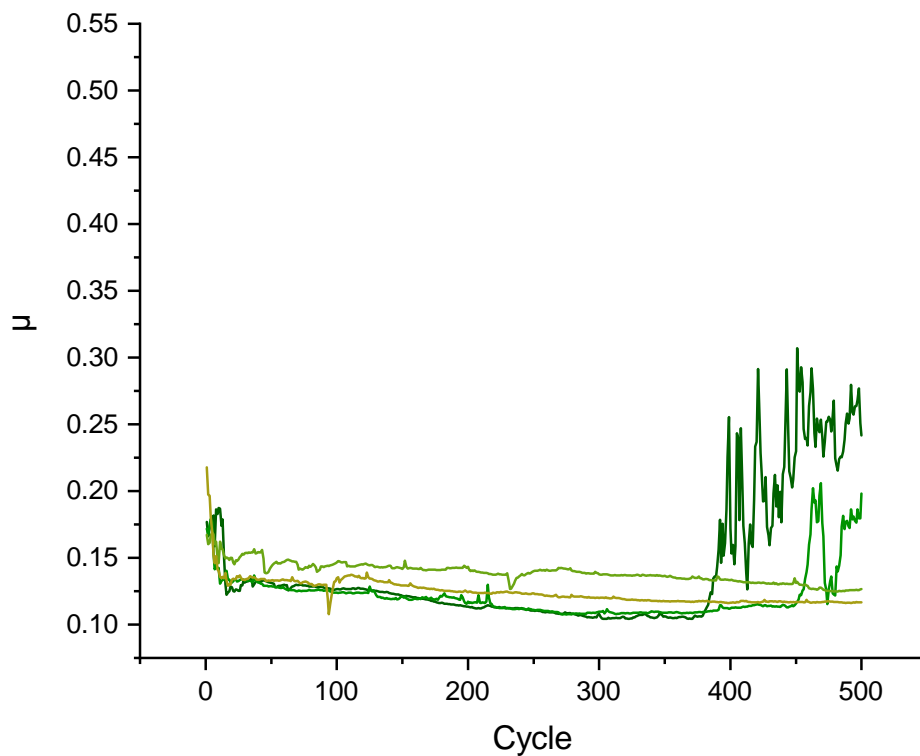
Figure 4.31: CoF of four microtribometer experiments conducted under a dry nitrogen atmosphere at $\leq 5\,\%\,RH$ and $1\,GPa$.

4.9 Dry Conditions

4.9.1 Nitrogen

The previous chapter revealed how the surrounding water content influences the graphite lubrication mechanism. But how does the solid lubricant perform in dry surroundings? As seen in the previous experimental studies (see subsection 4.8.1c) and literature publications, graphite suffers from severe wear due to dusting in dry regimes like nitrogen or ultra-high vacuum (UHV) [21, 29, 94, 96]. To investigate the behavior of the graphite airbrush coating in the absence of abundant water, a set of microtribometer experiments were conducted with the same parameters as before ($3.5\,\mu m$ coating thickness, $1\,GPa$ normal force). The experimental chamber was purged with dry nitrogen instead of dry pressurized air for $15\,min$, leading to a relative humidity of RH $\leq 5\,\%\,RH$. Depicted in Figure 4.31 is the friction data from these experiments, where a short running-in behavior was observed, followed by an average steady-state CoF of $\mu = 0.12$. On the one hand, this value is in the same range as for the experiments conducted in dry pressurized air ($\mu = 0.14$). On the other hand, the longevity was decreased under nitrogen atmosphere, as the lifetime ended for two of the four experiments prior to the entire experimental duration, leading to an average non-steady μ of 0.21 and an average lifetime of $459\,cycles$.
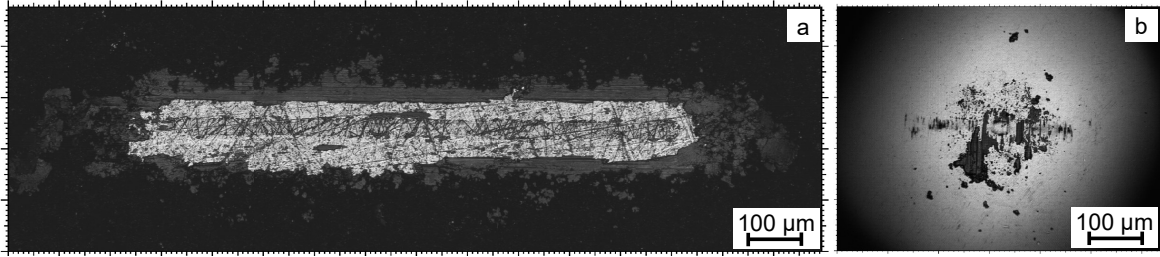
Figure 4.32: Confocal microscopy images of (a) plate and (b) sphere after experiments conducted under a dry nitrogen atmosphere at $\leq 5\,\%\,\mathrm{RH}$ and $1\,\mathrm{GPa}$.
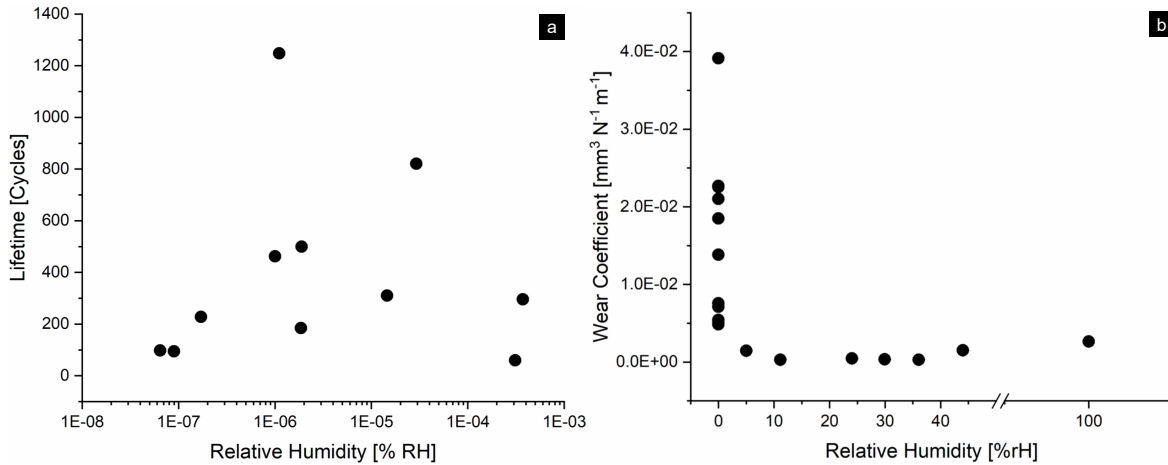
Figure 4.33: a) Lifetime vs. the relative humidity during the UHV experiments and (b) Normalized wear coefficients in UHV (marks on the left side) in comparison to the microtribometer experiments.

The graphite-coated iron plates and steel counterbodies were analyzed after the experiment by confocal microscopy (see Figure 4.32). Visible in the microscopy images is a graphite transfer onto the counterbody as well as the formation of the thin carbon film. When averaged over all four experimental repetitions, a slightly decreased wear of the counterbody was observed in comparison to the dry air experiments ($k_{Nitrogen} = 8.87 \cdot 10^{-4}\,\mathrm{mm^3\,N^{-1}\,m}$ instead of $k_{dryAir} = 1.45 \cdot 10^{-3}\,\mathrm{mm^3\,N^{-1}\,m}$). An increased wear coefficient was measured for the counterbody, with $k_{Nitrogen} = 1.79 \cdot 10^{-6}\,\mathrm{mm^3\,N^{-1}\,m}$; under dry pressurized air, no counterbody wear took place.

4.9.2 UHV-Tribometer

To reduce the surrounding humidity even more, ultra-high vacuum (UHV) experiments were conducted. The experimental parameters remained the same as in the microtribometer experiments wherever possible. The sliding length had to be adjusted to $100\,\mu\mathrm{m}$ instead of $1\,\mathrm{mm}$ due to constraints from the stage manufacturer. A mass spectrometer (MS) connected to the UHV chamber detected the atomic mass of wa-

ter (18 u) to quantify the humidity in the chamber. A vial of deionized water was connected to the chamber, which could be opened accordingly to tune the desired humidity.

To evaluate the tribological performance of the graphite coating in dry conditions, the CoF was calculated with a Matlab script (written at the Leibniz Institute for new Materials, Saarbruecken, Germany, adapted by Markus Stricker). The wear coefficients were gathered by analyzing confocal microscopy images taken after the experiment. For these calculations, the shape of the wear tracks was approximated with an elliptical shape. To gain insight into the wear mechanisms, the graphite-coated plates were analyzed by SEM after the experiments.

A total of 11 tribometric experiments was conducted under UHV with relative humidity ranging from $6.54 \cdot 10^{-8}$ to $3.15 \cdot 10^{-4}$ % RH, which are summarized in the appendix, see Figure A.10. All UHV experiments exhibited a similar CoF trend as the microtribometer experiments: after a short running-in period, the CoF remained stable for a limited and variable duration, after which friction rose abruptly and drastically to higher values. The experiments were stopped as soon as this rise in friction was observed. In total, an average steady-state CoF of $\mu = 0.11 \pm 0.04$ was measured. Overall, the CoF is slightly lower than for the dry nitrogen microtribometer experiments as well as the dry air experiments. The lifetime of the graphite coating vs. the relative humidity is depicted in Figure 4.33a. Clearly, no correlation between the humidity and lifetime could be observed in UHV with the low RH tested in this study. For all eleven experiments a shorter longevity was reached than during the microtribometer experiments: the longest lifetime of 1248 cycles resulted in an overall distance of 0.26 m. In comparison: the shortest lifetime in the microtribometer experiments was 153 cycles under 45 % RH, resulting in a distance of 0.31 m at the same load of 1 GPa until failure occurred.

The wear coefficient of the graphite plate under UHV is depicted in Figure 4.33b. For comparison, the data of the microtribometer experiments is plotted as well (dots at 5 RH and higher). The wear coefficients for all UHV experiments ranged between $4.86 \cdot 10^{-3}$ and $3.91 \cdot 10^{-2}$ mm^3 N^{-1} m, hence double or ten times higher than for the ambient microtribometer experiments. No correlation between the humidity and the plate wear coefficient was observed under the UHV environment. SEM images taken after the UHV experiments revealed severe adhesive wear in the sliding contact for all experiments (for an example see Figure 4.34) and no carbon-film formation.

4.9.3 Discussion

Most research groups reported a distinct increase in friction and wear upon insertion of the tribological contact into a nitrogen atmosphere. This friction increase is presumably due to the non-reactive nature of the nitrogen molecule, as the two nitrogen atoms are connected by a strong triple-bond. Consequently, nitrogen does not react easily in a normal environment. During the experiment, the continuous formation of
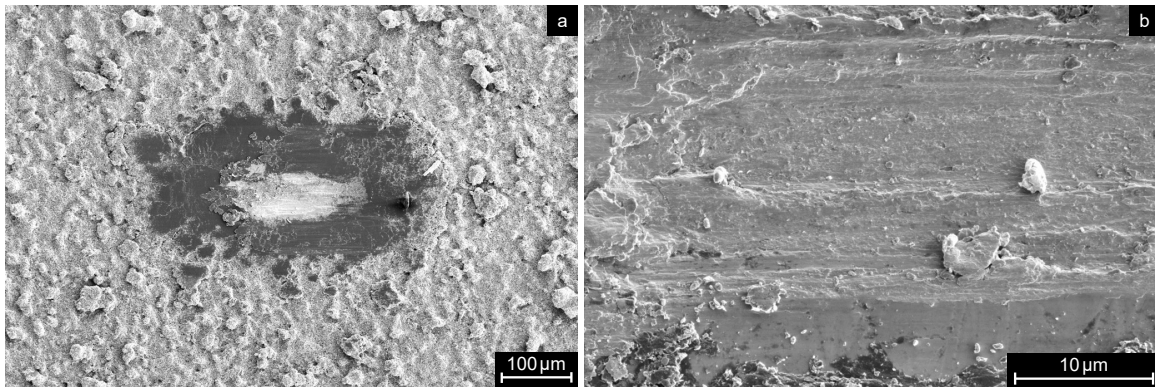
Figure 4.34: SEM images of the wear track of the graphite-coated iron plate after an UHV experiment at a water partial pressure of $5.40 \cdot 10^{-5}$ Pa and 1 GPa.

dangling reactive sites like edges, kinks, and defects occurs, which are highly reactive. Due to the absence of enough water molecules in the surrounding environment, they cannot be saturated and hence higher friction is yielded. [56, 82, 96, 102]

Zaidi, Robert, and Paulmier reported a slight friction decrease in the presence of inert gases like nitrogen due to their slow migration into lattice defects. This slow diffusion increased the mobility of the superficial crystallite, which hence could be oriented in an incommensurable way and decrease friction further. However, this effect occurs slowly and thus only displays its friction-reducing benefits if another, humid gas is present [103].

During the dry experiments presented in this chapter, friction was comparable to the experiments conducted in dry air and hence no influence of the nitrogen environment on friction was observed. Presumably, enough water remained adsorbed on the initial graphite surface to saturate the majority of defects formed in the beginning. However, it is important to mention that the formation of the thin carbon layer occurred, thus its formation is independent of the surrounding humidity. The structure of the layer was not analyzed by TEM. However, the MD simulations demonstrated that the surrounding humidity needs to be below the crucial water density for t-C formation to take place. In a nitrogen environment, the humidity will be lower than this density and the transformation to t-C might be accelerated. Nevertheless, if the humidity is too low, only cold welding will occur.

This negative impact at non-sufficient humidity might explain the decreased longevity observed in the nitrogen experiments. This cold welding will lead to an increased adhesion of the two graphite surfaces, thus more graphite material transport out of the wear track takes place. In conclusion, a nitrogen environment had a negative impact on the graphite lubricant presented in this thesis and the best tribological performance was reported under ambient conditions of 24 % RH.

The experiments under UHV environment delivered no clear correlation between the humidity and the wear coefficient or lifetime of the coating. The obtained CoF was

comparable to the experiments in ambient conditions, which is in contrast to other publications. In those, drastically increased friction was reported in dry conditions [21, 29, 94]. However, in most of these studies, the samples were heated to high temperatures prior to the tribological investigation to get rid of any remaining water and other volatile species incorporated in the carbon. During the experiments presented in this thesis, no heating step was conducted and hence the residual water suffices to saturate the defects during the experiment for a limited time.

In addition, a small track length of 100 µm was used for the UHV experiments instead of the 1 mm in the microtribometer. As visible in the SEM images, no thin carbon layer was formed. Due to the short length of the wear track, presumably, no additional graphite material could be transported in between the sphere and the plate (as it happens in the 1 mm microtribometer experiments) and hence no homogeneous thin carbon layer can be formed. This lack of layer formation might explain the high wear coefficient in the UHV environment, which is in agreement with previous publications on graphite lubrication where the solid lubricant performed worse in dry conditions than in ambient ones [21, 29, 94]. These results again stress the importance of the *in situ* formed t-C layer in the contact, without which the tribological performance suffers.

4.10 Amorphous Carbon

After reading the last section, a question that possibly comes into the reader's mind is: If the t-C layer is so important, would it be not more straightforward to start with an amorphous structure? For amorphous carbon, the running-in period might be considerably shorter and the lifetime could be drastically longer due to a better coating adhesion to the substrate. This hypothesis was investigated with two different amorphous carbon coatings. Both were deposited via physical vapor deposition (PVD). In a first experiment, a hard, amorphous carbon (a-C) deposited on 100Cr6 was provided by the Prometheus project funded by the Bundesministerium für Wirtschaft und Energie (BMWi). In a second set of experiments, a softer a-C coating was directly deposited onto the P1200 iron substrate by Patrice Brenner at the Center for functional Nanostructures (CFN) at KIT. Other than the sample material, all the experimental parameters for the microtribometer experiments were kept the same as for the previous experiments and the behavior of the coatings in varying humidity investigated.

4.10.1 Hard Amorphous Carbon Coating

Depicted in Figure 4.35 is the steady-state CoF over the range of tested humidity values. The coating exhibited a 2.8 µm thickness, an sp^3 content of 30%, and a coating hardness of 30 GPa (as determined by the Fraunhofer IWS and Joachim Faller). As evident from the figure, no clear influence of the surrounding humidity on friction was observed. Over the whole humidity range, higher friction was measured than with
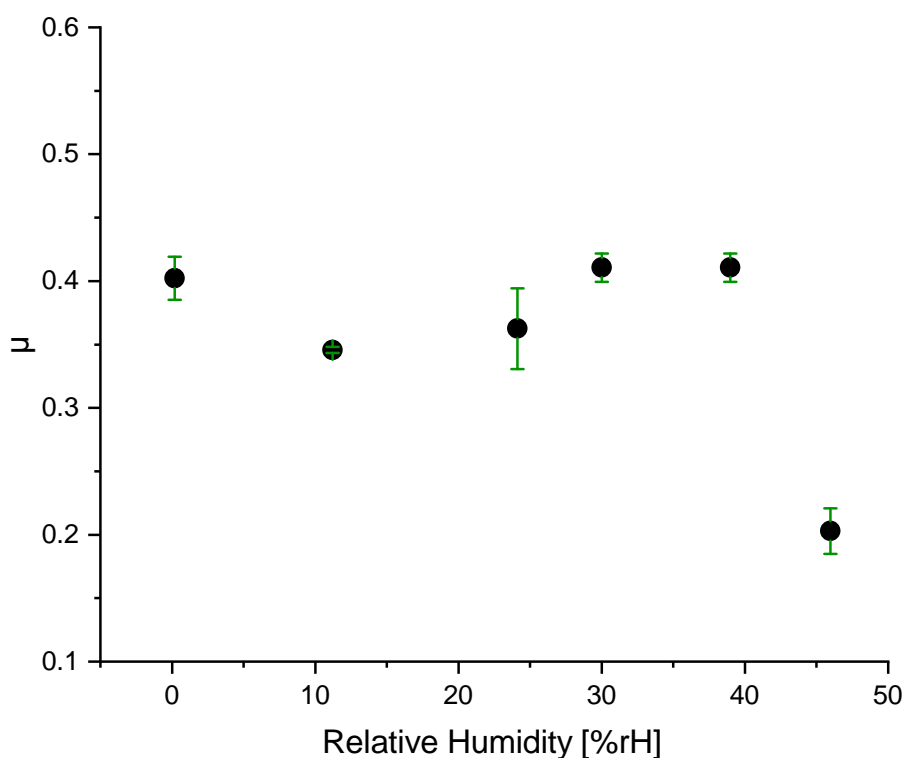
Figure 4.35: Steady-state CoF vs. the surrounding relative humidity for an a-C DLC coating vs. a steel sphere in a sphere-on-flat microtribometer experiment under a Hertzian pressure of $1\,\mathrm{GPa}$.

the graphite coating. This increase was due to the high hardness of the a-C coating ($(278 \pm 20)\,\mathrm{GPa}$) and due to the fact that friction on DLC coatings often correlates strongly to the surface finishing [104, 105]. The Prometheus a-C coating thus was not polished to a sufficiently low surface roughness, as all counterbodies suffered from wear after a short duration (see Figure 4.36).

4.10.2 Softer Amorphous Carbon

The a-C coating from CFN was applied onto the rougher iron substrates with a LESKER PVD 75 and evaporated with a Telemark e-Gun Multipoket from a Fabmate EVCFABEB-23 vessel with a carbon rod of $10\,\mathrm{mm}$ diameter. The obtained coating had a thickness of approximately $550\,\mathrm{nm}$ and conserved the topography of the original polished iron substrate. Unfortunately, the lubricant immediately wore away under the high loads tested in the experiments in the first cycles and resulted the steady-state CoF depicted in Figure 4.37. The CoF values are well within the range of an unlubricated metal-metal contact.
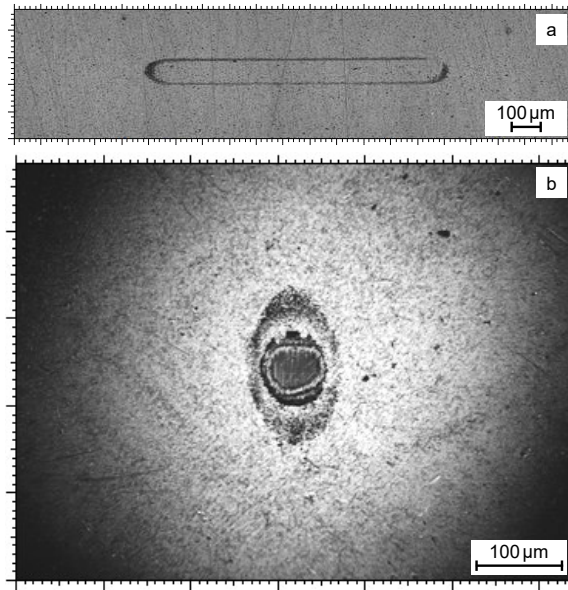
Figure 4.36: Confocal microscopy images of the a-C DLC plate (a) and the 100Cr6 counterbody (b) after the microtribometer experiment under a Hertzian pressure of $1\,\mathrm{GPa}$ and $8\,\%\,\mathrm{RH}$.
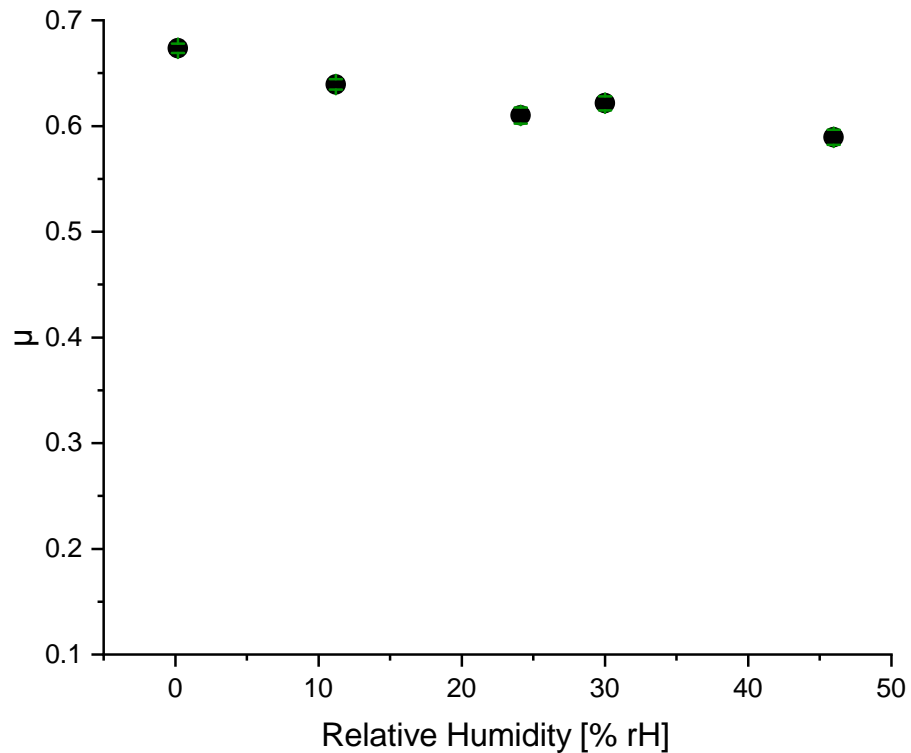
Figure 4.37: Steady-state CoF vs. the surrounding relative humidity for an a-C coating deposited by the CFN vs. a steel sphere in a sphere-on-flat microtribometer experiment under a Hertzian pressure of $1\,\mathrm{GPa}$.

4.10.3 Discussion

As evident from the two tested amorphous carbon coatings, none of them were suitable for a friction reduction in the same range as the graphite coating. For both a-C lubricants, the longevity of the counterbody was extremely short, which in turn led to high wear of both tribo-bodies. One reason for the better performance of the *in situ* formed t-C with the graphite lubricant than the CVD obtained a-C coatings could lie in their differing hardness. The initial graphite coating is relatively soft, easily compressed, and has a porous structure. The two a-C coatings, however, are considerably harder – hence they function as files at the high-pressure range investigated in this thesis, quickly wearing away the counterbody. The surface roughness furthermore increases this file-like behavior. In conclusion, for successful lubrication with graphite under high loads, only starting with the soft graphite material will lead to a high friction reduction. Upon shearing, the solid lubricant will get transferred *in situ* into the desired t-C material.

5 Results: Rolling Friction

All previous sections investigated the lubrication behavior and mechanism of graphite under sliding motion. However, the desired application in this project is a rolling bearing, hence the lubrication behavior has to be analyzed under rolling motion as well. Based on the results presented in the previous chapter, multiple questions arise: How does the graphite coating behave under a rolling motion under high loads? Can the results under sliding motion be generalized to a wider range of tribological applications? How does the slide-to-roll-ratio (SRR) influence both friction and wear? Will there be a thin carbon layer formation, and if yes, how will it be influenced by the sliding percentage? All these questions are going to be discussed in this chapter.

The experiments were conducted in a mini traction machine (MTM, for details see 3.3.3) on bearing rings (INA, LS2035). In the first characterization step, the areal surface parameters of the rings were determined by white-light interferometry (WLI). The obtained parameters were: $S_a = 129\,\text{nm}$, $S_q = 255\,\text{nm}$, and $S_z = 2717\,\text{nm}$. Prior to the coating deposition process, the rings were cleaned with brake cleaner, acetone, and isopropanol in succession and coated with graphite to obtain a thickness of $(3.5 \pm 0.2)\,\text{μm}$.

In the MTM setup, both tribo-bodies can be rotated individually at different velocities to tune the SRR to any desired value. The author of this dissertation is not aware of any publications that report the real SRR in axial rolling bearings, as it is difficult to measure it in the real contact. However, in a comparable work by Stratmann et al., the influence of SRRs on the tribofilm formation in rolling bearings was investigated for a SRR range between 0 and 15% [106]. Hence, the SRR tuning range analyzed in this dissertation is valid – for the experiments, the SRR was changed between 0% (pure rolling) and 15% in steps of five. The chamber was purged continuously with dry pressurized air to keep the humidity constant at $\leq 5\%$ and a normal force of $15.6\,\text{N}$ yielded a Hertzian Pressure of $1\,\text{GPa}$ to be comparable to the microtribometer experiments and the desired application.

5.1 Friction

The experiments conducted at four different SRRs resulted in the frictional data summarized in Figure 5.1. Overall, the steady-state CoF lies between $\mu = 0.06$ and 0.12 for all experiments, which is similar to or slightly lower than for the sliding experiments. For all SRRs, there are multiple "steps" observed in the CoF development and the
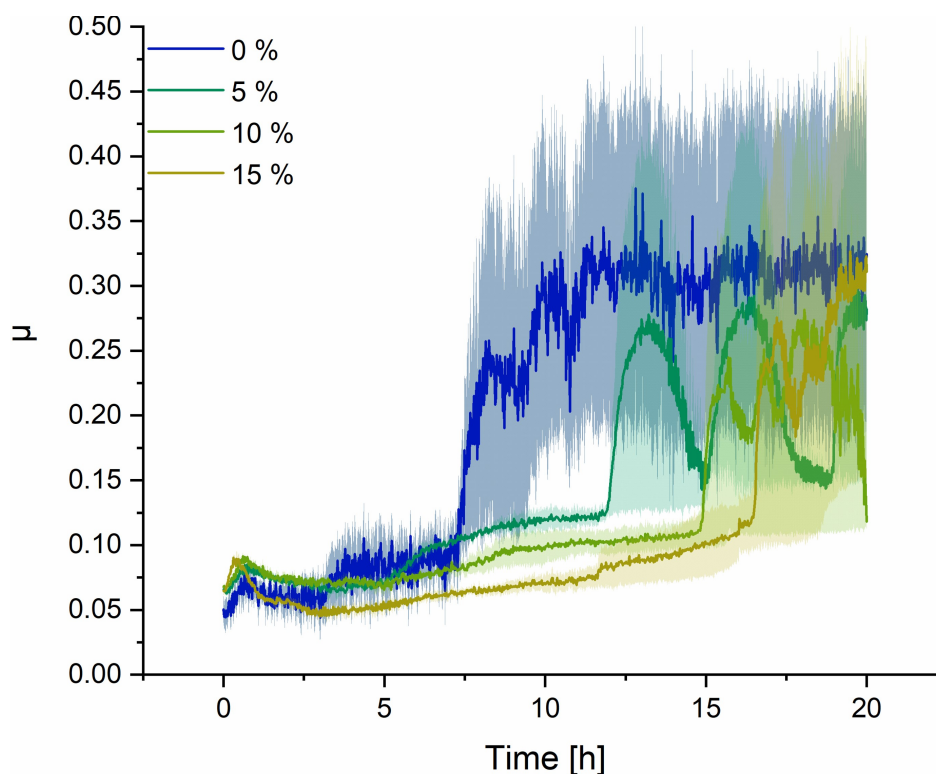
Figure 5.1: Average CoF vs. the experimental duration for the different investigated SRR. The solid lines represent the average of three repetitions whereas the translucent area represents the standard error of the mean.

coating lifetime ends prior to 20 h as friction rises abruptly. At the end of the lifetime, friction rose to values of circa $\mu = 0.6$. In general, a decrease of the steady-state friction while increasing the SRR was observed in Figure 5.1, with an exception of 0% SRR ("pure" rolling), where lower steady-state friction was reached, however, the scattering of friction was drastically larger for this SRR value than for the others.

5.2 Lifetime and Wear

Figure 5.2 represents the averaged lifetime for the three experimental repetitions over each investigated SRR. The end of the lifetime was defined as the moment where the CoF exceeded the previous 10 cycles by 30%. The maximal possible lifetime was 20 h, as this was the experimental duration. As evident from the graph, increased longevity is reported with increasing SRR with an asymptotic trend (presumably due to the limited lifetime of 20 h). At 0% SRR, the lifetime of the coating ended after 12.2 h and a large scattering was observed. For 5%, a lifetime of 15.6 h was measured, at 10% 18.2 h, and at 15% 18.8 h. As seen and discussed in the previous chapters, the longevity of the coating is limited due to the material transport of the graphite out of the wear track, hence leading to lubricant starvation.
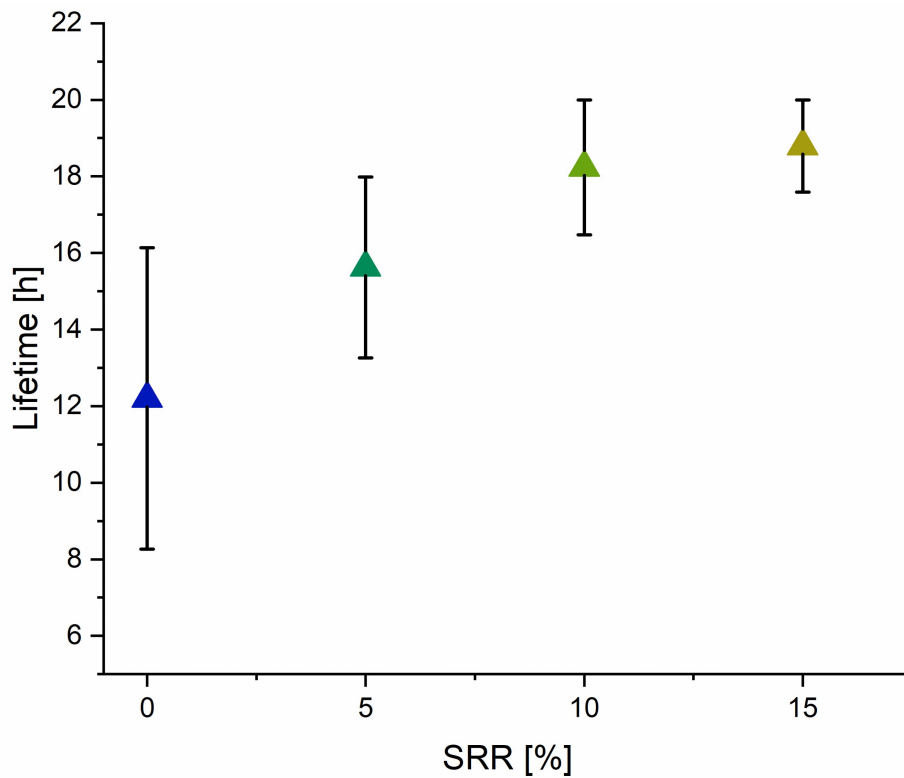
Figure 5.2: Average lifetime vs. the investigated SRR. The error bars represents the standard error of the mean for the three repetitions.

Listed in Table 5.1 is the wear coefficient data for the graphite-coated rings for all investigated SRR values. It is important to note that for these calculations, only the sample sets which survived the entire experimental duration were incorporated. By doing so, the influence of the SRR on wear protection can be derived. The "non-surviving" samples showed signs of severe abrasive and adhesive wear due to extensive material transfer out of the contact.

When analyzing the wear coefficients, it becomes evident that the wear of the graphite-coated ring decreased if the SRR was increased. This observation is in line with the previously discussed improvement in longevity at higher SRR. As the incorporated data originated from samples that endured the entire experiment, no visible wear was detected on the counterbodies.

Table 5.1: Normalized wear coefficient.

SRR [%]	Wear Coefficient ring [mm^3 N^{-1} m^{-1}]	Standard Error of the Mean [mm^3 N^{-1} m^{-1}]
0	failure	—
5	$1.19 \cdot 10^{-6}$	$2.17 \cdot 10^{-7}$
10	$6.02 \cdot 10^{-7}$	$5.20 \cdot 10^{-9}$
15	$4.88 \cdot 10^{-7}$	$2.50 \cdot 10^{-8}$
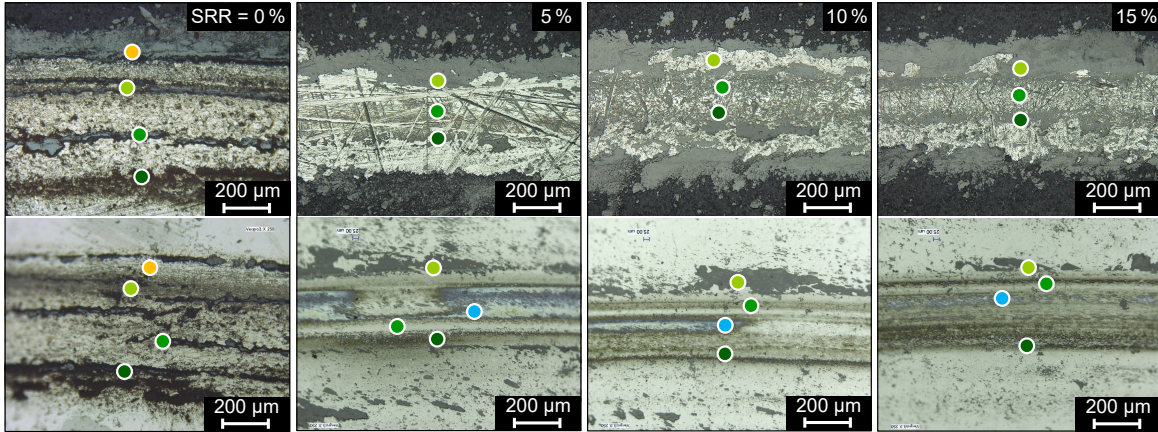
Figure 5.3: Digital microscopy images of the graphite-coated rings (upper panels) and the respective spheres (lower panels) after the 20 h MTM experiments for the four different SRRs. Marked by the coloured circles are the regions analyzed by Raman spectroscopy.

5.3 Thin Carbon Layer - Microscopy

To investigate the origin of the steps in the frictional behavior as well as the reason for the decrease in friction and increase in longevity with increasing SRR, images were taken with a digital microscope at a 250x magnification. Another focus of this analysis was the formation of the thin carbon film and whether its formation is influenced by the SRR.

The digital microscopy images are displayed in Figure 5.3, where the graphite-coated rings are presented in the upper panels and the corresponding counterbodies in the lower panels. For all SRRs except for 0% the formation of a thin carbon layer was observed, hence a slide percentage of 5% sufficed. Even at 0% SRR some sliding will occur due to microslip, but apparently, this is not enough for the layer formation. The coverage and homogeneity of the thin carbon layer increased with increasing SRR.

When comparing the images to the ones acquired after the sliding microtribometer experiments, similar trends in terms of material transport were observed. Material transport on the ring led again to compression of the coating on the wear track sides and the majority of the material has been pushed to the sides as well. Material

transfer onto the counterbody was observed as well in the form of larger graphite flakes. However, a new characteristic was observed: Visible especially on the counterbody of the 5-15% SRR experiment are iridescent areas.

These iridescent areas were observed on both the rings and the spheres for all experiments that exhibited a lifetime of 20 h, with them overall being more abundant on the counterbodies. An exception to this trend were the samples after experiments at 0% SRR, where no iridescent spots were visible. Presumably, the shimmery nature of these spots is created due to the effect of thin film interference [107], as observed for example for thin soap films on water. In consequence, in these areas, a thin tribofilm consisting of carbonaceous species could have been created. The approximate thin film thickness can be calculated by considering the blue color of the tribofilm. This means that the opposing color of the white light used for the investigations (in this case orange light, wavelength $\lambda = 585$ - 650 nm) is adsorbed or interferes in a destructive way, respectively. For a perpendicular beam, the thin film thicknesses d where destructive interference of orange light occurs can be calculated in the following way [107]:

$$2d = \frac{2k}{n} \cdot \frac{\lambda}{2} \quad (k = 1, 2, ...) \tag{5.1}$$

The refractive index n for amorphous carbon layers lies between 1.7 and 2.6 [108]. With these numbers, the thickness of the blue tribofilm can range from 112 to 191 nm depending on the wavelength of the adsorbed orange light and the used refractive index. This is comparable to the thin carbon layer observed during the sliding experiments, where a thickness of 30 to 150 nm was determined via TEM analyses. To investigate the chemical nature of the blue tribofilm, Raman spectroscopy was conducted and is discussed in the following section.

For the sample conducted with 0% SRR, dark particles are evident in the wear track on both the steel ring and counterbodies. Most likely, they materialized as wear set in, thus they are likely to consist of iron oxides and degraded graphite particles.

5.4 Thin Carbon Layer - Raman Spectroscopy

Raman spectroscopy analyses were conducted to analyze the chemical composition and nature of the iridescent areas, gather information about their homogeneity and coverage, and investigate whether the composition of the carbon layer varies depending on the position in the wear track. For this goal, two key characteristics were calculated and analyzed: The carbon G band position and the intensity ratio between the D and the G peak.

On each sample, at least three to four regions of interest were measured. The thin carbon film and the alleged tribofilm were destroyed as soon as wear set in (lifetime < 20 h, hence the results represented in this focus on experiments that endured the entire duration. For the MTM experiments at 0% SRR, a shorter lifetime was observed
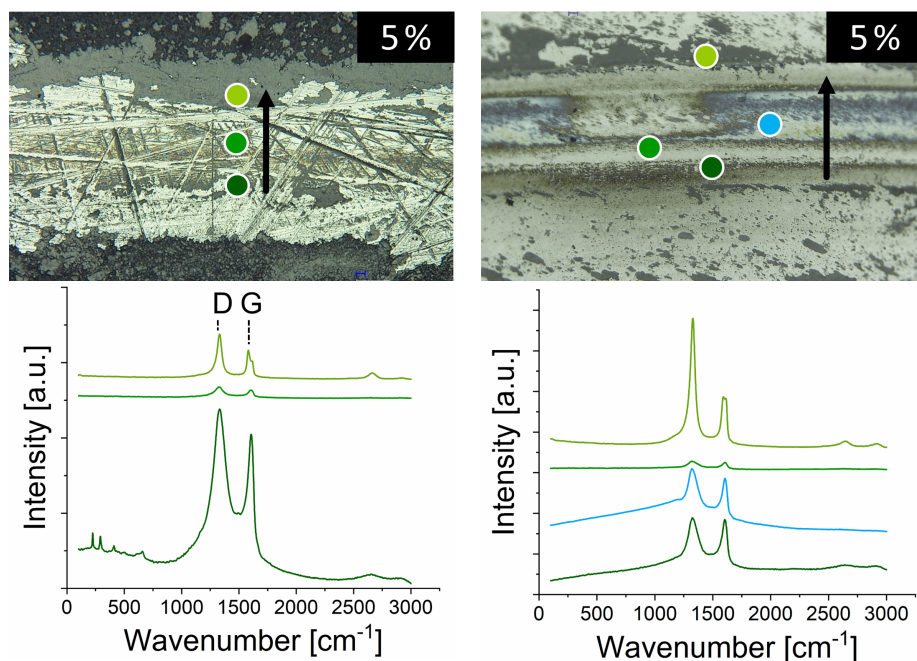
Figure 5.4: Digital microscopy images and Raman spectra of the graphite-coated ring (left panels) and sphere (right panels) after MTM experiments at 5% SRR.

at all repetitions, hence no thin carbon film or tribofilm could be investigated for this parameter set. However, the analysis of them gave insight into the chemical degradation of the substrate if lubricant starvation occurred (for more information see the following sections).

Pictured in Figure 5.4 are the Raman analyses for the 5% MTM sample as an example for the general analysis. On the left-hand side, the analyzed regions of the ring and the respective Raman spectra are displayed, while on the right-hand side, the respective data of the sphere is visualized. Overall, different peak signatures are observed in the spectra. For both tribo-bodies, the most dominant peaks are the D and the G-band. The G-band is accompanied by a shoulder at $1620 \, \text{cm}^{-1}$, the so-called D'-band. Both the D and D'-band originate from defects in the graphite structure [13, 109, 110]. This D'-band was usually accompanied by two smaller peaks in the higher wavenumber range at 2500-2800 and circa $2950 \, \text{cm}^{-1}$, which correspond to the 2D and D+G band, respectively [13, 109, 110]. The 2D band corresponds to the overtone of the D band while the D+G combination band is induced by disorder [13, 109, 110]. They were observed for all tested SRR (expect 0% and more dominant on the outer side of the wear track for both the rings and the spheres).

For some of the Raman spectra, iron oxide peaks were detected in the lower wavenumber range from circa $400\text{-}800 \, \text{cm}^{-1}$ [32, 111]. These iron oxides were observed for all samples where (partial) abrasive wear took place, hence mostly for the samples where the graphite did not endure the entire experimental duration. For these destroyed samples, the Raman spectra consisted of the iron oxide bands and a broad D-band, while the G-band was comparably small or even absent. Hence, tribooxidation of the
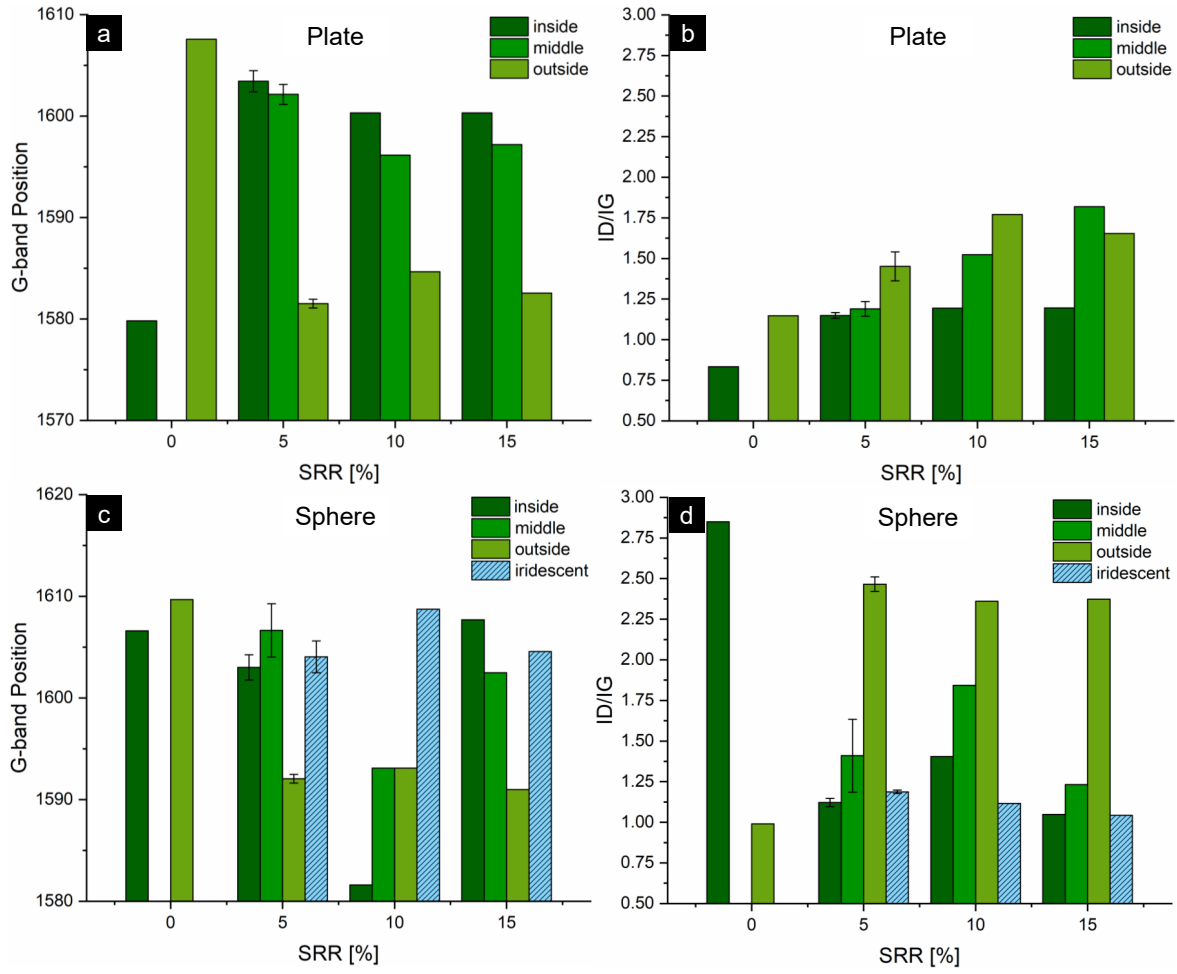
Figure 5.5: Raman G-band position and intensity ratio of graphite-coated rings (upper panels) and counterbodies (lower panels) after the 20 h MTM experiments for the four different SRRs.

steel substrate took place if the graphite coating got worn away. The Raman spectra of samples from all SRR values are depicted in the appendix (see Figure A.11 to Figure A.14) for a complete overview.

As mentioned in the paragraphs above, the chemical nature of the iridescent areas and their coverage should be analyzed. Depicted in Figure 5.4 are the regions measured by Raman (the blue dot represents the iridescent areas) and the corresponding spectra for the 5% sample. A G-band position of $1606\,\mathrm{cm^{-1}}$ and $I_D/I_G = 1.18$ was gathered. These values were quite similar for all SRR values higher than 0%. Averaged over all SRRs from 5 to 15%, an average G-band position of $(1605 \pm 1)\,\mathrm{cm^{-1}}$ and an intensity ratio of $I_D/I_G = (1.14 \pm 0.03)$ was calculated for the iridescent areas.

In Figure 5.5, the G-band position (a, c) and I_D/I_G ratios (b, d) for all measurement positions are summarized over the different SRRs. The spectra were recorded on the inner side of the thin carbon layer, in the middle, on the outer side of the layer, and

iridescent areas if present. These measurements were conducted for both the ring (a, b) and the corresponding sphere (c, d). On the rings, iridescent areas were visible but usually not large enough for reliable Raman analyses, thus this position was omitted for them.

When visualizing both the G-band position and the I_D/I_G intensity ratio for the rings, a clear trend was observed: When going from the inside of the wear track to the outside of it, the G-band position shifted to lower values for all SRR $\geq 5\%$, e.g. from 1607 to 1582 cm^{-1} for 5% SRR (see Figure 5.5). At the same time, the intensity ratio between the D and G bands increased, e.g. from 1.15 to 1.52 for 5% SRR. But not only the investigated region in the wear track plays an important role – the SRR influenced the Raman results as well. On the rings, a clear correlation between the I_D/I_G ratio and the SRR was observed: as the SRR was increased, the I_D/I_G ratio grew as well. For the G-band shift, the influence of the SRR was less pronounced.

On the counterbodies, similar to the graphite-coated rings, an influence of the wear track position on the I_D/I_G ratio was observed (see Figure 5.5d). The G-band position displayed stronger fluctuations on the counterbody than on the rings (Figure 5.5c), hence no clear trend could be derived. For the SRR influence, no clear correlation to the G-band position or intensity ratio was evident on the counterbody.

5.5 Discussion

The previous sections summarized the results on the lubrication behavior of the airbrush-applied graphite coatings under rolling friction. The main goal of these analyses was to elucidate whether a thin carbon layer forms even if the sliding percentage is below 100% (pure sliding), whether any differences in its appearance become evident, and how friction, lifetime, and wear are influenced by SRR changes. So far, most literature studied the influence of graphite under rolling friction focused on the use of graphite as an additive oil or grease [83, 112–114].

For all SRRs, some of the experiments failed before the end of the experiment due to starvation of the lubricant. Hence, it became evident that relubrication is needed. Ideally, the graphite coating should guarantee lifetime lubrication of a rolling bearing, thus the longevity must be increased by improving the coating adhesion to the bearing substrate. By doing so, the material transport out of the wear track will decrease, but material transfer onto the rolling bodies still must be guaranteed. There are multiple ways to improve the adhesion of a coating to a substrate: surface roughness increment, chemical treatment, usage of a binder material, etc. [115, 116]. In the scope of the SPP2074 project, the IPEK tested commercially available coatings in a test rig. Manipulating the bearing surface would be difficult and costly, hence this possibility is not suitable for the project. The chemistry of the bearing could either be tuned by coating the inner bearing with an adhesion layer or by mixing the graphite with a binder material. The latter is already frequently done in pencil production, where

clay is added as a binder to graphite to tailor the hardness and wear rate of pencils [117].

The MTM experiments furthermore proved that an SRR increase led to both a lower steady-state friction coefficient as well as longer longevity and lower wear. The following two points could deliver an explanation for this behavior: 1. The coverage and homogeneity of the thin carbon layer might increase as well with higher SRR values. The digital microscopy images support this hypothesis, as the thin carbon layer grew in width and thickness at higher SRR (see Section 5.3). 2. A tribolayer formation might enhance tribological performance further. The digital microscopy images showed blue iridescent areas for all samples with SRR = 5% or higher. This iridescence could be due to thin film interference and thus a thin tribofilm of around 112 to 191 nm thickness could be formed on counterbodies and rings.

To prove the existence of a tribofilm, Raman analyses were conducted. They revealed a graphite structure dependence on the wear track location with a G-band shift to lower and I_D/I_G ratio to higher values when moving from the inner side to the outer side of the wear track. This trend was less pronounced for the spheres. The scattering of the measurements on the counterbody could originate from the fact that the carbon material on the sphere is formed by transfer from the graphite-coated ring and hence, mixing might occur between carbon material from different regions. Additional measurements for more data points might be helpful to investigate this matter. The D band, however, was present for all samples and analyzed Raman spots, which proves a certain degree of disorder and the presence of six-fold aromatic rings according to Ferrari and Robertson [77].

Overall, the obtained G-band positions and intensity ratios can be compared to literature values, for example by Ferrari and Robertson [77]. The different bands correspond to different vibrational modes for the corresponding molecule and allow to make statements about the structure (e.g. crystallite size) and the chemical nature (clustering, sp^2 hybridization, disorder etc.). First we'll talk about the structural properties: The intensity ratio of I_D/I_G allows for the calculation of the crystallite size L_a according to the Tuinstra-Koenig-Relation [118]. Cançado et al. extended this equation for all Raman laser wavelengths λ_l in the following equation [119]. For the red laser used in this thesis λ_l corresponds to 633 nm.

$$L_a(nm) = (2.4 \times 10^{-10}) \times \lambda_l^4 \times \left(\frac{I_D}{I_G}\right)^{-1} \tag{5.2}$$

In Table 5.2 the crystallite sizes for all areas were calculated according to the Tuinstra-Koenig-Relation [118]. According to these calculations, the sizes for the graphite coating after rolling under high loads range between 15.6 and 36.8 nm, hence a nanocrystalline structure will prevail. Two effects can be observed, which are of course in line with the trend observed regarding the I_D/I_G ratio: the crystal size decreases from the

Table 5.2: G-band shifts and I_D/I_G ratio changes summarized over all SRR values for the two tribo-bodies and their dependency on the Raman measurement position.

SRR [%]	Crystallite Size Inside [nm]	Crystallite Size Middle [nm]	Crystallite Size Outside [nm]	Crystallite Size Iridescent [nm]
Ring 0	46.2	–	33.6	–
Ring 5	33.5	32.6	26.6	–
Ring 10	32.3	25.3	21.8	–
Ring 15	32.2	21.2	23.3	–
Sphere 0	13.5	–	38.92	–
Sphere 5	34.3	27.3	15.6	32.5
Sphere 10	27.4	20.9	16.3	34.5
Sphere 15	36.8	31.3	16.2	37.0

inside to the outside of the wear track for all samples and SRR. On the ring, a decrease in crystal size is observed when increasing the SRR. On the sphere however, the latter trend is not as clear, presumably due to it being a transfer film and thus more mixing of the material takes place. But what could be the reason for the areal size dependency? One hypothesis is a speed-dependence due to the geometry of the contact. As the sphere rotates around its own axis, the speed and thus the number of rollovers will vary depending on the position. At the very top of the sphere the speed will be higher than in the middle of it. Another possibility could be the pressure-distribution, which according to Hertz will of course be higher in the middle of the contact (presumably the inner side of the wear track) and lower further away from it. In addition, calculations by Stratmann et al. on roller bearings showed a clear areal variation of the SRR depending on the position [106]: close to the middle of the roller, the SRR will be small and nearly no sliding will occur. On the sides of the roller, however, the SRR will gradually increase. Their observations are in line with the results discussed in this chapter: on the inside of the wear track, a small local SRR will dominate and thus only small or no structural changes at all are expected. On the outside of the wear track, a higher SRR is expected which will lead to more structural changes in the graphite due to shear, similar to the sliding experiments. To test which of these factors contribute most to the nanocrystalline size distribution, additional MTM experiments would be needed at constant SRR but varying speed and varying normal force. Further TEM and EELS analyses of the thin carbon layer on different wear track positions might help support the hypothesis of only small structural changes in the middle of the sphere-flat contact and an increasing gradient of structural transition to t-C on the outer side of the contact.

It is important to mention that the Tuinstra-Koenig-Relation does not account for some characteristics of nano-crystalline graphite or amorphous carbon [77]. This means that the sizes could be different in reality, but the overall trends should remain the same. Nevertheless, according to Ferrari and Robertson for graphite (and thus small L_a) the I_D/I_G ratio will first increase with increasing disorder until a reversal point is

reached. At this point, the clusters decrease in number and become distorted and smaller. The G-peak however only relates to the relative motion of sp^2 hybridized carbon and thus I_D will decrease with respect to the D-band. Hence the TK-relation does not apply anymore and in amorphous carbon a higher D-peak indicates ordering instead of disorder like for graphite.[77]

Generally the Raman spectra depend on five things [77]:

- sp^2 phase clustering

- degree of bond disorder

- presence of sp^2 rings and chains

- the ratio of sp^2/sp^3

- excitation laser energy [119]

Due to the influence of the excitation laser energy on the peak position, height, and width [119] it is difficult to compare G-band positions and the I_D/I_G ratio values directly to other publications if measured at differing laser wavelength. However, Ferrari and Robertson put extensive work to compare samples of differing sp^2 ratio at different laser wavelength. In general, lower laser wavelength result in a G-band shift to lower values but increased I_D/I_G ratios [120].

The presence of the D' and D+G band prove again that the graphite gets disordered during rolling at high pressures. The intensities of these two peaks significantly increase from the inside to the outside of the wear track, which proves again that the outer region of the wear track is less effected by the wear process [32].

In the iridescent areas an average G-band position of $(1605\pm1)\,\mathrm{cm}^{-1}$ and $I_D/I_G = 1.14$ was measured. The presence of these peaks clearly validate the hypothesis of a thin, carbon-based tribofilm which is getting formed via transfer onto the counterbody. It might be possible that the development, built-up and continuous destruction of this tribofilm might lead to the steps observed in the frictional behavior (see Figure 5.1). In addition the tribofilm coverage might be different for the SRR parameter sets. For both hypothesis additional experiments would be needed with varying experimental duration to analyze the built-up of the tribofilm, ideally via Raman mapping for a more detailed view of the coverage.

In the HR-TEM images and EELS measurements (see Section 4.8.3) we have seen that a sliding motion leads to the formation of a thin carbon layer which exhibits a decreased sp^2 content in comparison to the initial state and the disorder increases especially at the sliding interface. As we've observed the same thin carbon layer in the rolling experiments at 5% SRR and higher, one would expect the following things:

- the structure of the layer after rolling is close to amorphous carbon

- a lot of disorder and defects will be present

- the sp^2 content will be close to 30%

According to Ferrari and Robertson graphite can transform into nanocrystalline or amorphous carbon, which can be divided into different stages [77]. Due to the previously discussed results under sliding and rolling it is likely that in the contact we'll observe either nanocrystalline graphite or amorphous carbon (a-C), hence the transition between those two is of most interest. During the transition from nanocrystalline graphite to a-C, more defects are introduced and distorted sixfold rings or rings of other order will prevail with a sp^3 content of max. 20%. Due the decreased amount of sliding and more rolling it might be possible that a smaller percentage of the sp^2-hybridized graphite is transferred into the sp^3 content than the 27% we observed at 1 GPa. These structural changes should lead to a shift to lower G-band positions for a-C. This correlates well to the G-band shift observed in our Raman experiments, hence we'll likely observe a-C on the inner side of the wear track and more nanocrystalline graphite on the outside. For a-C a higher amount of defects is observed, which would correlate to a increased I_D/I_G and hence smaller crystallite sizes compared to the nanocrystalline graphite on the outside of the wear track. Our Raman studies in Figure 5.5 and Table 5.2 show the opposite trend. How can this observation be explained?

One hypothesis was stated by Ferrari and Robertson, according to which at a certain crystallite size and amount of disorder the I_D/I_G trend is reversed. This is due to the fact that the G peak relates to bond stretching of sp^2 pairs, which will remain constant and hence the intensity will remain unchanged. I_D/I_G will hence decrease as the number of ordered rings decreases. It might be possible that we reached this inversal point for our graphite system and hence the trend is the opposite of one would observe. One way to test this hypothesis would be the preparation and analyses of (HR-) TEM lamella over the width of the wear track and consecutive EELS measurements to determine the cluster sizes and the sp^2 content. This would in addition give further insight into the total sp^2 content and whether they lay in the range of circa 20% as predicted by the Raman analyses.

As a last section of this discussion, it is important to validate if we do observe an SRR influence on the structure. It is observed that a SRR of 0% is not sufficient to built up the thin carbon layer in a sufficient quality or thickness to endure longer experiments, hence failure of the coating and wear took place. In the absence of any shear forces, no structural transformation to t-C is expected but only compression, as seen in the compression experiments in subsection 4.4.1. This explains their poor tribological behavior and the short lifetime of the MTM experiments under pure rolling, as the sliding experiments revealed the necessity of the t-C formation. If the SRR is increased to 5% and higher values, the thin carbon layer appears and t-C formation is expected, along with a thin tribofilm on the counterbody, which increases the coating's longevity drastically. In terms of the Raman experiments, no clear influence of the SRR on the G-band position and I_D/I_G became evident. Thus, the built-up, nature, and wear of the formed thin carbon layer as well as the iridescent tribofilm might be more crucial to explain the differences. Here again, additional electron microscopy and EELS analyses might shed some light onto this for experiments where the experimental duration was varied for shorter duration. However, the rolling analyses have clearly shown that

a thin carbon layer formation and thus presumably structural transformation occurs if the SRR is higher than 0%, as shear forces are needed for the transformation of graphite to t-C. Under pure rolling, no transformation occurs as the graphite coating only gets compressed. Hence, the results reported under sliding motion are valid for a wider range of motions, e.g. rolling.

6 Summary and Outlook

6.1 Summary

For the analysis of the graphite lubrication mechanisms under high mechanical load different experiments were conducted. First, microtribometer experiments in a linear-reversible sliding contact were used to investigate the influence of different parameters on the graphite lubrication mechanism: the graphite coating thickness, applied normal force, underlying substrate roughness, and the influence of humidity changes. The graphite coating yielded by the straight-forward airbrush deposition process exhibited a porous morphology and a degree of graphitization of 97%. Through extensive analysis with surface and chemical analysis of the samples, multiple important conclusions could be drawn. First and foremost, the material transport in the contact has proven to be limiting the longevity of the coating. In the first initial contact between counterbody and sphere, compression of the porous graphite layer occurs and graphite flakes adhere to the counterbody, forming a consistent graphite-graphite interface during sliding. The roughness asperities of the soft graphite are then worn away layer by layer, until delamination occurs, which at some point leads to starvation of the lubricant.

To tackle this matter, the adhesion-substrate roughness relationship was analyzed by an in-depth parameter study with varying substrate roughness states. In contrast to previous research, where an increased roughness led to higher friction, the correlation seems to be less straightforward. The results presented in this thesis have shown that an intermediate roughness of $S_\mathrm{a} = (70 \pm 1)\,\mathrm{nm}$ yielded an outstanding increase in coating lifetime and reduction of friction and counterbody wear. In these samples, the formation of a thin carbon layer in the sliding contact was observed. Its formation occurs already in the first initial cycles and the thickness of 30 to $150\,\mathrm{nm}$ suffices to prevent the contact of iron and steel surface asperities, which in turn would lead to cold welding and the creation of hard, abrasive particles. The formation of this thin carbon layer relies on the trapping of graphite material in polishing trenches of the ideal size and the right roughness peak to valley ratio. If valleys dominate the surface and the surface structures are abundant enough, graphite will prevail in the polishing trenches, act as lubricant reservoirs, and cover the roughness peaks sufficiently.

The thin carbon layer was then analyzed by high-resolution imaging methods for a detailed understanding of its structure. HR-TEM and EELS analysis revealed a sp^2 gradient with the lowest sp^2 hybridization measured at the sliding interface between graphite coating and counterbody transfer layer. This transformation of graphite to turbostratic carbon has so far been unknown unless in extreme environments like

ball milling. These novel results were thus summarized in a proposed new, extended graphite lubrication mechanism, which is valid under high and low loads. The experimental tribometric results were supported by molecular dynamic simulations conducted in the scope of the SPP2074 by Dr. Andreas Klemenz at the Fraunhofer IWM.

This proposed extended graphite lubrication model was additionally extended to explain the role of humidity. Here again, tribometric experiments and MD simulations were brought together and compared to gather a deep understanding. In the tribometric experiments an increase in humidity up to 24 % RH led to lower friction until a plateau of $\mu = 0.10$ was reached. MD simulations correlated this effect to the formation of a water film on the graphite surface. A critical water density is needed to saturate all surface defects. This density relates to the local pressure and thus may vary locally. At an asperity contact, the local pressure might increase drastically, thus the critical water density is not given and cold welding between the two graphite films occurs, leading to turbostratic carbon formation. At high relative humidity, extensive graphite coating wear takes place. In contrast to the literature, this effect is not (only) correlated to the formation of capillary necks between the two moving surfaces. Macroscopic amounts of water migrate in between the coating and substrate, hence forming a water film that accelerates the material transport.

In two smaller parameter studies, the tribological performance of solid lubrication graphite was investigated in dry environments, e.g. dry nitrogen and UHV. In nitrogen, a decrease in the longevity was observed, as reported by other researchers before. In an UHV environment, extensive wear was observed independently of the surrounding humidity content, as graphite suffered from dusting. Hence, the best friction reduction and a lifetime of the polycrystalline airbrush coating prevails under ambient conditions.

The thesis revealed the formation of a thin, turbostratic carbon layer, which is crucial for the good observed lubrication behavior. In a side study, the hypothesis was tested that similar results can be achieved by starting with amorphous carbon instead of graphite, which might get transformed as well. However, this hypothesis did not hold up as the softness of the amorphous carbon seems to be of utmost importance and extensive wear took place due to the hardness and roughness of the amorphous carbon coatings. Hence, it is crucial to start with a soft graphite coating on a substrate of industrial roughness to obtain the *in situ* formation of a thin, turbostratic carbon layer.

In the last part of the thesis, the coating was tested under a rolling motion for a better understanding and comparability of the wanted industrial application, a rolling bearing. Here, the so-called slide-to-roll ratio was varied to evaluate whether the thin carbon layer is also formed if less than pure sliding motion takes place. So far, no extensive studies on the performance of graphite solid lubricants under rolling motion were known to exist. The results presented in this thesis demonstrated the formation of the thin carbon layer for all slide-to-roll ratios higher than 0%. An increase in the sliding percentage increased the lifetime of the coating due to structural changes of the

graphite and a tribofilm was formed on the counterbody. The tribofilm presence was confirmed by Raman measurements and presumably, its formation and destruction control the tribological performance, as it varies for different slide-to-roll ratios. The results stressed the importance of structural changes of the graphite coating when exposed to shear forces for its good tribological performance.

The novel and surprising results presented in this thesis allow a more fundamental understanding of the graphite lubrication mechanisms under high mechanical load. The experiments revealed a so far unreported transformation of graphite to turbostratic carbon in sliding contacts with a clear, declining sp^2 hybridization gradient towards the sliding interface. The results thus closed a gap in research of graphite lubrication mechanism and added another puzzle piece to it. As seen by the rolling experiments the easy and cost-effective airbrush coating process yielded a soft, porous graphite coating which is suitable for high load applications both under sliding and rolling motion.

6.2 Outlook

Based on the research presented in this thesis, additional research is needed in some areas. As seen in both sliding and rolling experiments, the longevity of the coating is limited due to the coating-substrate adhesion being in need of improvement. The most promising way to do so by mixing the graphite particles with a binder material such as clay, polymer, or resin. Through careful tuning of the mixing ratio, a sacrificial element can be achieved with the ideal softness to ensure material transfer onto the rolling bodies and/or the cage of a bearing. The transfer layer formation will depend on the binder material as well as the applied normal force. Hence, a detailed parameter study will help shine a light on the nature, formation, and wear of the transfer layer and how to tailor it to the desired goals. The SPP2074 project on this matter will be continued in a next project phase of three years, where these research points will be investigated in detail.

The rolling experiments and consecutive Raman studies revealed a crucial tribofilm formation on the counterbodies. To work towards the goal of an ideally lifetime-lubricated rolling bearing with graphite as a solid lubricant, a better understanding is needed. Additional experiments with varying duration paired with Raman mapping would enable a better understanding of the stepwise tribofilm formation and how its coverage influences friction and wear. Furthermore, detailed TEM and EELS analyses of the formed thin carbon layer might prove the transition of graphite to t-C in rolling contacts. In addition, they would allow the investigation of an expected gradient in the t-C formation from the inside of the sphere-flat contact to the outer side, where higher SRR values are expected.

Bibliography

[1] I. Hutchings and P. Shipway. "Preface to the second edition". In: *Tribology (Second Edition)*. Ed. by I. Hutchings and P. Shipway. Second Edition. Butterworth-Heinemann, 2017, p. ix.

[2] B. Bhushan. *Principles and Applications to Tribology*. The Atrium, Southern Gate, Chichester, West Sussex, PO19 8SQ, UK: John Wiley & Sons, Ltd, 2013.

[3] K. Holmberg and A. Erdemir. "Influence of tribology on global energy consumption, costs and emissions". In: *Friction* 5.3 (2017), pp. 263–284.

[4] M. Woydt et al. *Tribologie in Deutschland*. Jülich, Germany: Gesellschaft für Tribologie e.V., 2019.

[5] B. für Forschung und Technologie. *Damit Rost und Verschleiß nicht Milliarden fressen*. Bonn, Germany: BMFT-Report, Referat Presse und Öffentlichkeitsarbeit, 1983.

[6] T. W. Scharf and S. V. Prasad. "Solid lubricants: a review". In: *Journal of Materials Science* 48.2 (2013), pp. 511–531.

[7] H. E. Sliney. *Solid Lubricants*. NASA Technical Memorandum 103803. NASA, Cleveland, Ohio, USA, 1991.

[8] D. G. Beate Bender. *Dubbel Taschenbuch für den Maschinenbau 1: Grundlagen und Tabellen*. 26th ed. Heidelberg: Springer Vieweg Berlin, 2020.

[9] I. L. Singer, ed. *Fundamentals of friction. Macroscopic and microscopic processes ; [proceedings of the NATO Advanced Study Institute on Fundamentals of Friction, Braunlage, Harz, Germany, July 29 - August 9, 1991*. eng. Vol. 220. NATO ASI series Series E, Applied sciences. Singer, Irwin L. (Hrsg.) Dordrecht: Kluwer Academic Publishers, 1992. 621 pp.

[10] Nils Wiberg. "Lehrbuch der Anorganischen Chemie". In: *Lehrbuch der Anorganischen Chemie*. Ed. by N. Wiberg et al. De Gruyter, 2008.

[11] P. Ruz et al. "Structural evolution of turbostratic carbon: Implications in H2 storage". In: *Solid State Sciences* 62 (2016), pp. 105–111.

[12] N. Kumar et al. "Load dependent friction coefficient of crystalline graphite and anomalous behavior of wear dimension". In: *Tribology International* 88 (2015), pp. 280–289.

[13] M. A. Pimenta et al. "Studying disorder in graphite-based systems by Raman spectroscopy". In: *Physical chemistry chemical physics : PCCP* 9.11 (2007), pp. 1276–1291.

[14] M. Antisari et al. "Low energy pure shear milling: A method for the preparation of graphite nano-sheets". In: *Scripta Materialia* 55.11 (2006), pp. 1047–1050.

[15] Z. Q. Li et al. "X-ray diffraction patterns of graphite and turbostratic carbon". In: *Carbon* 45.8 (2007), pp. 1686–1695.

[16] Z. Q. Li and Y. Zhou. "Structural evolution of a graphite–diamond mixture during ball milling". In: *Physica B: Condensed Matter* 405.3 (2010), pp. 1004–1010.

[17] A. V. Mokhov et al. "Identification of sp2 Carbon in Lunar Material from the Sample Delivered by the Luna 24 Automatic Station". In: *Doklady Earth Sciences* 485.2 (2019), pp. 418–421.

[18] W. H. Bragg. *An introduction to crystal analysis.* G. Bell and Sons, Ltd., London, 1928.

[19] R. M. Mortier, M. F. Fox, and S. T. Orszulik. *Chemistry and Technology of Lubricants.* SpringerLink: Springer e-Books. Dordrecht: Springer Netherlands, 2010. Online-Ressource.

[20] B. K. Yen, B. E. Schwickert, and M. F. Toney. "Origin of low-friction behavior in graphite investigated by surface x-ray diffraction". In: *Applied Physics Letters* 84.23 (2004), pp. 4702–4704.

[21] Bowden, F. P. and Young, J. E. "Friction of diamond, graphite, and carbon and the influence of surface films". In: *Proc. R. Soc. Lond. A* 1951.208 (1951), pp. 444–455.

[22] R. M. Baker. "Sliding contacts- electrical characteristics". In: *Transactions of the American Institute of Electrical Engineers* 55.1 (1936), pp. 94–100.

[23] R. H. Savage. "Graphite Lubrication". In: *Journal of Applied Physics* 19.1 (1948), pp. 1–10.

[24] R. Holm. *Electric Contacts: Theory and Application.* Berlin, Heidelberg: Springer Berlin Heidelberg and Springer, 1967, pp. 251–259.

[25] G.W Rowe. "Some observations on the frictional behaviour of boron nitride and of graphite". In: *Wear* 3.4 (1960), pp. 274–285.

[26] R. Arnell and D. Teer. "Lattice Parameters of Graphite in relation to Friction and Wear". In: *Nature* 218 (1968), pp. 1155–1156.

[27] J. Skinner, N. Gane, and D. Tabor. "Micro-friction of Graphite". In: *Nature Physical Science* 232 (1971), pp. 195–196.

[28] C. E. Morstein et al. "Humidity-dependent lubrication of highly loaded contacts by graphite and a structural transition to turbostratic carbon". In: *Nature communications* 13.1 (2022), p. 5958.

[29] J. K. Lancaster and J. R. Pritchard. "The influence of environment and pressure on the transition to dusting wear of graphite". In: *Journal of Physics D: Applied Physics* 14.4 (1981), pp. 747–762.

[30] Paolo Restuccia, Mauro Ferrario, and M.C. Righi. "Monitoring water and oxygen splitting at graphene edges and folds: Insights into the lubricity of graphitic materials". In: *Carbon* 156 (2020), pp. 93–103.

[31] J. D. Schall, G. Gao, and J. A. Harrison. "Effects of Adhesion and Transfer Film Formation on the Tribology of Self-Mated DLC Contacts". In: *The Journal of Physical Chemistry C* 114.12 (2010), pp. 5321–5330.

[32] D. Berman, A. Erdemir, and A. V. Sumant. "Few layer graphene to reduce wear and friction on sliding steel surfaces". In: *Carbon* 54 (2013), pp. 454–459.

[33] M. Dienwiebel et al. "Superlubricity of graphite". In: *Physical review letters* 92.12 (2004), p. 126101.

[34] F. Bonelli et al. "Atomistic simulations of the sliding friction of graphene flakes". In: *The European Physical Journal B* 70 (2009), pp. 449–459.

[35] A. P. Merkle and L. D. Marks. "Friction in full view". In: *Applied Physics Letters* 90.6 (2007), p. 064101.

[36] J. Li, X. Ge, and J. Luo. "Random occurrence of macroscale superlubricity of graphite enabled by tribo-transfer of multilayer graphene nanoflakes". In: *Carbon* 138 (2018), pp. 154–160.

[37] W. Bollmann and J. Spreadborough. "Action of Graphite as a Lubricant". In: *Nature* 186.4718 (1960), pp. 29–30.

[38] G. S. Verhoeven, M. Dienwiebel, and J. W. M. Frenken. "Model calculations of superlubricity of graphite". In: *Physical Review B* 70.16 (2004).

[39] M. Dienwiebel et al. "Model experiments of superlubricity of graphite". In: *Surface Science* 576.1-3 (2005), pp. 197–211.

[40] M. M. van Wijk et al. "Superlubric to stick-slip sliding of incommensurate graphene flakes on graphite". In: *Physical Review B* 88.23 (2013).

[41] A. Klemenz et al. "Atomic scale mechanisms of friction reduction and wear protection by graphene". In: *Nano letters* 14.12 (2014), pp. 7145–7152.

[42] C. M. Mate et al. "Atomic-scale friction of a tungsten tip on a graphite surface". In: *Phys. Rev. Lett.* 59.17 (1987), pp. 1942–1945.

[43] R. Buzio et al. "Friction force microscopy investigation of nanostructured carbon films". In: *Carbon* 40.6 (2002), pp. 883–890.

[44] D. Marchetto et al. "Friction and Wear on Single-Layer Epitaxial Graphene in Multi-Asperity Contacts". In: *Tribology Letters* 48.1 (2012), pp. 77–82.

[45] F. Wählisch et al. "Friction and atomic-layer-scale wear of graphitic lubricants on SiC(0001) in dry sliding". In: *Wear* 300.1-2 (2013), pp. 78–81.

[46] D. Marchetto, T. Feser, and M. Dienwiebel. "Microscale study of frictional properties of graphene in ultra high vacuum". In: *Friction* 3.2 (2015), pp. 161–169.

[47] Y. Huang et al. "Wear evolution of monolayer graphene at the macroscale". In: *Carbon* 115 (2017), pp. 600–607.

[48] C. Lee et al. "Frictional characteristics of atomically thin sheets". In: *Science (New York, N.Y.)* 328.5974 (2010), pp. 76–80.

[49] S. Li et al. "The evolving quality of frictional contact with graphene". In: *Nature* 539.7630 (2016), pp. 541–545.

[50] T. Filleter et al. "Friction and dissipation in epitaxial graphene films". In: *Physical review letters* 102.8 (2009), p. 086102.

[51] J. Qi et al. "Film thickness effects on mechanical and tribological properties of nitrogenated diamond-like carbon films". In: *Surface and Coatings Technology* 145.1 (2001), pp. 38–43.

[52] G. T. Gao, P. T. Mikulski, and J. A. Harrison. "Molecular-scale tribology of amorphous carbon coatings: effects of film thickness, adhesion, and long-range interactions". In: *Journal of the American Chemical Society* 124.24 (2002), pp. 7202–7209.

[53] X. Shi et al. "Tribological performance of graphite-like carbon films with varied thickness". In: *Tribology International* 149 (2020), p. 105586.

[54] D. Berman, A. Erdemir, and A. V. Sumant. "Reduced wear and friction enabled by graphene layers on sliding steel surfaces in dry nitrogen". In: *Carbon* 59 (2013), pp. 167–175.

[55] D. Berman et al. "Extraordinary Macroscale Wear Resistance of One Atom Thick Graphene Layer". In: *Advanced Functional Materials* 24.42 (2014), pp. 6640–6646.

[56] D. Berman, A. Erdemir, and A. V. Sumant. "Graphene: a new emerging lubricant". In: *Materials Today* 17.1 (2014), pp. 31–42.

[57] D. Marchetto et al. "Surface passivation by graphene in the lubrication of iron: A comparison with bronze". In: *Carbon* 116 (2017), pp. 375–380.

[58] V. R. S. Shaji. "An investigation on surface grinding using graphite as lubricant". In: *International Journal of Machine Tools & Manufacture* 42.6 (2002), pp. 733–740.

[59] P. Fasihi et al. "Effect of graphite and MoS2 based solid lubricants for application at wheel-rail interface on the wear mechanism and surface morphology of hypereutectoid rails". In: *Tribology International* 157 (2021), p. 106886.

[60] H. Torres et al. "Compatibility of graphite, hBN and graphene with self-lubricating coatings and tool steel for high temperature aluminium forming". In: *Wear* 490-491 (2022), p. 204187.

[61] L. Reinert et al. "Influence of Surface Roughness on the Lubrication Effect of Carbon Nanoparticle-Coated Steel Surfaces". In: *Tribology Letters* 66.1 (2018), p. 221.

[62] B. S. Waldemar Steinhilper, ed. *Konstruktionselemente des Maschinenbaus 2. Grundlagen von Maschinenelementen für Antriebsaufgaben.* 7th ed. Heidelberg: Springer Berlin, 2012.

[63] S. Sharma et al. "Graphite particles reinforced ZA-27 alloy composite materials for journal bearing applications". In: *Wear* 219.2 (1998), pp. 162–168.

[64] *SKF high temperature bearings and units.* 2022. URL: https://www.skf.com/my/industries/food-and-beverage/products-and-solutions/high-temperature-bearings-and-units (visited on 11/23/2022).

[65] *GGT Gleitlager AG: Graphitlager: Gleitlager aus Kohlenstoff.* 2023. URL: https://gleitlager.ch/de/produkte/gleitlager/gleitlager-aus-kohlenstoff (visited on 02/25/2023).

[66] *GGT Gleitlager AG: MBW-Gleitlager und Gleitelemente.* 2023. URL: https://gleitlager.ch/de/produkte/gleitlager/mbw-gleitlager (visited on 02/25/2023).

[67] F. P. Bowden and D. Tabor. *The Friction and Lubrication of Solids.* International series of monographs on physics. Clarendon Press, 2001.

[68] M. Scherge and S. Gorb. *Biological Micro- and Nanotribology: Nature's Solutions.* Berlin: Springer Science & Business Media, 2001.

[69] *LOG210 PDF - data logger with display for temperature and humidity - Dostmann.* URL: https://dostmann-electronic.de/product/log210-pdf-data-logger-with-display-for-temperature-and-humidity.html (visited on 01/07/2022).

[70] PCS Instruments, ed. *MTM2 Operation Manual.* London, 2009.

[71] B. J. Griffin. "A comparison of conventional Everhart-Thornley style and in-lens secondary electron detectors—a further variable in scanning electron microscopy". In: *Scanning* 33.3 (2011), pp. 162–173.

[72] R. Brydson. *Electron Energy Loss Spectroscopy.* 1st ed. London: Garland Science, 2001.

[73] R. F. Egerton. "Electron energy-loss spectroscopy in the TEM". In: *Reports on Progress in Physics* 72.1 (2009), p. 016502.

[74] F. Mangolini et al. "Quantification of the carbon bonding state in amorphous carbon materials: A comparison between EELS and NEXAFS measurements". In: *Carbon* 173 (2021), pp. 557–564.

[75] X. Zhang et al. "Practical aspects of the quantification of sp2-hybridized carbon atoms in diamond-like carbon by electron energy loss spectroscopy". In: *Carbon* 102 (2016), pp. 198–207.

[76] I. Tilinin, A. Jablonski, and W. Werner. "Quantitative surface analysis by Auger and x-ray photoelectron spectroscopy". In: *Progress in Surface Science* 52.4 (1996), pp. 193–335.

[77] A. C. Ferrari and J. Robertson. "Interpretation of Raman spectra of disordered and amorphous carbon". In: *Physical Review B* 61.20 (2000).

[78] A. Joerger et al. "A numerical approach for the determination of graphite deformation behaviour by using microtribological pressure tests". In: *Wear* 476 (2021). 23rd International Conference on Wear of Materials, p. 203652.

[79] C. Morstein and M. Dienwiebel. "Graphite lubrication mechanisms under high mechanical load". In: *Wear* 477 (2021). 23rd International Conference on Wear of Materials, p. 203794.

[80] H. Dogan, F. Findik, and O. Morgul. "Friction and wear behaviour of implanted AISI 316L SS and comparison with a substrate". In: *Materials & Design* 23.7 (2002), pp. 605–610.

[81] L. Reinert et al. "Long-lasting solid lubrication by CNT-coated patterned surfaces". In: *Scientific reports* 7.1 (2017), p. 42873.

[82] S. Bhowmick, A. Banerji, and A. T. Alpas. "Role of humidity in reducing sliding friction of multilayered graphene". In: *Carbon* 87 (2015), pp. 374–384.

[83] F. Pape and G. Poll. "Investigations on Graphene Platelets as Dry Lubricant and as Grease Additive for Sliding Contacts and Rolling Bearing Application". In: *Lubricants* 8.1 (2020), p. 3.

[84] S. K. Ghosh et al. "The Effects of PTFE Thickness on the Tribological Behavior of Thick PDA/PTFE Coatings". In: *Tribology Transactions* 63.3 (2020), pp. 575–584.

[85] B. Huang, Q. Zhou, and E.-g. Zhang. "Effect of Thickness on Tribological Behavior of Hydrogen Free Diamond-like Carbon Coating". In: *Coatings* 10.3 (2020), p. 243.

[86] K. Holmberg, H. Ronkainen, and A. Matthews. "Tribology of thin coatings". In: *Ceramics International* 26.7 (2000), pp. 787–795.

[87] F. P. Bowden, A. J. W. Moore, and D. Tabor. "The Ploughing and Adhesion of Sliding Metals". en. In: *Journal of Applied Physics* 14.2 (1943), pp. 80–91.

[88] K.-S. Kim et al. "Chemical vapor deposition-grown graphene: the thinnest solid lubricant". In: *ACS nano* 5.6 (2011), pp. 5107–5114.

[89] Deutsches Institut für Normung e.V., ed. *Geometrische Produktspezifikation (GPS)_- Oberflächenbeschaffenheit: Flächenhaft_- Teil_2: Begriffe und Oberflächen-Kenngrößen (ISO_25178-2:2012); Deutsche Fassung EN_ISO_25178-2:2012.* Geometrische Produktspezifikation. Berlin: Beuth Verlag GmbH, Sept. 1, 2012.

[90] A. Hirata, M. Igarashi, and T. Kaito. "Study on solid lubricant properties of carbon onions produced by heat treatment of diamond clusters or particles". In: *Tribology International* 37.11 (2004). Novel Carbons in Tribolgy, pp. 899–905.

[91] J. Takadoum and H. H. Bennani. "Influence of substrate roughness and coating thickness on adhesion, friction and wear of TiN films". In: *Surface and Coatings Technology* 96.2 (1997), pp. 272–282.

[92]   F. Svahn, Å. Kassman-Rudolphi, and E. Wallén. "The influence of surface roughness on friction and wear of machine element coatings". In: *Wear* 254.11 (2003). Papers presented at the 10th Nordic Conference on Tribology, NORDTRIB 2002, pp. 1092–1098.

[93]   L. Xiaowei et al. "The influence of roughness on tribological properties of nuclear grade graphite". In: *Journal of Nuclear Materials* 350.1 (2006), pp. 74–82.

[94]   D. H. Buckley and R. L. Johnson. "Mechanism of Lubrication for Solid Carbon Materials in Vacuum to 10 −9 Millimeter of Mercury". In: *ASLE Transactions* 7.1 (1964), pp. 91–100.

[95]   T. MacLucas et al. "Multiwall Carbon Nanotubes for Solid Lubrication of Highly Loaded Contacts". In: *ACS Applied Nano Materials* 6.3 (2023), pp. 1755–1769.

[96]   N. Kumar et al. "Super low to high friction of turbostratic graphite under various atmospheric test conditions". In: *Tribology International* 44.12 (2011), pp. 1969–1978.

[97]   J. Spreadborough. "The Frictional Behaviour of Graphite". In: *Wear* 5 (1961), pp. 18–30.

[98]   T. Arif, G. Colas, and T. Filleter. "Effect of Humidity and Water Intercalation on the Tribological Behavior of Graphene and Graphene Oxide". In: *ACS applied materials & interfaces* 10.26 (2018), pp. 22537–22544.

[99]   T. Arif et al. "Role of chemical vs. physical interfacial interaction and adsorbed water on the tribology of ultrathin 2D-material/steel interfaces". In: *Tribology International* 163 (2021), p. 107194.

[100] H.-J. Butt and M. Kappl. *Surface And Interfacial Forces, 2nd ed.* Weinheim, Germany: Wiley-VCH, 2018.

[101] A. Kozbial et al. "Characterization of the intrinsic water wettability of graphite using contact angle measurements: Effect of defects on static and dynamic contact angles". In: *Langmuir* 33.4 (2017), pp. 959–967.

[102] B. K. Yen. "Influence of water vapor and oxygen on the tribology of carbon materials with sp2 valence configuration". In: *Wear* 192.1-2 (1996), pp. 208–215.

[103] H. Zaidi, F. Robert, and D. Paulmier. "Influence of adsorbed gases on the surface energy of graphite: consequences on the friction behaviour". In: *Thin Solid Films* 264.1 (1995), pp. 46–51.

[104] B. Schultrich. *Tetrahedrally Bonded Amorphous Carbon Films I. Basics, Structure and Preparation.* Vol. 263. Springer Series in Materials Science. Schultrich, Bernd (VerfasserIn). Berlin, Heidelberg: Springer Berlin Heidelberg and Springer, 2018. 752 pp.

[105] J. Jiang and R. Arnell. "The effect of substrate surface roughness on the wear of DLC coatings". In: *Wear* 239.1 (2000), pp. 1–9.

[106] A. Stratmann et al. "Antiwear tribofilm growth in rolling bearings under boundary lubrication conditions". In: *Tribology International* 113 (2017), pp. 43–49.

[107] E. Hecht. *Optics.* 5th ed. Hecht, Eugene, (author.) Boston: Pearson Education Inc, 2017. 714 pages.

[108] D. P. Dowling et al. "The use of refractive index as a measure of diamond-like carbon film quality". In: *Diamond and Related Materials* 7.2-5 (1998), pp. 432–434.

[109] Y. Kawashima and G. Katagiri. "Fundamentals, overtones, and combinations in the Raman spectrum of graphite". In: *Phys. Rev. B* 52 (14 Oct. 1995), pp. 10053–10059.

[110] T. Livneh, T. L. Haslett, and M. Moskovits. "Distinguishing disorder-induced bands from allowed Raman bands in graphite". In: *Phys. Rev. B* 66 (19 Nov. 2002), p. 195110.

[111] D. L. A. de Faria, S. Venâncio Silva, and M. T. de Oliveira. "Raman microspectroscopy of some iron oxides and oxyhydroxides". In: *Journal of Raman Spectroscopy* 28.11 (1997), pp. 873–878.

[112] J. Lin, L. Wang, and G. Chen. "Modification of Graphene Platelets and their Tribological Properties as a Lubricant Additive". In: *Tribology Letters* 41.1 (2011), pp. 209–215.

[113] J. Zhao et al. "Friction-induced nano-structural evolution of graphene as a lubrication additive". In: *Applied Surface Science* 434 (2018), pp. 21–27.

[114] J. Wang et al. "Tribological characteristics of graphene as grease additive under different contact forms". In: *Tribology International* 127 (2018), pp. 457–469.

[115] F. Deuerler et al. "Pretreatment of substrate surface for improved adhesion of diamond films on hard metal cutting tools". In: *Diamond and Related Materials* 5.12 (1996), pp. 1478–1489.

[116] S. J. Bull. "Techniques for improving thin film adhesion". In: *Vacuum* 43.5-7 (1992), pp. 517–520.

[117] P. J. Blau and J. K. Gardner. "Tribological characteristics of graded pencil cores on paper". In: *Wear* 197.1-2 (1996), pp. 233–241.

[118] F. Tuinstra and J. L. Koenig. "Raman Spectrum of Graphite". In: *The Journal of Chemical Physics* 53.3 (1970), pp. 1126–1130.

[119] L. G. Cançado et al. "General equation for the determination of the crystallite size La of nanographite by Raman spectroscopy". In: *Applied Physics Letters* 88.16 (2006), p. 163106.

[120] A. C. Ferrari and J. Robertson. "Resonant Raman spectroscopy of disordered, amorphous, and diamondlike carbon". In: *Physical Review B* 64.7 (2001), p. 199.

List of Abbreviations

a-C	amorphous carbon
AFM	atomic force microscope
BF	bright field
CoF	coefficient of friction
DLC	diamond-like carbon
EDXS	energy dispersive X-ray spectroscopy
EELS	electron energy loss spectroscopy
ETD	Everhardt-Thornley-detector
FFT	fast Fourier transform
FIB	focused ion beam
FWHM	full width at half maximum
HR	high resolution
MD	molecular dynamic
ML	mirror-like
MS	mass spectrometer
MTM	mini traction machine
PTFE	Polytetrafluoroethylene
PVD	physical vapour deposition
RH	relative humidity
ROI	region of interest
SE	secondary electrons
SEM	scanning electron microscope
SRR	slide-to-roll ratio
STEM	scanning transmission electron microscope
t-C	turbostratic carbon
TEM	transmission electron microscope
TK	Tuinstra-Koenig
UHV	ultra high vacuum
WLI	white light interferometry
XPS	X-ray photoelectron spectroscopy
XRD	X-ray diffraction

List of Figures

Appendix

Project Number	Project Topic	Involved Research Institutions
1	Mechanismen der Graphitschmierung in Wälzkontakten	KIT Angewandte Materialien – Zuverlässigkeit und Mikrostruktur IAM-ZM Fraunhofer Institut für Werkstoffmechanik IWM KIT Institut für Produktentwicklung IPEK
2	Trockenschmierung von Wälzkontakten durch selbstregenerative Molybdänoxidschichtsysteme	Institut für Maschinenkonstruktion und Tribologie (IMKT) Institut für Umformtechnik und Umformmaschinen (IFUM) Institut für Werkstoffkunde (IW) - Leibniz Universität Hannover
3	Fluidfrei geschmierte Stirnradverzahnung – tribologische Analyse und konstruktive Auslegung	Forschungsstelle für Zahnräder und Getriebebau (FZG), Technische Universität München Institut für Oberflächentechnik (IOT), RWTH Aachen University
4	Fluidfreie Schmierstoffschichten für den hochbelasteten und unsynchronisierten Betrieb von trockenlaufenden Schraubenmaschinen	Technische Universität Dortmund - Fachgebiet Fluidtechnik (Ft) Lehrstuhl für Werkstofftechnologie (LWT) Experimentelle Physik 2 (E2)
5	Polytetrafluorethylen (PTFE)-Schmierung in hochbelasteten Wälzkontakten	Institut für Maschinenelemente und Systementwicklung der RWTH Aachen (MSE) Fraunhofer-Institut für Werkstoffmechanik IWM, Freiburg
6	Tribologische Transfermechanismen und großflächige Mikrokontaktsimulation der Festschmierstoffbereitstellung aus PVD-Schichten für trockenlaufende Zahnradstufen	Werkzeugmaschinenlabor (WZL) der RWTH Aachen Leibniz-Institut für Werkstofforientierte Technologien - IWT
7	Fluidfreie Schmiersysteme für mechanisch hoch belastete Linearführungen durch beschichtungstechnische Optimierung der Funktionselemente	Fraunhofer IST Braunschweig Hochschule Mannheim, Kompetenzzentrum für Tribologie
8	Feststoffschmierung durch Kohlenstoffnanoröhren: Grundlegendes Verständnis der Transferschichtbildung und der Gleitmechanismen durch Atomistik und experimentelle Nanoanalytik	Fraunhofer IWM, Freiburg Universität des Saarlandes, Saarbrücken
9	Fluidfreie Schmierung von Schneckengetrieben auf Basis von PTFE	Leibniz-Institut für Polymerforschung Dresden e. V. (IPF) Institut für Oberflächen- und Schichtanalytik GmbH (IFOS), Kaiserslautern Lehrstuhl für Maschinenelemente und Getriebetechnik (MEGT) TU Kaiserslautern
10	Mechanismenbasierte Aufklärung des Transfers kunststoffgebundener fluidfreier Schmierstoffsysteme im Schmierstoffkörper-Grundkörper-Kontakt und dessen Einfluss auf die tribologischen Eigenschaften im hochbelasteten Grundkörper-Gegenkörper-Kontakt	Lehrstuhl für Verbundwerkstoffe (CCe) TU Kaiserslautern Institut für Oberflächen-und Schichtanalytik GmbH (IFOS), Kaiserslautern
11	Grundlagen für eine verbesserte Gebrauchsdauerberechnung feststoffgeschmierter Wälzlager durch Multiskalen-Untersuchungen	Friedrich-Alexander-Universität Erlangen-Nürnberg: Lehrstuhl für Konstruktionstechnik (KTmfk) Lehrstuhl für Allgemeine Werkstoffeigenschaften (WW1) / Computer-Chemie-Centrum (CCC)
12	Einfluss von Transfer- und Transformationsprozessen auf die Gebrauchsdauer von feststoffgeschmierten Wälzlagern	Institut für Oberflächen- und Schichtanalytik (IFOS) Lehrstuhl für Maschinenelemente u. Getriebetechnik (MEGT) TU Kaiserslautern

Figure A.1: Overview of the different SPP2074 projects and the involved institutions.

Table A.1: Lifetime and the steady-state CoF derived from microtribometer experiments at $1\,\mathrm{GPa}$ and $\leq 5\,\%\,\mathrm{RH}$ with substrates of varying roughness, see Section 4.7.3.

End SiC Grain Size	Steady-State CoF	Lifetime [cycles]
P320	0.18 ± 0.01	275 ± 65
P600	0.15 ± 0.02	115 ± 13
P1200	0.13 ± 0.00	1451 ± 398
P2500	0.15 ± 0.01	386 ± 88
P4000	0.16 ± 0.00	90 ± 20
ML	0.15 ± 0.00	238 ± 40
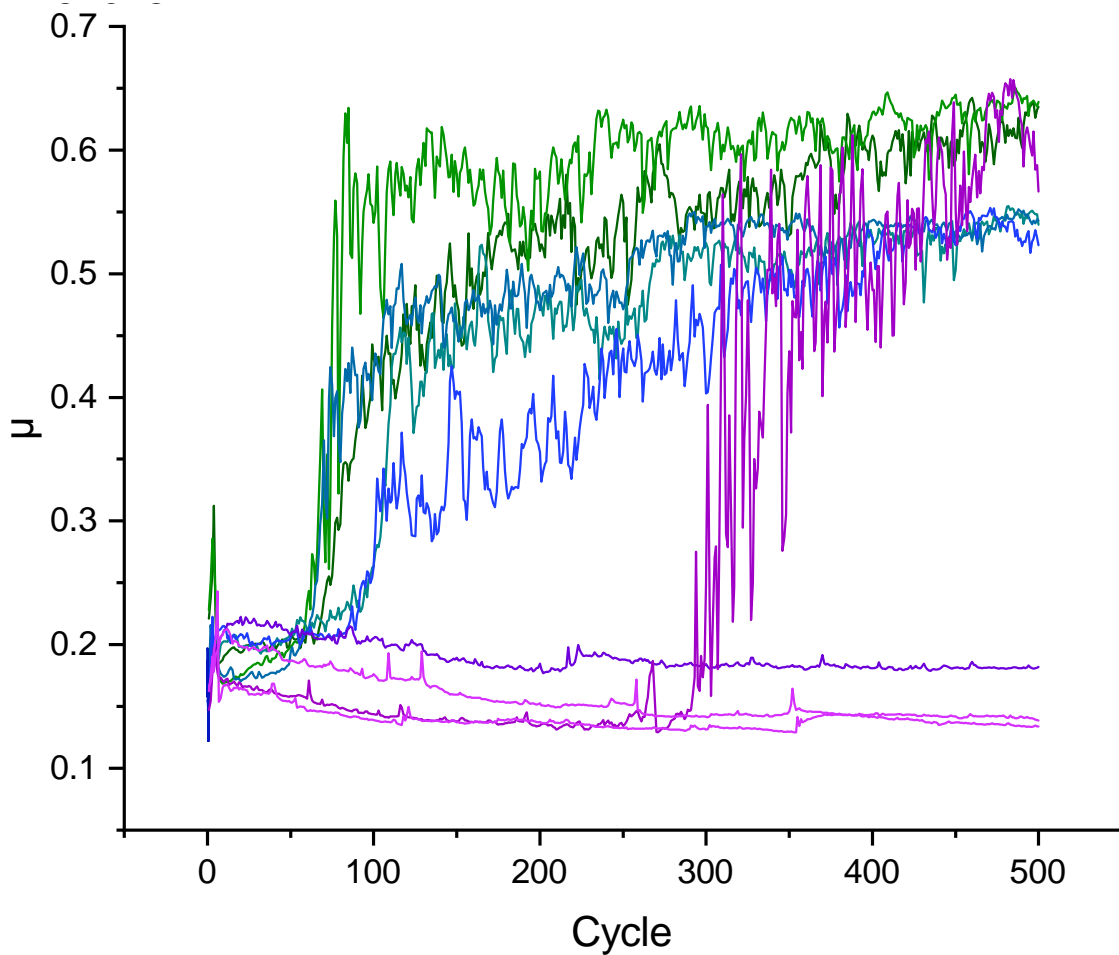
Figure A.2: CoF during the microtribometer experiments with a P320 graphite-coated iron substrate at $1\,\mathrm{GPa}$ and $\leq 5\,\%\,\mathrm{RH}$, see Section 4.7.3.
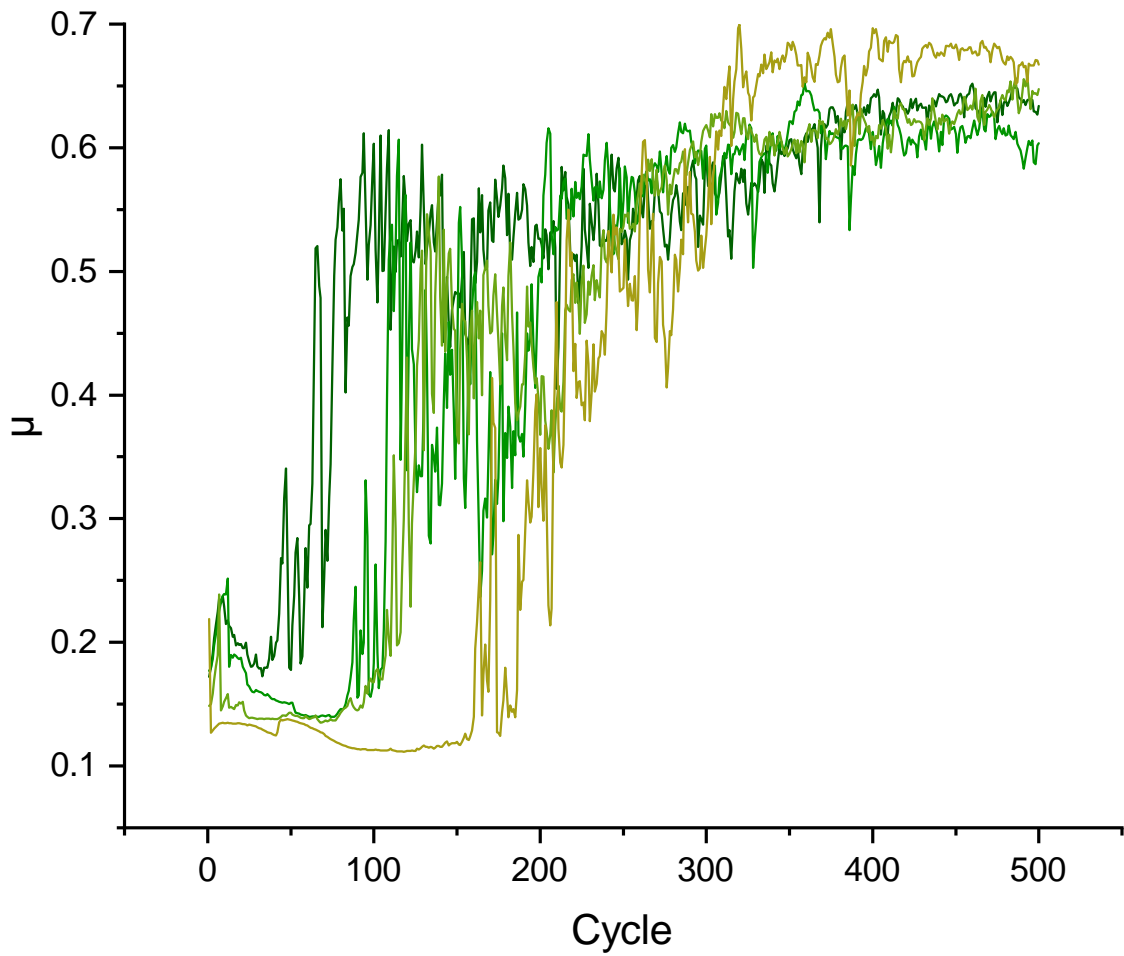
Figure A.3: CoF during the microtribometer experiments with a P600 graphite-coated iron substrate at $1\,\mathrm{GPa}$ and $\leq 5\,\%\,\mathrm{RH}$, see Section 4.7.3.
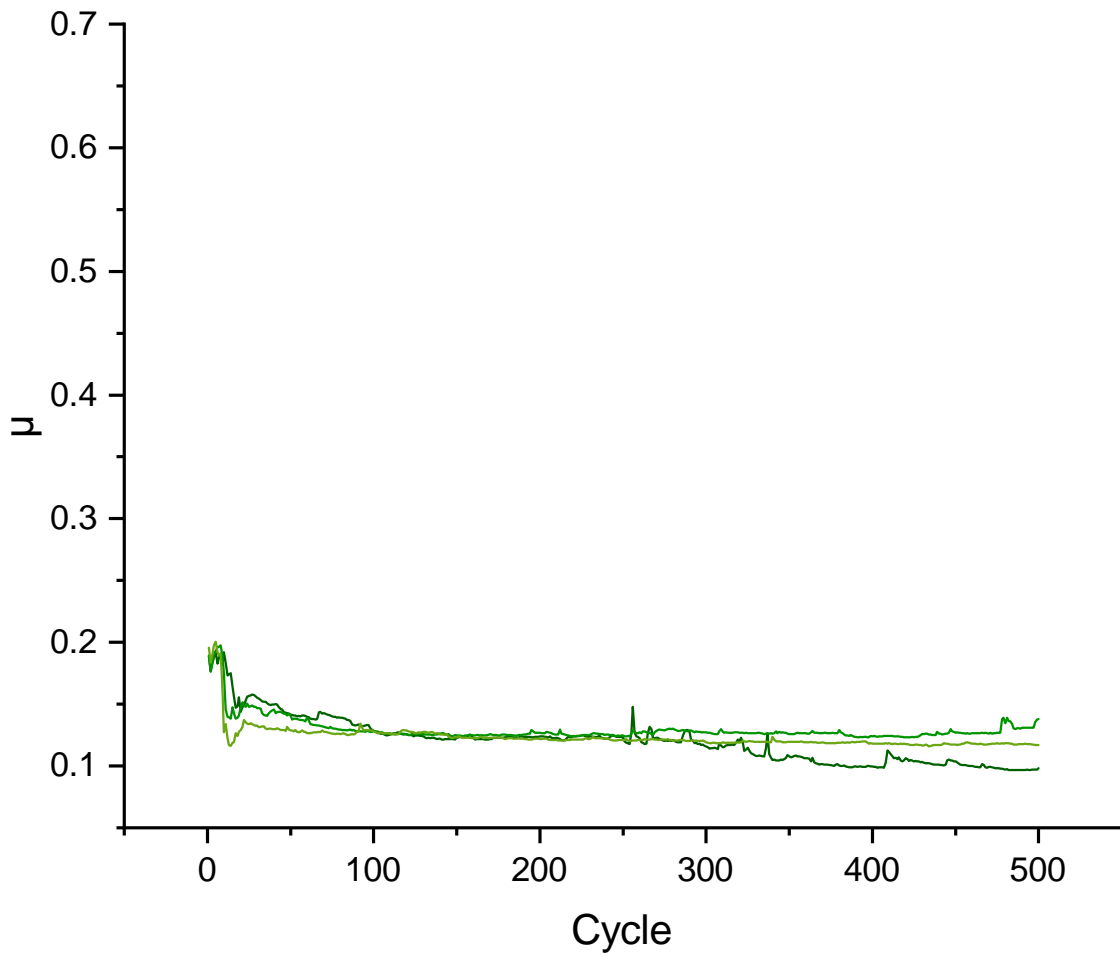
Figure A.4: CoF during the microtribometer experiments with a P1200 graphite-coated iron substrate at $1\,\mathrm{GPa}$ and $\leq 5\,\%\,\mathrm{RH}$, see Section 4.7.3.
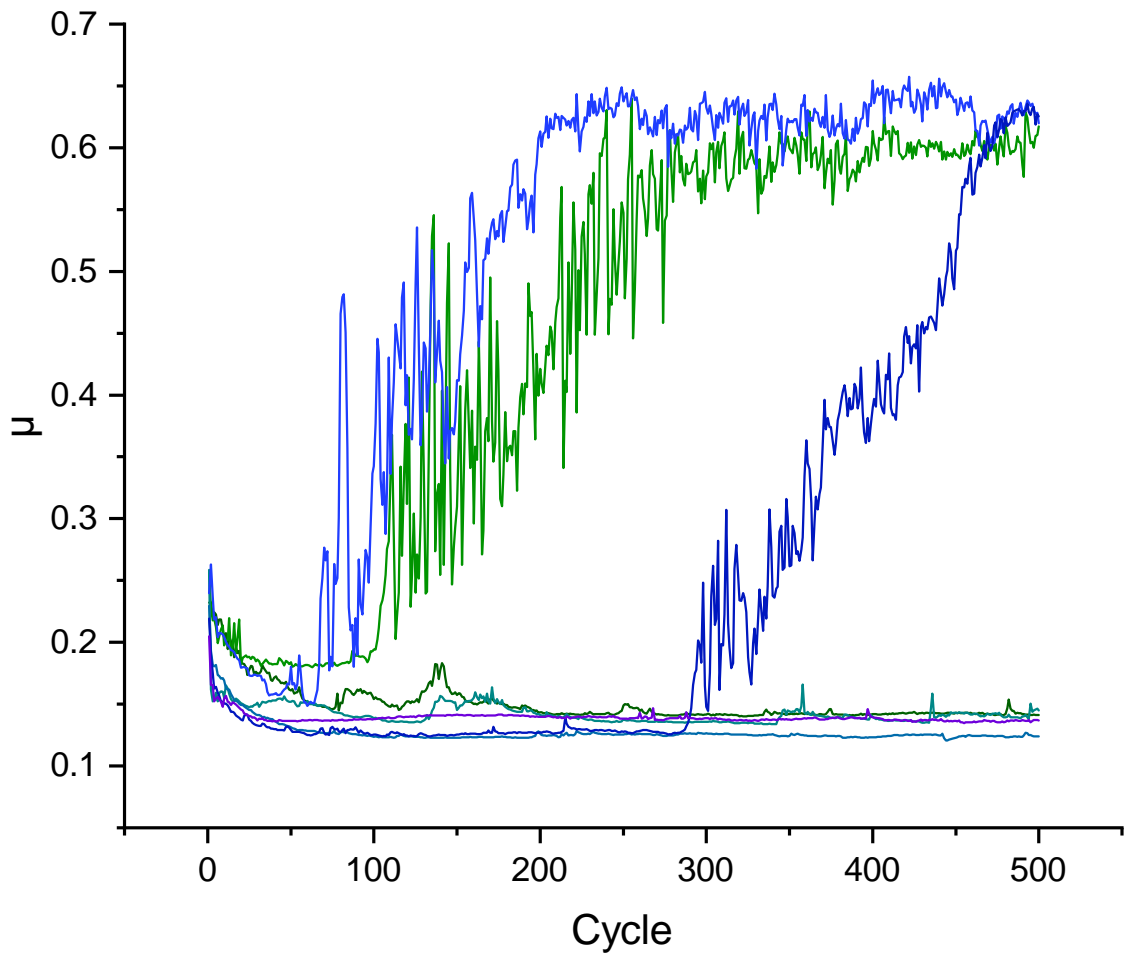
Figure A.5: CoF during the microtribometer experiments with a P2500 graphite-coated iron substrate at $1\,\mathrm{GPa}$ and $\leq 5\,\%\,\mathrm{RH}$, see Section 4.7.3.
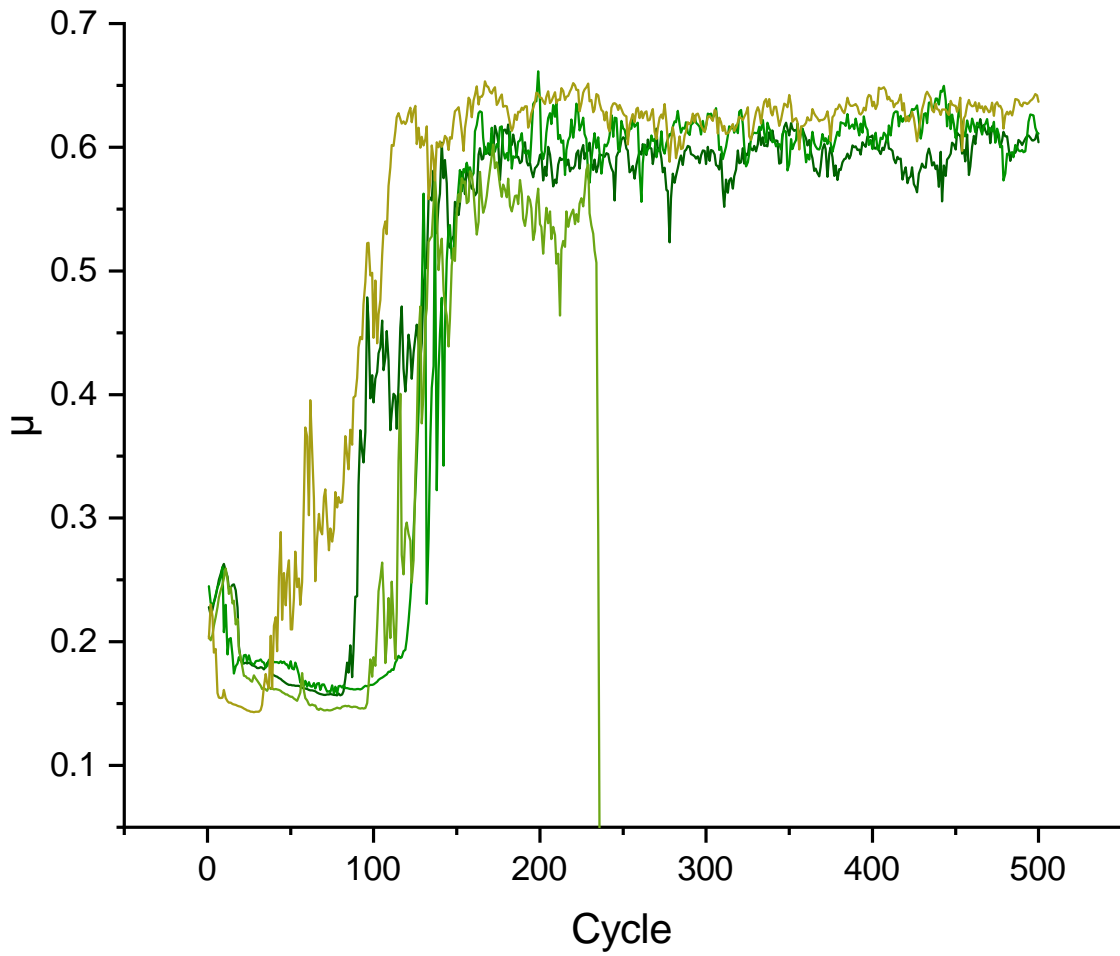
Figure A.6: CoF during the microtribometer experiments with a P4000 graphite-coated iron substrate at $1\,\mathrm{GPa}$ and $\leq 5\,\%\,\mathrm{RH}$, see Section 4.7.3.. The abrupt force decay of the light green experiment originates from a detaching of the steel sphere during the experiment.
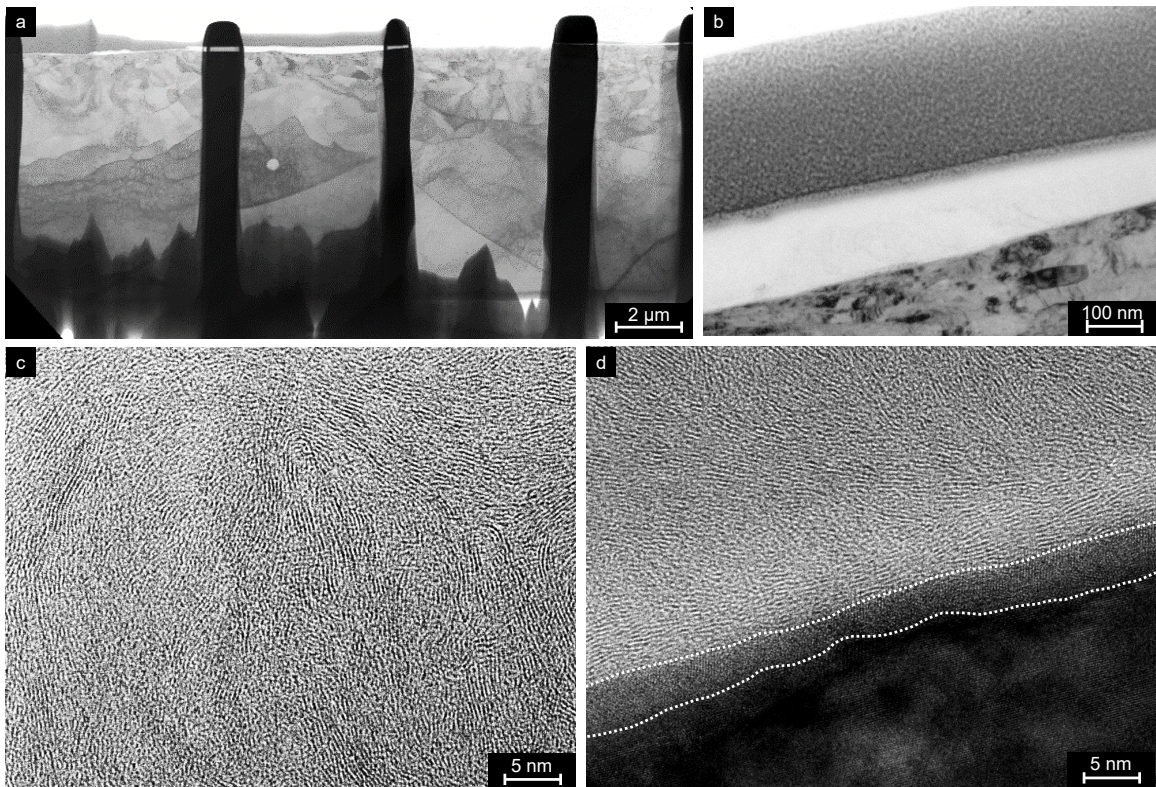
Figure A.7: Transmission Electron Microscopy images. Bright-Field (a,b) and High Resolution Transmission Electron Microscopy (c,d) images of the lamella prepared after microtribometer experiments at $1\,\mathrm{GPa}$ and $\leq 5\,\%\,\mathrm{RH}$. The focus lies on the thin carbon layer which is created in the middle of the wear track during sliding, see Section 4.8.2.
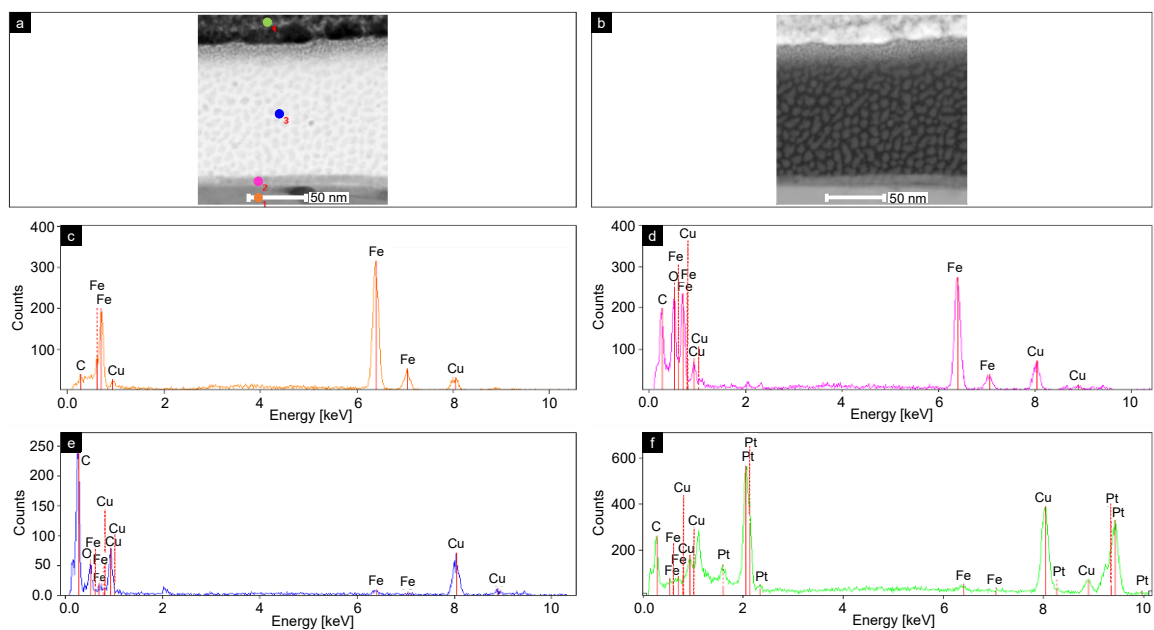
Figure A.8: Energy Dispersive X-Ray Spectroscopy of the thin carbon layer in the sliding contact. Measured after microtribometer experiments at $1\,\mathrm{GPa}$ and $\leq 5\,\%\,\mathrm{RH}$ at different regions. (a,b) TEM images recorded in bright field and dark field mode at the region of interest. (c) underlying iron substrate, (d) newly formed iron carbide layer, (e) newly formed carbon layer, and (f) protective Platinum layer, see also Section 4.8.2.
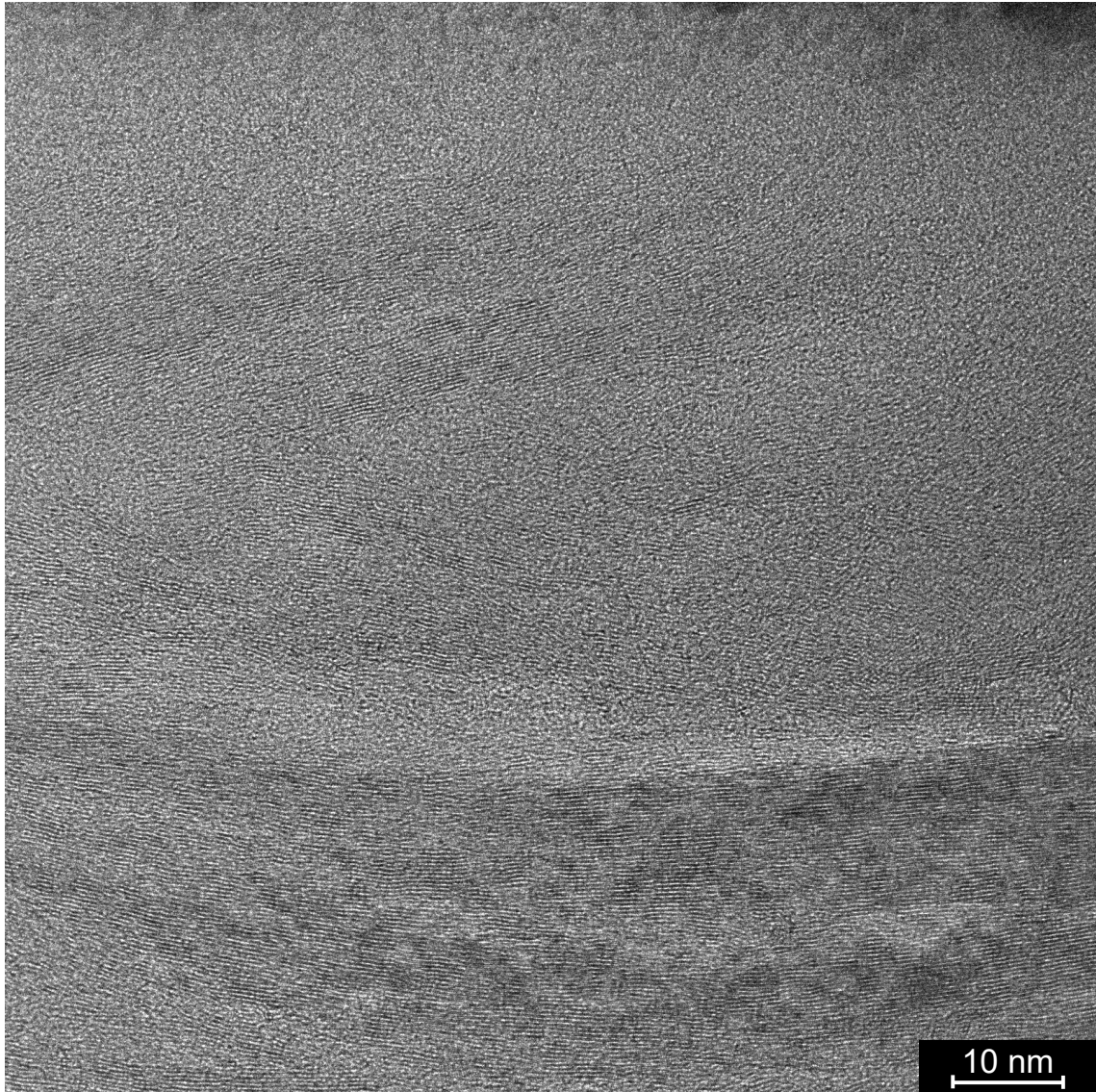
Figure A.9: High-resolution TEM image of the inset of Figure 4.26c. Visible is the surface of the thin carbon layer created during sliding in microtribometer experiments. On the bottom of the image highly ordered graphene bundles are observed, which are transitioned into turbostratic carbon (t-C) at the sliding interface seen at the upper region of the image, see also Section 4.8.2.
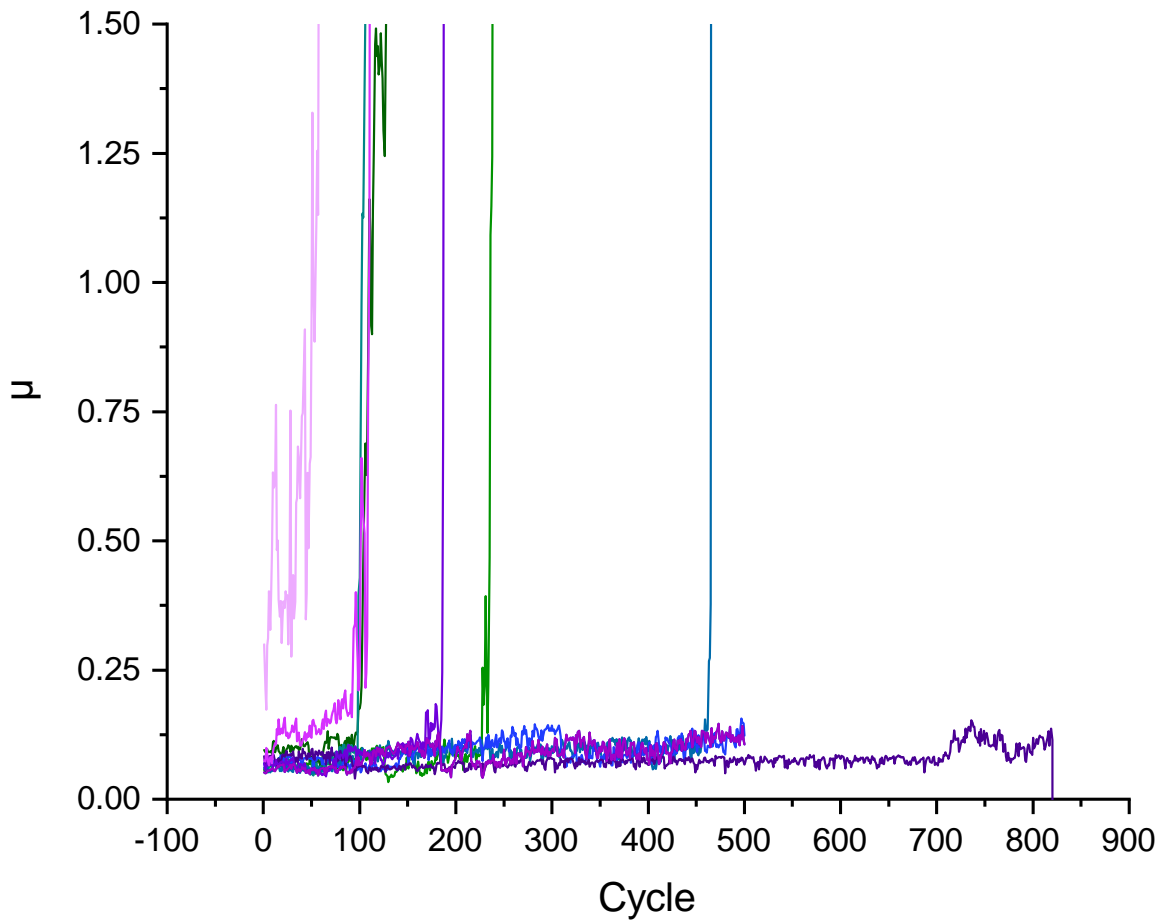
Figure A.10: CoF during sliding experiments under UHV at 1 GPa against a steel sphere, see Section 4.9.2.
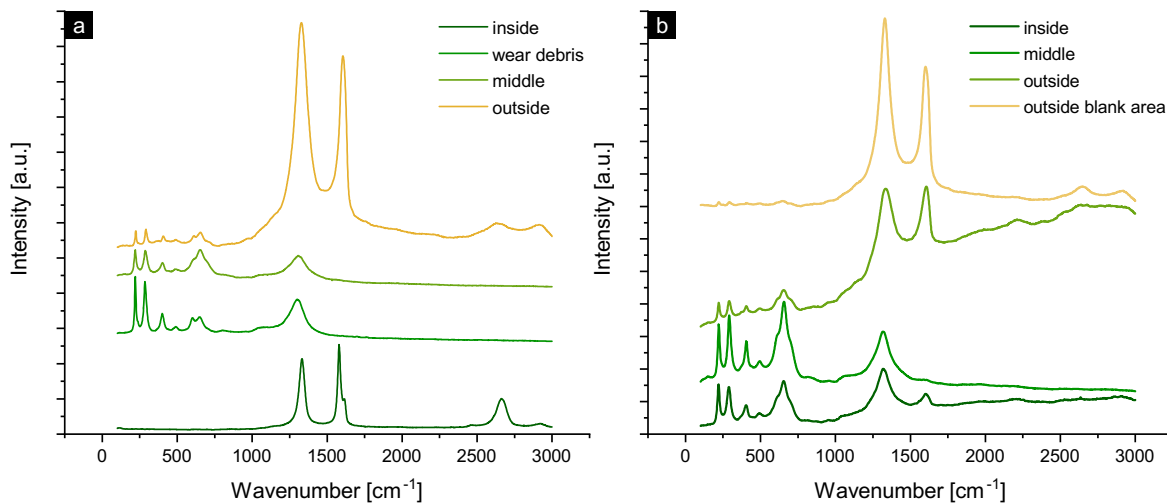
Figure A.11: Raman spectra taken after mini traction machine (MTM) rolling experiments at 0% SRR, 1 GPa, and $50\,\mathrm{mm\,s^{-1}}$ at different wear track positions on the ring (a) and the sphere (b), see Section 5.4.
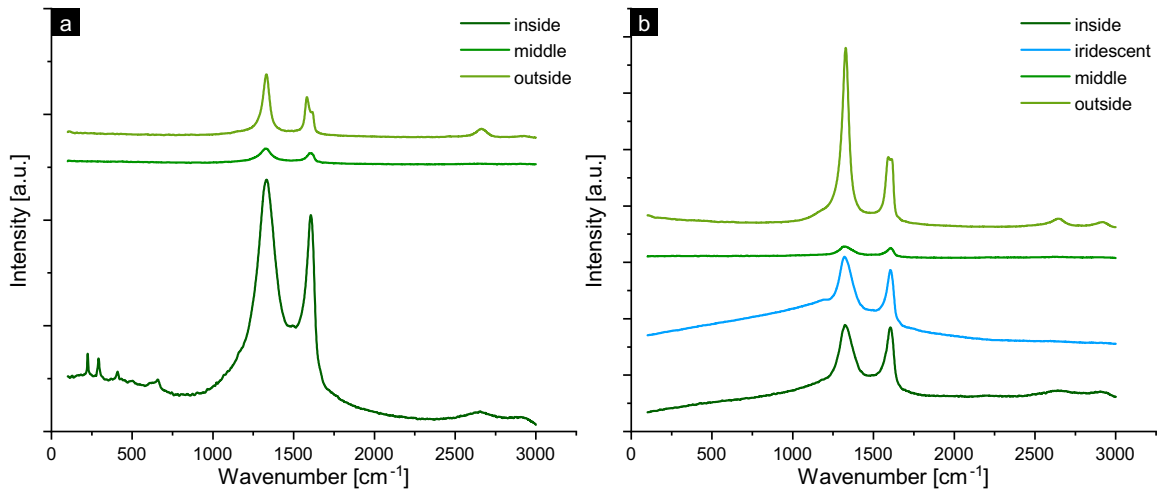
Figure A.12: Raman spectra taken after MTM rolling experiments at 5% SRR, 1 GPa, and $50\,\mathrm{mm\,s^{-1}}$ at different wear track positions on the ring (a) and the sphere (b), see Section 5.4.
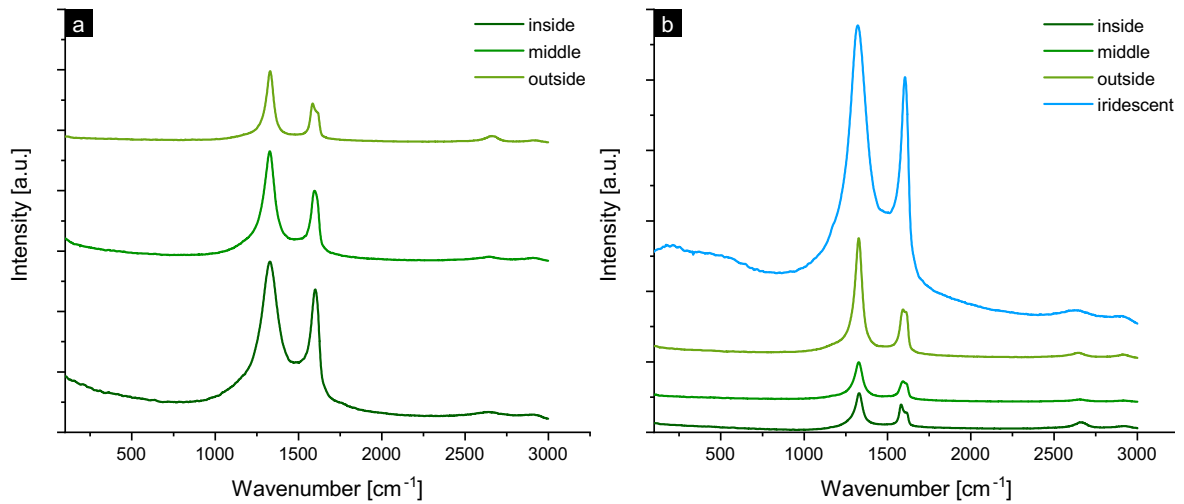
Figure A.13: Raman spectra taken after MTM rolling experiments at 10% SRR, 1 GPa, and $50\,\mathrm{mm\,s^{-1}}$ at different wear track positions on the ring (a) and the sphere (b), see Section 5.4.
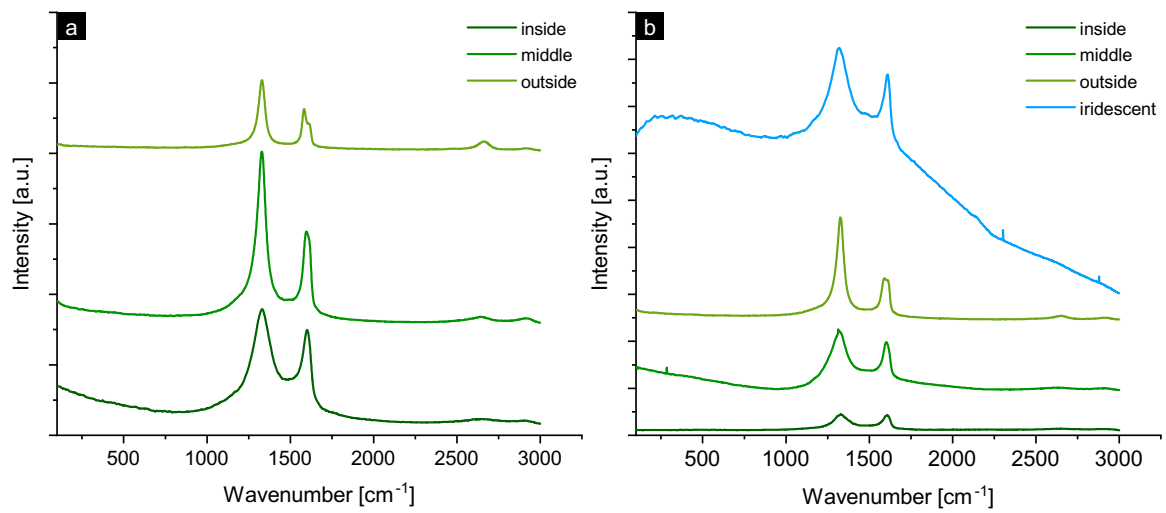
Figure A.14: Raman spectra taken after MTM rolling experiments at 15% SRR, 1 GPa, and $50\,\mathrm{mm\,s^{-1}}$ at different wear track positions on the ring (a) and the sphere (b), see Section 5.4.